The Auroral Large Imaging System
—Design, operation and scientific results

Abstract: The Auroral Large Imaging System (ALIS) was proposed in 1989 by Åke Steen as a joint Scandinavian ground-based network of automated auroral imaging stations. The primary scientific objective was in the field of auroral physics, but it was soon realised that ALIS could be used in other fields, for example studies of Polar Stratospheric Clouds (PSC), meteors and other atmospheric phenomena.

This report describes the design, operation and scientific results from a Swedish prototype of ALIS consisting of six unmanned remote-controlled stations located in a grid of about 50 km in northern Sweden. Each station is equipped with a sensitive high-resolution (1024×1024 pixels) unintensified monochromatic CCD-imager. A six-position filter-wheel for narrow-band interference filters facilitates absolute spectroscopic measurements of, for example, auroral and airglow emissions. Overlapping fields-of-view resulting from the station baseline of about 50 km combined with the station field-of-view of 50° to 60° enable triangulation as well as tomographic methods to be employed for obtaining altitude information of the observed phenomena.

ALIS was probably one of the first instruments to take advantage of unintensified (i.e. no image-intensifier) scientific-grade CCDs as detectors for spectroscopic imaging studies with multiple stations of faint phenomena such as aurora, airglow, etc. This makes absolute calibration a task that is as important as it is difficult.

Although ALIS was primarily designed for auroral studies, the majority of the scientific results so far have, quite unexpectedly, been obtained from observations of HF pump-enhanced airglow. ALIS made the first unambiguous observation of this phenomenon at high latitudes and the first tomography-like inversion of height profiles of the airglow regions. The scientific results so far include tomographic estimates of the auroral electron spectra, coordinated observations with satellite and radar, as well as studies of polar stratospheric clouds. An ALIS imager also participated in a joint project that produced the first ground-based daytime auroral images. Recently ALIS made spectroscopic observations of a Leonid meteor trail and preliminary analysis indicates the possible detection of water in the Leonid.

Keywords: Aurora, Artificial Airglow, HF pump-enhanced airglow, Multi-station measurements, Polar Stratospheric clouds, Radio-Induced optical emissions, Space physics, Spectroscopic imaging observations, Tomography.

IRF Scientific Report 279
Language: English
ISSN: 0284-1703
ISBN: 91-7305-405-4 pp. 184 pages

Kiruna, April 2003

Urban Brändström

Cover illustrations:

The large image is a portion of an all-sky colour image (see Section C.1) of an active auroral arc near zenith acquired on 12 December 2001 at 22:17:00 UTC with 4 s integration time. The five small pictures are all obtained with ALIS and show (from left to right):

1. White-light (i.e. no filter) image of a pulsating aurora from 11 April 1994 at 22:35:40 UTC obtained with 50 ms integration time by the ALIS station in Kiruna.
2. A polar stratospheric cloud (see also Figure 6.16 and Section 6.6.1) on 9 January 1997 at 14:19:30 UTC imaged in white-light and with 100 ms integration time by the ALIS station in Kiruna.
3. Top: The first unambiguous observations of HF pump-enhanced airglow that occurred on 16 February 1999 (see Section 6.4). The images are portions of ALIS images obtained at 17:32:25 UTC in the $O(^1D)$ 6300 Å emission-line with 5 s integration time at the ALIS station in Kiruna (left) and in Silkkimuotka (right). Bottom: A double-arc system imaged in the $O(^1S)$ 5577 Å emission-line on 25 March 1998 at 19:54:00 UTC by the ALIS imager in Silkkimuotka (integration time 100 ms). This image is part of a data-set used to estimate the auroral electron-spectra, see Section 6.5.1.
4. A Leonid meteor trail captured by the Kiruna ALIS station with a 4227 Å filter on 19 November 2002 at 03:48:00 UTC with 20 s integration time.
5. The same meteor trail, but imaged with an adjacent ALIS imager in Kiruna with a 5893 Å filter and 10 s integration time (refer to Section 6.6.2 for further information).

Doktorsavhandling vid Institutet för rymdfysik
Doctoral thesis at the Swedish Institute of Space Physics
The Auroral Large Imaging System —Design, operation and scientific results.
Online version and errata at: `http://www.irf.se/~urban/avh/`
Typeset by the author in LaTeX.
Kiruna, April 2003
Rev. 2

IRF Scientific Report 279
ISSN 0284-1703
ISBN 91-7305-405-4 pp. 184 pages
Printed at the Swedish Institute of Space Physics
Box 812
SE-981 28, Kiruna, Sweden
April 2003

Michail Pudovkin, David Rees, Mike Rietveld, Tima Sergienko, Mikko Syrjäsuo, Trond Trondsen, Bo Thidé, Assar Westman, Ian McWhirter and Ola Widell.

Thanks to Trevor Preston, Maureen Ffitch and colleagues at AstroCam Ltd for valuable discussions and help regarding the CCD camera and its software. A special acknowledgement goes to all the thousands of voluntary programmers making up the free and open software communities. ALIS was funded through FRN (Forskningsrådsnämnden), NFR (Naturvetenskapliga forskningsrådet), Swedish National Space board (Rymdstyrelsen, fjärranalyskommitén), IRF and Vetenskapsrådet. Without the financial support of the tax-payers of Sweden, Japan and other nations, as well as other funding sources, none of this research would have been possible.

I would have been completely unable to finish this work without the music of Johan Sebastian Bach, Ludwig van Beethoven, Franz Berwald and many others. Dag Hammarskjöld's book Vägmärken [Transl. as Markings; *Hammarskjöld*, 1963, 1964] provided guidance and inspiration to carry on.

Ett alldeles speciellt tack till min mamma, Astrid Brändström, som ställt upp för mig mer än någon son kan begära. En stor kram till min fästmö Anette Snällfot, som tålmodigt har stått ut med många olägenheter på grund av mina envisa försök att färdigställa detta arbete. Tillråga på allt drabbades hon av korrekturläsning och tryckeribestyr. Tack för allt stöd och all uppmuntran, jag hade inte klarat mig utan er! Sist ett postumt tack till alla de som på många sätt bidragit till detta arbete men som aldrig fick uppleva dess färdigställande.

Björkliden i april 2003

Urban Brändström

the newly established Royal Swedish Academy of Sciences, *Wilcke* [1778] summarises "the newest explanations of the northern lights". This speech includes a large set of early references.* *Wilcke* also remarks on the exceptional difficulties to make accurate recordings of auroral events. "The eye, the pen, and the brush of the fastest painter are too slow to record the changes"†. Yet, it would take more than one century until better tools became available. Meanwhile, artistic work, like drawings and paintings were the only available tools to record observations of northern lights [see references in *Eather*, 1980; *Pellinen and Kaila*, 1991]. Now, over 225 years later, and despite the giant leaps of technology, it is still a rather difficult task to make accurate auroral recordings.

1.1 Auroral imaging

Following the invention of photography the first successful picture of the aurora was taken by Brendel in 1892 [*Baschin*, 1900]. This paved the way for multi-station auroral imaging. One of the first large-scale auroral observation campaigns involving several stations was carried out by *Birkeland* [1908, 1913].

The most well-known imaging instrument is maybe the All-Sky Camera (ASC), which consists of a camera together with an optical arrangement of one or several mirrors providing near 180° field-of-view. This instrument exists in a variety of designs [for example *Stoffregen*, 1955, 1956; *Elvey and Stoffregen*, 1957; *Hyppönen et al.*, 1974, and others] and was pioneered by *Gartlein* [1947]. During the International Geophysical Year (IGY) of 1957–1958 a ground-based network of all-sky cameras was operating at 114 stations around the polar regions [*Stoffregen*, 1962]. Since then, improved versions of the all-sky camera have been the main observatory instruments for ground-based imaging of the aurora. Examples of present state-of-the-art digital all-sky cameras are the all-sky optical imager (ASI) in use at the Amudsen-Scott South Pole station [*Ejiri et al.*, 1998, 1999] as well as the cameras used in the Finnish MIRACLE network‡ [*Syrjäsuo*, 1996; *Syrjäsuo*, 1997; *Syrjäsuo*, 2001]. These all-sky cameras represent a considerable improvement over earlier instruments. Since a filter-wheel is present, spectroscopic measurements are possible. A somewhat different, and less advanced approach, is presented in Section C.1, where a commercial digital colour camera is used.

The intense development of television cameras starting in the late 1940's led to the emergence of better low-light imaging detectors based on television image-tubes, for example image orthicons and intensified vidicons. This enabled direct electronic recording of auroral image data. Absolute measurements with this class of detectors is very difficult, mainly due to calibration difficulties related to their non-linear response. Therefore these detectors have mainly been used for white-light imaging.

According to *Jones* [1974], the first use of image orthicon television camera systems for auroral observations were by *Davis and Hicks* [1964]. Image-intensified vidicon tubes were introduced by *Scourfield and Parsons* [1969]. Since

*See also [*Chamberlain*, 1995, Appendix VIII], regarding historical references.

†Free translation by the author, see the quote at the beginning of Chapter 3

‡`http://www.geo.fmi.fi/MIRACLE/`

important contributor to auroral spectroscopy was *Vegard* [1913]. Further information on auroral spectra, as well as more references are provided by *Jones* [1974] and *Chamberlain* [1995].

Sadly, spectrographs and spectrometers are rare instruments in present day auroral studies. As much more sensitive detectors exist today, a re-examination of the spectral features of the aurora might prove rewarding.

At the present time, the dominating instrument for spectroscopic studies of aurora is the interference filter photometer. This instrument is used either for fixed single-point measurements, or in a scanning or imaging configuration. Examples of contemporary instruments are found in *Kaila* [2003a].

1.2 Summary

This short introduction can in no way provide a complete overview of the field. Hopefully, it has at least provided a set of references for further studies and a rudimentary background to the desire to build ALIS as a multi-station imaging network capable of absolute spectroscopic measurements of column emission rates within the field-of-view of a traditional all-sky camera, as well as the capability to image a common volume, thus enabling triangulation and auroral tomography.

For further reading related to low-light optical instrumentation for auroral measurements see, for example, *Høymork* [2000], and references therein. *Galperin* [2001] presents an interesting discussion regarding the multiple scales of auroral phenomena. Such considerations are important for selecting a suitable baseline and field-of-view of a multi-station imaging system. An extensive review of instruments and networks for optical auroral studies was presented by *Pellinen and Kaila* [1991]. This was about the same time as work on ALIS commenced and therefore their work is recommended as an additional introduction, as well as an illustration of the power of coordinated studies with many instruments, regardless of whether they are ground-based or space-borne.

This work is organised in seven chapters and four appendices. A reader only interested in the scientific results from ALIS might wish to skip directly to Chapter 6, however, please consider quickly browsing through Chapters 2–4 for an introduction to the possibilities and limitations of the instrument. Technical details, related work and future plans are deferred to the appendices.

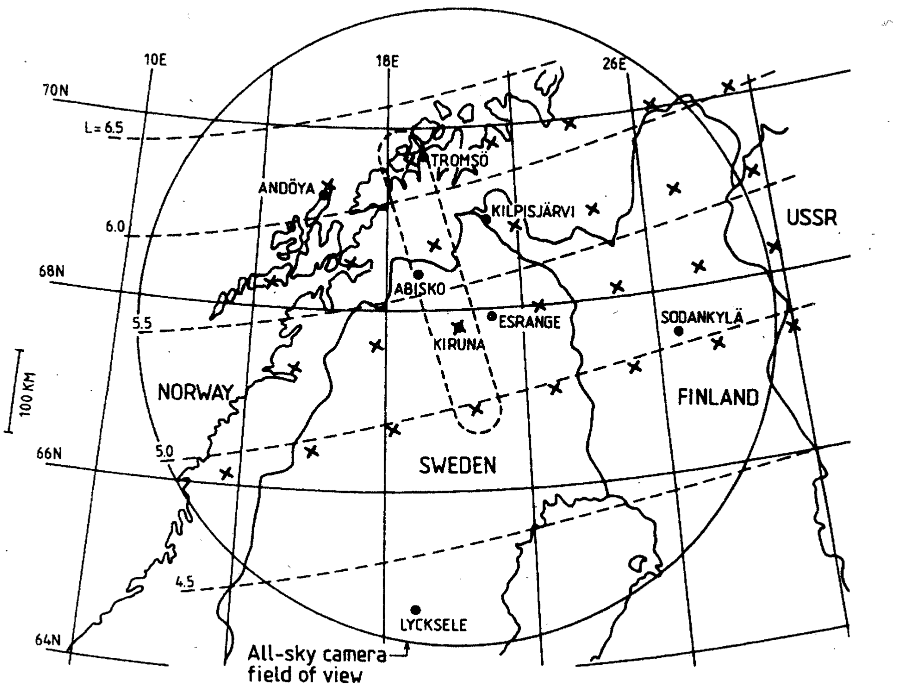

Figure 2.1: The first proposed layout of ALIS with 28 stations in northern Scandinavia separated by about 100 km, each with a field-of-view of about 90°. The suggested station sites are marked with crosses. The four stations enclosed in a dotted line represent a suggested mini version of ALIS. The large circle illustrates the field-of-view of an all-sky camera in Kiruna at ionospheric altitudes. [After *Steen*, 1989]

Year	1993	1994	1995	1996	1997	1998	1999	2000	2001
Stations	3	4	6	6	6	8	9	9	9
Cameras	1	1	4	5	5	6	6	6	6
Images	51	454	2374	3020	4034	15053	18905	19844	55878

Table 2.1: The ALIS time-line 1993–2001. ‘Stations’ represent the number of stations on site. ‘Cameras’ denotes the number of operational ALIS cameras, ‘Images’ lists the total number of images recorded each year.

2.1 The ALIS stations

The design and deployment of the ALIS stations involves a large number of considerations. Each station must be designed for unmanned remote-controlled operation during extended time-periods in low-population regions with a sub-arctic climate. The technical design of the ALIS-station, which constitutes a Ground-based Low-light Imaging Platform (GLIP), is considered in Appendix A.

The main scientific instrument at the ALIS-station is the ALIS-imager (covered in detail in Chapter 3). Although the stations are primarily designed for optical instrumentation, the design permits a variety of other instruments to share the common infrastructure. The general requirement on any additional scientific module is that it fits physically, does not interfere with existing equipment and is compatible with the resources available at the GLIP (for example power and communication). A number of scientific modules (for example auroral spectrometers, photometers, cloud cameras) were planned but are not yet realised. For a period, three stations, (1) Kiruna, (3) Silkkimuotka and (6) Nikkaluokta were equipped with pulsation magnetometers operated by the University of Newcastle, Australia. So far these have only used the mains power and not been remote-controlled. A radio-experiment involving a new type of antenna and a 3D-receiver is planned to be installed for testing at some of the ALIS stations [*Puccio*, 2002].

2.1.1 Scientific considerations

While large-scale auroral phenomena are most conveniently studied from space, medium to small-scale phenomena are usually studied using ground-based instruments. ALIS was designed to make absolute measurements of auroral phenomena within the field-of-view of a traditional all-sky camera (Figure 2.1).

In order to make accurate absolute measurements of auroral emissions, the optimal situation exists when the observation is carried out close to the magnetic zenith of the observation site. As the zenith angle increases, the need for photometric corrections due to spatial smearing as well as atmospheric effects also increases rapidly. On the other hand, if the field-of-view is too small, many more stations are required in order to obtain an acceptable spatial coverage and overlapping fields-of-view suitable for triangulation at auroral altitudes. Selecting a field-of-view in the range of 50° to 90° with a station baseline of 50–100 km appeared as a suitable compromise, and also economically feasible. Figure 2.3 illustrates the effects of station baselines and fields-of-view in these ranges. Note that the fields-of-view under consideration in this section are along the x/y directions on the CCD, *not* to be confused with the diagonal, or optical field-of-view, refer to Figure 4.1 and Table 4.6 for details. It is immediately seen that a 50° field-of-view combined with a 100 km baseline will not provide sufficient overlap for auroral triangulation and tomography (assuming the lower edge of the auroral curtain at about 105 km [*Størmer*, 1955]). Consequently, a baseline of about 50 km was selected together with a field-of-view of about 50° (see Table 4.6 for details). However, as four stations were put into operation, it was realised that increasing the field-of-view to about 60° would reduce the artifacts during auroral tomography (see references in Section 6.3), as well as providing better triangulation possibilities for studies of lower lying objects, for example polar-

			coverage in [km] at altitudes [km]:					
FoV	pixels	FoV_p	40	80	105	250	500	1000
50°			**37**	**75**	**98**	**233**	**466**	**933**
	64	0.78°	0.55	1.09	1.43	3.41	6.82	13.64
	128	0.39°	0.27	0.55	0.72	1.70	3.41	6.82
	256	0.20°	0.14	0.27	0.36	0.85	1.70	3.41
	512	0.10°	0.07	0.14	0.18	0.43	0.85	1.70
	1024	0.05°	0.03	0.07	0.09	0.21	0.43	0.85
60°			**46**	**92**	**121**	**289**	**577**	**1155**
	64	0.94°	0.65	1.31	1.72	4.09	8.18	16.36
	128	0.47°	0.33	0.65	0.86	2.05	4.09	8.18
	256	0.23°	0.16	0.33	0.43	1.02	2.05	4.09
	512	0.12°	0.08	0.16	0.21	0.51	1.02	2.05
	1024	0.06°	0.04	0.08	0.11	0.26	0.51	1.02

Table 2.2: Examples of approximative imager coverages in km (boldface), at some altitudes of interest given either a 50° or 60° imager field-of-view. For *each* field-of-view, the corresponding linear field-of-view per pixel (FoV_p) and pixel-coverage (in km) for a pixel looking in the zenith direction are given. (see also Section 4.3). The number of pixels also reflects some common binning factors in use with the present six ALIS imagers (see also Figure 3.4).

stratospheric clouds. Locating the two 60° imagers at appropriate stations thus provided a possibility for enhancing the results of tomography and triangulation.

The next parameter to consider is the spatial coverage and achievable field-of-view per pixel, FoV_p. Table 2.2 lists the linear coverage at some altitudes of interest for both the whole field-of-view, as well as for a pixel looking in the zenith direction. Note that these values are only to be interpreted as a first order approximation (see also Table 4.6 in Section 4.3). At 105 km altitude and 1024 pixels, the achievable pixel field-of-view is in the order of 100 m in zenith.

2.1.2 Selecting sites for the ALIS stations

Selecting the actual sites for the stations involved compromises. Although the first paper on ALIS [*Steen*, 1989] assumed that some stations would have to generate their own power and rely on microwave or satellite communications, budgetary considerations required the stations to be located in the vicinity of existing power and telecommunication lines. It was decided that the first station should be located close to the Swedish Institute of Space Physics (IRF) in Kiruna, in order to simplify development. The final decision on where to locate the remaining ALIS stations was based on a careful evaluation of a number of sites with regard to station separation (about 50 km) and geometry of ALIS with respect to tomographic as well as general auroral observation requirements, the proximity to commercial electrical power, telecommunication infrastructure and road access. Another important criteria was to find sites with low levels of man-made light pollution and a reasonably free horizon.

The highest priority was to populate the Tromsø–Kiruna meridian with sta-

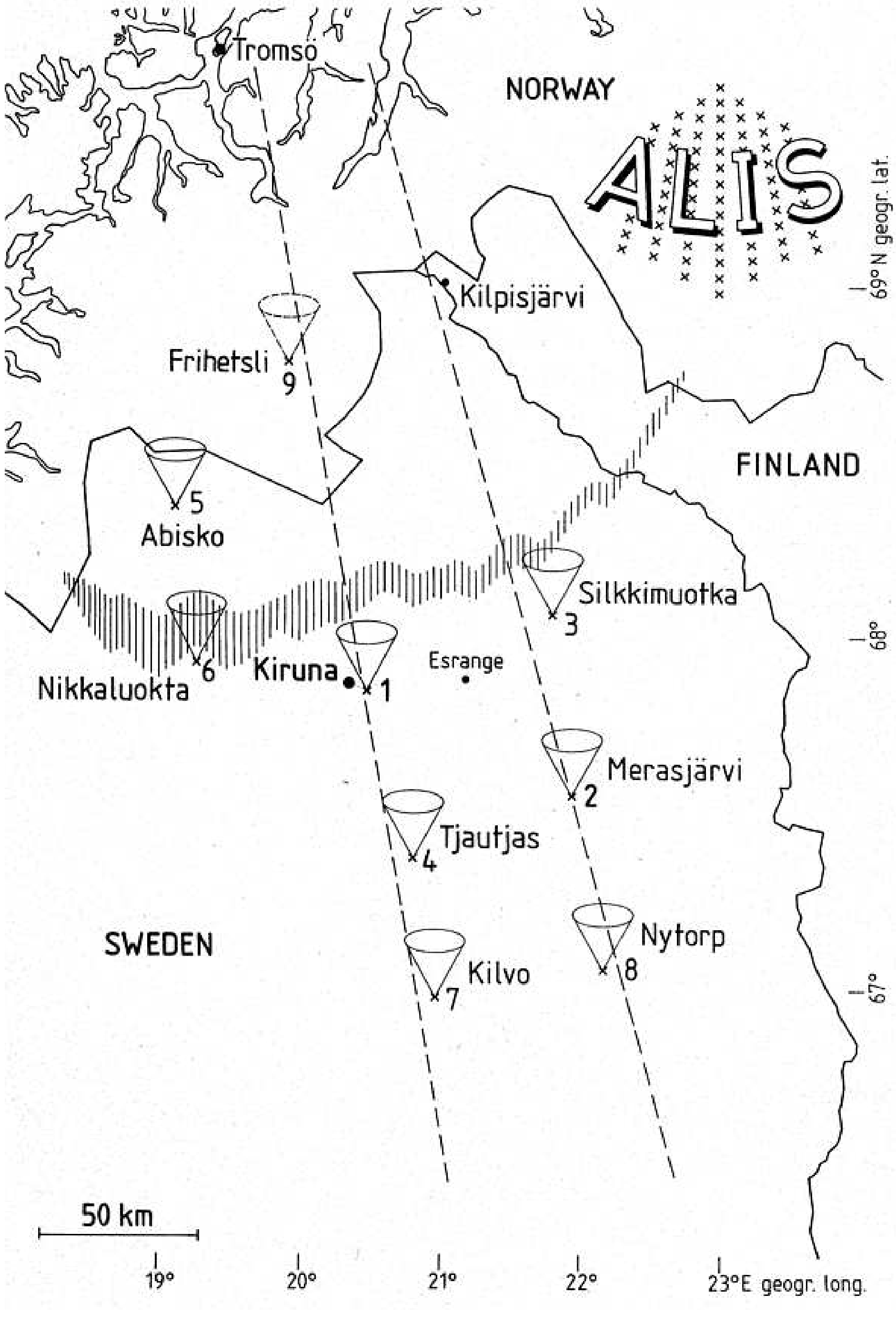

Figure 2.4: Map of northern Scandinavia displaying the final locations of the ALIS stations. See also table Table 2.3. The Control-Centre as well as a secondary Operations Centre is located in Kiruna.

Figure 2.5: The NIPU. The board contains four T222 modules, each controlling the α and β axes of the camera-positioning system as well as the filter-wheel and an additional Transputer intended (but never used) for GPS-timing. The large module is the T800-board with memory and parallel interface for image capture from the 16-bit parallel interface of the camera controller. Ample space is provided for future expansions with T9000 boards.

2.2.4 Station data storage

Various solutions for the local data storage at the stations have been considered over the years. Initially it was intended to store the image data onto Digital Data Storage (DDS) tapes which around 1992 had a storage capacity of up to 1 Gbyte. However, this solution proved slow and unreliable, mainly due to the hostile environment at the stations during tape-changes (moist, rapid temperature changes, etc.). Other solutions were also studied, but most of these were too complicated, too expensive or both. If faster communications would have been available, data could be stored on hard-disks, and downloaded to the control-centre in near real-time, or during non-measuring time. As the DDS drives tested at the first stations were not as reliable as expected, large (i.e. 2–9 Gbytes around 1992) external SCSI hard-disks were used instead. When a disk became full, it was exchanged manually, either by neighbours to the stations, or by staff from IRF. This solution proved simple and reliable. The only disadvantage was the usually rather long time (typically months) before raw-data from all stations became available for archiving and analysis.

2.2.5 Data archiving and availability

Reduced quick-look images (about 16 kBytes) are transmitted to the control centre and distributed to the operations centre (and web-site) in near real-time during measurement. However, these images are only intended for monitoring, and are of far too poor resolution for scientific analysis.

As the raw-data disks reach the control centre, recordable CDs (CD-R) of ALIS data are produced, and archived. All ALIS data produced so far are also made freely available on the world-wide web (see `http://www.alis.irf.se` for details) The main archive web-site is maintained by Peter Rydesäter who also provides a SQL database and search tools (see also Section 6.2).

The image data is stored in the Flexible Image Transfer System (FITS), [NASA, 1999]. This format is in wide use by the astronomical community, and found to be particularly suited to store scientific image data, as all supplementary information regarding an image (exposure time, filter, CCD temperatures, subsequent processing etc.) can be stored in the image header in a flexible way. FITS is recognised by many image processing packages, and free conversion programs to most other image formats exist on the Internet for most operating systems.

The size of the image-files is 16 bits/pixel (2 bytes) where the number of pixels is dependent on the configured spatial resolution (see Table 2.2 and Section 3.2). The total size of a set of images is also dependent on the number of stations involved and the temporal resolution selected.

2.2.6 Operating Systems

It was an early requirement to have a true multi-tasking operating system such as Unix for ALIS. HP-UX, which was delivered with the workstation selected for the control centre fulfilled this demand. The decision to use the IBM-PC architecture at the stations limited the choice of operating systems to SCO-Unix and MS-DOS. SCO-Unix was quite expensive compared to its reliability, so the

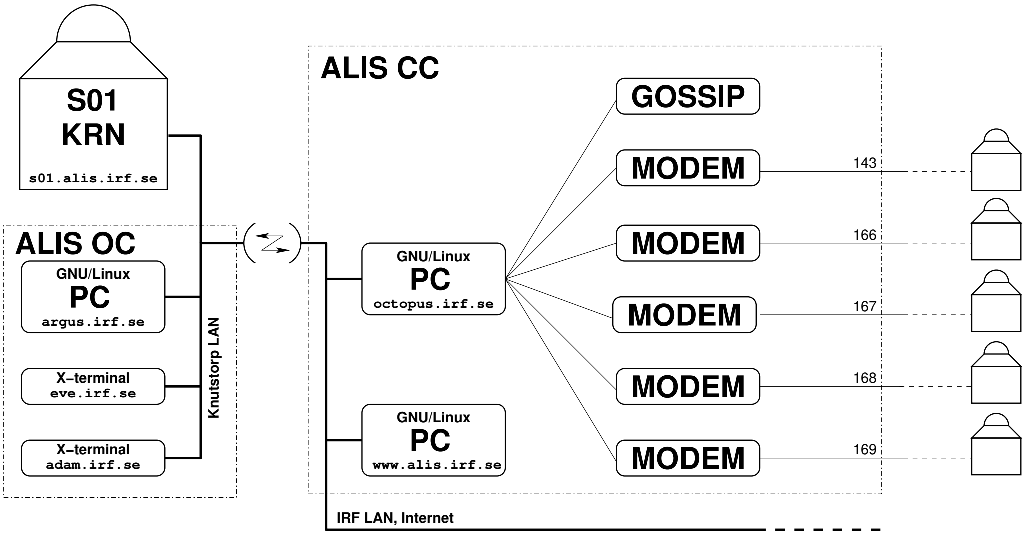

Figure 2.7: Block-diagram of the ALIS control centre (CC) at the optical laboratory, IRF Kiruna. The control centre consists of the gateway for dial-up access to the remote stations (`octopus.irf.se`) and its modem-pool. ALIS is controlled from the main computer (`www.alis.irf.se`) which also contains the web-server for ALIS. GOSSIP is a status display showing status and alarm information from the stations on a map [*Tornéus*, 1992]. The operations centre (OC) was initially located at the CC, but was later moved to Knutstorp (see text). It consists of a PC workstation and two X-terminals. Supporting optical instruments, for example low-light TV cameras, are also available at the OC. ALIS station 1 is located at the same site as the OC and they are both connected to the IRF LAN over a microwave link.

Φ, into a solid angle, Ω. The spectral radiant sterance in energy units, L_E, then becomes:

$$L_E(\lambda) = \frac{\partial^2 \Phi(\lambda)}{\partial A_s \partial \Omega} \quad \left[\frac{\mathrm{W}}{\mathrm{m}^2 \ \mathrm{sr}} \right] \tag{3.1}$$

where λ is the wavelength. Expressing the spectral radiant sterance in quantum units (L_γ) the following equation is obtained:

$$L_\gamma = \frac{L_E}{h\nu} = \frac{L_E \lambda}{hc} \quad \left[\frac{\mathrm{photons}}{\mathrm{s\ m^2\ sr}} \right] \tag{3.2}$$

Here ν is the frequency, h is Planck's constant and c is the speed of light. Please note spectral radiant sterance (radiance) is not to be confused with surface brightness which is a photometric unit involving the characteristics of the human eye [see *Holst*, 1998, pp. 20,26].

3.1.2 The Rayleigh

In terms of measurement techniques the aurora can be regarded as a five-dimensional signal with three spatial dimensions, one temporal and one spectral dimension. The desired physical quantity is usually the volume emission rate, $\epsilon(\mathbf{r}, t, \lambda)$, which cannot be found directly from measurements. However the rate of emission from a 1 m^2 column along the line of sight is normally just $4\pi L_\gamma$ for any isotropic source with no self-absorption [*Hunten et al.*, 1956].

Consider a cylindrical column of cross-sectional area 1 m^2 extending away from the detector into the source. The volume emission rate from a volume element of length dl at distance l is $\epsilon(l, t, \lambda)$ photons $\mathrm{m}^{-3}\,\mathrm{s}^{-1}$. The contribution to L_γ is given by:

$$dL_\gamma = \frac{\epsilon(l, t, \lambda)}{4\pi} \, dl \quad \left[\frac{\mathrm{photons}}{\mathrm{s\ m^2\ sr}} \right] \tag{3.3}$$

Integrating along the line of sight, l :

$$4\pi L_\gamma = \int_0^\infty \epsilon(l, t, \lambda) dl \tag{3.4}$$

This quantity is the column emission rate, which *Hunten et al.* [1956] proposed as a radiometric unit for the aurora and airglow. (See also *Chamberlain* [1995, App. II]) The unit is named after the fourth Lord Rayleigh, R. J. Strutt, 1875–1947, who made the first measurements of night airglow [*Rayleigh*, 1930]. (Not to be confused with his father, J. W. Strutt, 1842–1919 remembered for Rayleigh-scattering etc.) In SI-units the Rayleigh becomes [*Baker and Romick*, 1976]:

$$1\ [\mathrm{Rayleigh}] \equiv 1\ [\mathrm{R}] \triangleq 10^{10} \left[\frac{\mathrm{photons}}{\mathrm{s\ m^2\ column}} \right] \tag{3.5}$$

The word *column* denotes the concept of an emission-rate from a column of unspecified length, as discussed above. It should be noted that the Rayleigh is an apparent emission rate, not taking absorption or scattering into account. However, *Hunten et al.* [1956] emphasise that *"the Rayleigh can be used as defined without any commitment as to its physical interpretation, even though it has been*

Consider an extended source of area, A_s, of given column emission rate, I, imaged by an optical system, here represented by a single lens with given focal length, f, and f-number, $f_\#$. The relation between the aperture-stop, d_{app}, f and $f_\#$ is given by:

$$f_\# = \frac{f}{d_{app}} \tag{3.10}$$

Setting the source at distance r_s from the lens, which is at the distance r_i from the detector and letting Ω_{ds} be the solid angle of the lens aperture as seen from the source, (assuming small angles), the photon flux, $\Phi_{\gamma_{app}}$, at the lens aperture then becomes:

$$\Phi_{\gamma_{app}} = L_\gamma A_s T_a \Omega_{ds} = L_\gamma A_s T_a \frac{A_{app}}{r_s^2} \quad \left[\frac{\text{photons}}{\text{s}}\right] \tag{3.11}$$

The spectral radiant incidence at the aperture, $E_{\gamma_{app}}$, then becomes:

$$E_{\gamma_{app}} = \frac{\Phi_{\gamma_{app}}}{A_{app}} = \frac{L_\gamma A_s T_a}{r_s^2} \quad \left[\frac{\text{photons}}{\text{s } m^2}\right] \tag{3.12}$$

The spectral radiant incidence at the image plane, E_{γ_i}, is given by (by substituting Equation 3.10 and assuming a circular aperture):

$$E_{\gamma_i} = \frac{\Phi_{\gamma_{app}}}{A_i} = L_\gamma \frac{A_s}{A_i} T \frac{\pi d_{app}^2}{4 r_s^2} = L_\gamma \frac{A_s}{A_i} T \frac{\pi f^2}{4 r_s^2 f_\#^2} = L_\gamma \frac{A_s}{A_i} T \frac{\pi f^2}{4 r_s^2 f_\#^2} \quad \left[\frac{\text{photons}}{\text{s } m^2}\right] \tag{3.13}$$

Noting that, for thin lenses and small angles:

$$\frac{1}{r_s} + \frac{1}{r_i} = \frac{1}{f} \tag{3.14}$$

In this case:

$$r_s \gg r_i \Rightarrow r_i \approx f \tag{3.15}$$

The lens-magnification formula is:

$$M^2 = \left(\frac{h_i}{h_s}\right)^2 = \frac{A_i}{A_s} = \left(\frac{r_i}{r_s}\right)^2 \tag{3.16}$$

where h_i and h_s denote the height of the image and source respectively. Inserting Equations 3.6 and 3.14-3.16 into Equation 3.13, the following equation for E_{γ_i} is obtained:

$$E_{\gamma_i} = \frac{T\Phi_\gamma}{A_i} = T L_\gamma \frac{\pi}{4 f_\#^2} = T \frac{10^{10} I}{16 f_\#^2} \quad \left[\frac{\text{photons}}{\text{s m}^2}\right] \tag{3.17}$$

Note that this equation is only accurate for small angles, an off-axis image will have reduced incidence compared to an on-axis image. This is called the "natural vignetting", $\cos^4\theta$, and is usually inserted as a multiplication factor in Equation 3.17, as required.

However, the actual vignetting is highly dependent on the characteristics of the optical system. Therefore the vignetting as well as other aberrations, and the transmittance (T) must be experimentally determined. This will be considered further in Chapter 4 and references therein.

efficiency as 80–90% in the visible region as demonstrated in Figure 3.1. As

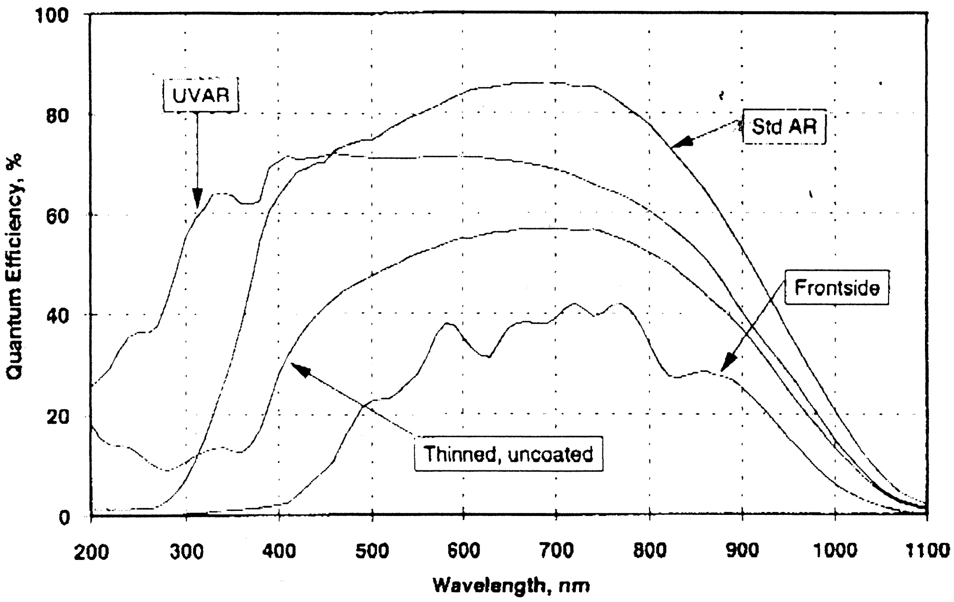

Figure 3.1: Quantum efficiency vs. wavelength for the SI-003AB CCD (ALIS `ccdcam5`) as published in the manufacturers data-sheet. Four curves are presented: with standard anti-reflection coating ("StdAR") UV anti-reflection coating ("UVAR"), uncoated, thinned, back-side illuminated ("Thinned uncoated") and front-side illuminated ("Frontside"). The ALIS imagers have a standard anti-reflection coating.

a comparison, Q_E for typical consumer CCDs lies in the range 30–70%. The average number of photoelectrons, $\overline{n}_{e^-_\gamma}$, obtained from $n_{\gamma_{pix}}$ (Equation 3.20) is:

$$\overline{n}_{e^-_\gamma} = Q_E n_{\gamma_{pix}} \left[e^-\right] \tag{3.22}$$

3.1.7 Noise

Aurora and airglow are so-called photon-limited signals, where the quantum nature of light limits the achievable signal-to-noise ratio. Photon arrival follows Poisson statistics, where the variance is equal to the mean. The sum of the standard deviation of the noise resulting from the photoelectrons, $\langle n_{e^-_\gamma} \rangle$, and dark-current noise, $\langle n_{e^-_d} \rangle$, is denoted shot noise, $\langle n_{e^-_s} \rangle$, and is obtained from the following equation:

$$\langle n_{e^-_s} \rangle = \sqrt{CTE^N \left(\langle n_{e^-_\gamma} \rangle^2 + \langle n_{e^-_d} \rangle^2 \right)} = \sqrt{CTE^N \left(\overline{n}_{e^-_\gamma} + \overline{n}_{e^-_d} \right)} \approx \sqrt{\overline{n}_{e^-_\gamma} + \overline{n}_{e^-_d}} \tag{3.23}$$

Here $\langle X \rangle^2$ stands for the variance of quantity X and $\langle X \rangle$ is the standard deviation. $\overline{X}$ denotes the mean value. CTE^N stands for the Charge Transfer Efficiency (CTE) where N is the number of transfers. Usually $CTE^N \approx 1$ for reasonably sized CCD devices. Note that $n_{e^-_\gamma}$ would be present even for an ideal detector.

Substituting Equation 3.26 the *SNR* can now be calculated with the help of Equations 3.20 and 3.22 and the total noise is given by Equation 3.26:

$$SNR_{CCD} \approx \frac{\overline{n}_{e^-_\gamma}}{\sqrt{\overline{n}_{e^-_\gamma} + \overline{n}_{e^-_d} + \langle n_{e^-_r} \rangle^2}} \tag{3.28}$$

For an ideal photon detector Equation 3.28 becomes:

$$SNR_{\gamma\text{ideal}} = \sqrt{\overline{n}_{e^-_\gamma}} \tag{3.29}$$

3.1.9 The signal-to-noise ratio of an ICCD

In the image-intensifier, for each primary photoelectron emitted by the photo-cathode (*pc*), the image-intensifier produces a burst of approximately 10^3 secondary CCD electrons, typically by the use of a micro-channel plate (MCP) between the photo-cathode and phosphor screen. The phosphor screen is then optically coupled to the CCD by the use of lenses or a fibre-optic taper†.

The number of photons reaching the image plane (n_{γ_i}) is given by Equation 3.18. The average number of signal electrons generated by the photo-cathode, $\overline{n}_{e^-_{\gamma,pc}}$, for a pixel area A_{pix} projected onto the photo-cathode, by the fibre-optic minification ratio, M_{FO} is given by [see *Holst*, 1998, p. 196]:

$$\overline{n}_{e^-_{\gamma,pc}} = Q_{E_{pc}} \overline{n}_{e^-_{\gamma i}} \frac{A_{pix}}{A_i} = Q_{E_{pc}} T t_{int} M^2_{FO} A_{pix} \frac{10^{10} I}{16 f^2_\#} \quad [\mathrm{e}^-_{\mathrm{RMS}}] \tag{3.30}$$

After the MCP the number of electrons are amplified with the average MCP gain, $\overline{g}$, i.e. average number of secondary photoelectrons, $\overline{n}_{e^-_{\gamma MCP}}$, produced per photo-cathode electron $\overline{n}_{e^-_{\gamma,pc}}$

$$\overline{n}_{e^-_{\gamma MCP}} = \overline{g}\, \overline{n}_{e^-_{\gamma,pc}} \quad [\mathrm{e}^-_{\mathrm{RMS}}] \tag{3.31}$$

The photoelectrons are then converted back to photons by the phosphor screen with a phosphor efficiency, η_P, and then re-imaged onto the CCD via a fibre optic taper. The transmittance losses here are denoted T_{FO}. Finally the photons hit the CCD and are converted to photoelectrons:

$$\overline{n}_{e^-_{\gamma CCD}} = \eta_P Q_{E_{CCD}} T_{FO}\, \overline{n}_{e^-_{\gamma MCP}} \quad [\mathrm{e}^-_{\mathrm{RMS}}] \tag{3.32}$$

By applying the following approximation:

$$Q_{E_{ICCD}} = Q_{E_{pc}} \eta_P Q_{E_{CCD}} T_{FO} \approx Q_{E_{pc}}$$

the following equation is obtained (using Equations 3.30-3.32):

$$\overline{n}_{e^-_{\gamma CCD}} = \overline{g}\, \overline{n}_{e^-_{\gamma,pc}} = \overline{g}\, Q_{E_{pc}} T t_{int} M^2_{FO} A_{pix} \frac{10^{10} I}{16 f^2_\#} \quad [\mathrm{e}^-_{\mathrm{RMS}}] \tag{3.33}$$

†In this text, the term “ICCD” is used for the combination of an image intensifier and a CCD, regardless of coupling type, or if they are manufactured as one unit or not.

3.1.11 Dynamic range

The Dynamic Range, DR, is defined as the peak signal divided by the RMS noise and the DC-bias-level, DN_{DC}, (if any). The minimum ADC output, DN_{min}, is subtracted in the case of a signed integer output. DR is usually expressed in decibels.

$$DR = 20\log_{10}\left(\frac{DN_{SEE} - DN_{min}}{DN_{DC} + DN_{NEE} - DN_{min}}\right)[dB] \tag{3.41}$$

An approximate theoretical value for DR is obtained by dividing the maximum signal (Equation 3.40) by the total noise, $\langle n_{e^-_{tot}} \rangle$, which is found in Equations 3.26 and 3.37 for the CCD and ICCD case respectively.)

$$DR \approx 20\log_{10}\frac{n_{e^-_{max}} - n_{e^-_{d}}}{\langle n_{e^-_{tot}} \rangle}\ [dB] \tag{3.42}$$

3.2 Selecting an imager for ALIS

The selection process for an ALIS imager includes many considerations of scientific, technical as well as of an economical nature. Naturally this leads to various compromises. A complete ALIS imager consists of optics, filters and a detector with its electronics and supporting systems. The choice of detector determines many parameters of the other imager subsystems, therefore this choice will be discussed first.

3.2.1 Comparison of an ICCD with a CCD imager

An ICCD imager was considered early on in the ALIS project [for example *Steen et al.*, 1990] and indeed many excellent CCD imagers for aurora and airglow, as, for example, the HAARP imager [*Lance and Eather*, 1993], the Portable Auroral Imager (PAI) [*Trondsen*, 1998] and the new Finnish all-sky camera [*Syrjäsuo*, 2001] as well as some of the imagers operated by *Kaila* [2003a] are based on an image-intensified CCD. Yet, it is important to realise that most CCDs have a higher Q_E than that of the photo-cathode in an image-intensifier. For example, the PAI, used for high spatial and temporal resolution auroral imaging, have a $Q_{E_{CCD}}$ of 67 %, while the quantum efficiency of the photo-cathode is only 28%, both at $\lambda = 5577$ Å [*Trondsen*, 1998, p. 51]. Scientific grade CCDs might have a $Q_{E_{CCD}}$ of up to about 90% as demonstrated in Figure 3.1. Despite this a CCD is not always preferable to an ICCD.

Figure 3.2 plots SNR as a function of column emission rate, with $f_{\#} = 3.9$ and a fixed integration time of 16.7 ms (NTSC video standard). The CCD data were taken from the technical specifications for the PAI (Table 3.1) as well as from the specifications for an ALIS imager (`ccdcam5`, Table 3.2). Ideal photon detectors with the same pixel area as of the ALIS Imager (a) and the PAI (c), have thresholds of detection at approximately 20 kR and 40 kR respectively. The ALIS Imager, curve (b), reaches $SNR = 2$ at about 100 kR which is also the case for the PAI ICCD (d). Curve (e) for the unintensified CCD of the PAI (without image intensifier) does not reach $SNR = 2$ until at approximately 2 MR. Clearly,

Parameter	Symbol	ccdcam5	Unit	Notes
Read noise	$\langle n_{e_r^-} \rangle$	8.3	e^-_{RMS}	a) b)7.5@10.5μs/pixel
Dark current	$\overline{n}_{e_d^-}$	12.4	$e^-_{RMS}\ s^{-1}$	at $-15°C$.
Full well	$n_{e^-_{max}}$	316	ke^-	c)
Quantum efficiency	Q_E	89.8	%	4000 Å
Quantum efficiency	Q_E	98.9	%	5500 Å, at $-15°C$, d).
Quantum efficiency	Q_E	99.4	%	7000 Å, d).
Quantum efficiency	Q_E	55.3	%	9000 Å

Table 3.2: Some parameters for the CCD in ALIS-imager ccdcam5 (SI-003AB serial No. 6144GBR10-B2) as measured by the CCD-manufacturer. All values measured at $-45°C$ unless otherwise noted. Notes: a) quadrant with highest value. b) same parameter, as measured by camera manufacturer. c) quadrant A 3% linearity. d) questionable assuming a lower value of about 85% (Figure 3.1) [author's note]. (See also Tables B.1–B.6 in Appendix B)

this CCD is not suitable for low-light observations, without image intensifier. These results are in agreement with *Trondsen* [1998, Chapter 4].

At low column emission rates, the ALIS Imager and the PAI ICCD appear comparable in *SNR*. However, note that this is a misleading result, as the PAI ICCD, with its frame-transfer CCD, provides data at NTSC video rates (30 frames/s), while the read-out of the ALIS quad read-out full-frame CCD is limited to about 2.8 s at the stated read noise, resulting in a maximum frame rate of about 0.3 frames/s (see Table 3.3 in Section 3.2.2). Therefore, as already noted by *Trondsen* [1998] it might be concluded that the ICCD is the better choice for temporal resolutions $\leq 1s$ needed by the high temporal resolution requirements on the PAI.

While the CCD is a linear device, the image-intensifier is an electron-tube exhibiting non-linearities and aging effects making the already non-trivial task of absolute calibration even more complicated. Also image-tubes might bloom, causing the entire image to saturate, if part of the scene within the field-of-view saturates. Exposure to too bright point sources might lead to permanent image retention or intensifier damage [See for example *Holst*, 1998, and references therein]. For these reasons it was decided to further investigate the feasibility of using an unintensified CCD for the ALIS imagers. However, for such a system to be useful for studies of aurora and airglow, the unintensified CCD must provide acceptable *SNR* for column emission rates down to a couple of hundred Rayleigh, for integration times of about 1 s. Figure 3.3 displays the *SNR* plotted versus integration time for column emissions ranging from 100 R–1 MR. As seen IBC-I–IV have acceptable *SNR* for 1 s integration time. Examining Equation 3.28, it is seen that the *SNR* can be increased by increasing the number of photoelectrons, i.e. by increasing the pixel area, improving the transmittance, increasing the integration time, or by improving the quantum efficiency (see Equations 3.20 and 3.22). One possibility is to utilise on-chip binning factors ("super-pixels") to increase the pixel area as demonstrated in Figure 3.4. As seen, the threshold of detection improves by the product of the binning factor (i.e. the increase of pixel area). On the other hand, the spatial resolution is decreased by the same factor.

This also implies that the frame-rate increases, as there are less pixels to read-out. Thus, for any given measurement situation, application of on-chip binning factors provides a way to optimise a compromise between sensitivity, spatial and temporal resolution.

For high column emission rates the CCDs saturate after reaching their charge well-capacity. It should be noted that pattern noise is not taken into account in the plots. This noise would have decreased the *SNR* somewhat at high-signal levels, but is of little interest for photon-limited imaging situations.

3.2.2 Frame rate

The ALIS CCD is a full frame CCD. The read-noise (which increases as the square-root of the pixel-rate, mainly due to the 1/f-noise, see Section 3.1.7) in Table 3.2 was measured at a pixel read-out rate of $10.5\mu s$/pixel. At this rate it would take 11 s to read 1024^2 pixels. One way of getting around this problem is to divide the CCD into sub-arrays. The ALIS CCD is divided into four sub-arrays with identical read-out channels working in parallel (Figure 3.5). Table 3.3

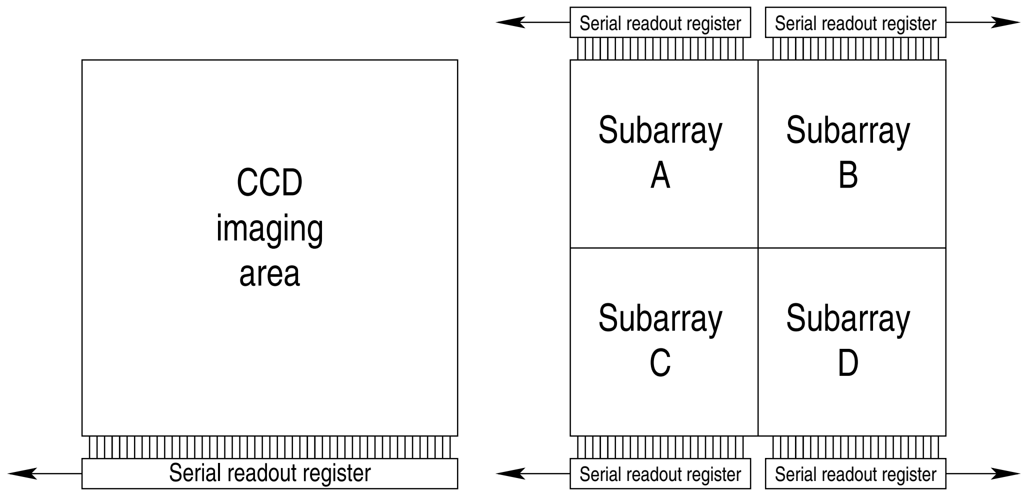

Figure 3.5: At a given pixel rate, a full frame CCD (left) takes four times as long to read-out as compared to an array divided into four sub-arrays (right), each with its own serial read-out register, sense node, amplifiers, S/H circuits and ADC:s.

illustrates the maximum achievable read-out rates for the ALIS CCDs.

The frame rate, FR, as a function of on-chip integration ("exposure") time, t_{int}, read-out time, t_{read}, and misc. time before the next image can be read, t_{misc}, (for example caused by the electronics, or the need to flush the CCD etc.) is given by:

$$FR = \frac{1}{t_{int} + t_{read} + t_{misc}} \tag{3.43}$$

sealed compartment. Note that the CCD itself has no optical window exposing the chip and bonding threads to the environment of the compartment. Therefore, the sealed compartment may not be opened, unless in a clean room environment with adequate electrostatic discharge (ESD) protection measures as CCDs are extremely sensitive to ESD discharges. Also, proper equipment for venting and re-sealing the compartment needs to be present.

A vendor-provided CCD test report accompanied each CCD-chip, and excerpts from these reports, as well as some measurements provided by the camera manufacturer, are provided in Appendix B as Tables B.1–B.6 as well as in Table 3.2 above.

The camera head also contains a circuit board with low-noise preamplifiers and buffers for the four analogue read-out channels, etc. A heat-sink and a cooling fan on the back of the camera head cools the hot side of the Peltier cooler. Three temperature sensors measure CCD, ambient and heat-sink temperatures. Two round 2 m 37-way screened twisted flat-cables with "DSUB" connectors in each end connect the camera head to the camera control unit[§]. These cables are individually matched to each imager system and may not be interchanged. A third cable is powering the Peltier cooler.

3.3.2 The camera control unit

The camera head is powered and controlled by a Camera Control Unit (CCU). This unit includes analogue and digital signal processing chains for the four identical signal processing channels, as well as other control electronics and power supplies (Figure 3.6).

The CCU is controlled by a T222 Transputer, which communicates with its host systems over a Transputer-link (a kind of serial interface). CCD clocking and pixel read-out is controlled by an Erasable, Programmable Logic Device (EPLD) that is capable to read-out up to 4×4096 pixels without pausing. The analogue pixel values are digitised using four fast 16-bits Analogue to Digital Converters (ADCs). The data is then stored in four 4 kByte FIFO memories for subsequent transfer to the host computer, either on the Transputer link, or by way of a 16-bit parallel port. The maximum possible theoretical pixel rate is $1.5\mu s$/pixel. If desired, any CCD quadrant, or region of interest can be read-out separately.

3.3.3 Configuring the imager

All configuration settings of the CCD imager are under software control. A configuration file (`4400.cf`, see `http://alis.irf.se/alis/alis/ccdcam`) stored on the controlling computer is uploaded to the CCU during its boot procedure. This file contains configuration settings for CCD-size, clock timing, voltage and gain settings, etc. The configuration file is unique to each CCD and imager. By changing appropriate configuration settings, it is possible to reconfigure the imager for various situations. As each of the four signal processing channels have software selectable gain settings as well as DCS (Section 3.1.7) time constant and slope settings, this allows for a wide range of speed, gain and noise settings. Table 3.3 gives a brief overview of some of the possible trade-offs between noise performance and

[§]Note the cables are only about 1 m and flat on the prototype unit (`ccdcam1`) read-out speed. For a more detailed understanding of these configuration possibilities, please refer to the imager documentation and configuration files. See also Table 3.2, Equations 4.7 and 4.8 in Section 4.2.1.

3.3.4 The user port

"Okay, Houston, we've had a problem here." *John Leonard Swigert, Jr.*

As the T222 Transputer links are capable of no more than 20 Mbits/s, image-data transfer at maximum pixel-clocking would be too slow. To remedy this the camera controllers are equipped with a 16-bit parallel interface. Originally it was intended that data from this interface would be read directly by the NIPU, however, due to the fast technical development, an extra computer responsible for receiving and storing the image data took over the role of the NIPU (see also Section 2.2.2). A prototype fast read-out interface card for a PC computer was built and tested. During these tests it was found that the user port omitted the 50 last pixels of each line on each of the four read-out channels (corresponding to a total of 102400 pixels in the centre 100 columns of the image) thus rendering the image data useless. Contacts were taken with the camera manufacturer to remedy this. This resulted in a new version of the camera controller software, fixing some of these problems, but now severe intermittent problems arose. Great effort was made to find the cause of these data-losses but without success. A solution to these problems still remains to be found, and meanwhile, the fast read-out mode had to be abandoned.

3.3.5 Operational remarks

At the time of writing, the ALIS imagers have been in operation for up to ten years. During this time they have produced a large number of images resulting in scientific findings as reported in Chapter 6, and references therein. The main technical obstacle has been poor frame-rate as discussed above.

The oldest, prototype imager, (`ccdcam1`) still works well, as does the newest imager (`ccdcam6`). The second camera (`ccdcam2`) developed a problem with ice on the CCD in 1999, probably due to a breach in the hermetic compartment. This problem should be fairly easy to resolve. The remaining cameras have had intermittent reliability problems related to the electronics. The occurrence of these problems has increased during the last couple of years. Another issue is that much of the camera electronics is becoming obsolete, severely affecting spare-parts availability. On a short time-scale (3–5 years), a limited maintenance operation will most likely bring 4–6 imagers back into operation. However, in a longer perspective, the now rather old imager electronics need to be completely replaced. During such a renovation it must be investigated if the most expensive part of the system (i.e. CCDs), and even the camera heads can be reused. All six CCD detectors are in good condition, and still among the best imaging detectors available for the scientific objectives of ALIS.

about 50°. Experiences gained from tomographic reconstruction using images from these four systems resulted in a decision to slightly widen the field-of-view for the next two imagers. Consequently these were equipped with a 35 mm front-objective, giving a diagonal field-of-view of about 90°.

According to vendor specifications [*Keo Consultants*, 1994, 1997], the f-number setting on the front lens, $f_{\#fl}$, will determine image brightness on the CCD, as well as the maximum ray-angle through the filter, θ_{max}, given by the following approximate formula:

$$\theta_{max} = \arctan\left(\frac{1}{2f_{\#fl}}\right) \tag{3.44}$$

A photograph of the six ALIS imagers appears in Figure 3.6.

3.5 Interference filters

To make spectroscopic imaging, narrow-band interference filters are required. These filters are sometimes referred to as Fabry-Perot filters, as they are multiple cavity solid Fabry-Perot etalons [See for example *Macleod*, 1986; *Hernandez*, 1986, and references therein]. Rays passing through an interference filter must be nearly normal to the filter system. This dictates the use of a telecentric lens-system as discussed in Section 3.4.

The passband of an interference filter with effective index of refraction, N_e, ($N_e \approx 2$ for most interference filters) and filter centre wavelength at normal incidence, λ_{cw}, shifts to λ_θ at angle of incidence θ according to the following equation¶:

$$\lambda_\theta = \lambda_{cw}\sqrt{1 - \frac{sin^2\,\theta}{N_e^2}} \tag{3.45}$$

As seen, the passband shifts to shorter wavelengths at increasing angle of incidence. This fact is often utilised to fine-tune filters, or to measure background intensity by tilting the filter out of the passband for the emission line under study. In the case of the ALIS optics, let θ define a cone between normal incidence and θ_{max} given by Equation 3.44. Optimum filters for this situation should be designed as insensitive to angle as possible, and the bandwidth should be wide enough to pass the wavelength(s) of interest at all angles within the cone. Thus θ_{max} also defines the minimum possible bandwidth of the filter. Given a wavelength region of interest, specification of the optical system, filter centre wavelength (λ_{cw}) and desired filter-bandwidth, $\Delta\lambda$, an optimal filter is manufactured. As almost every batch of filters are tailored for a particular application, high-quality interference filters for imaging applications are rather expensive devices. Data on the filters used for ALIS appear in Tables 3.4-3.5. A discussion of the selected emission lines is found in the work by *Gustavsson* [2000, Chapter 2] and references therein.

¶from the filter manufacturer (`http://www.barrassociates.com/terms.php?type=angle`), see also [*Jones*, 1974]

	Emission		Filter		
Pos.		λ [Å]	λ_{cw} [Å]	$\Delta\lambda$ [Å]	Notes
0	$O(^1S)$	5577	5590	40	
1	$O(^1D)$	6300	6310	40	
2					See Table 3.5
3					empty
4					See Table 3.5
5	N_2^+ 1Neg.	4278	4285	50	

Table 3.4: Filter placement standard for ALIS. The empty position is for white-light imaging (without filter). Two optional positions are available, see Table 3.5

	Filter CW			Positions at `ccdcam`					
λ [Å]	λ_{cw} [Å]	$\Delta\lambda$ [Å]	usage	1	2	3	4	5	6
4227	4225	280	meteor studies						2
	6230	40	background filter.	2	2	2	2	2	
	5324	50	Lidar filter			4			
	5100	40	background filter.						2
5893	5898	200	meteor studies (Na)	2					
8446	8455	40	$O(3p^3P)$	4			4	4	4

Table 3.5: Optional filters and their usage. The last six columns display the filter position assignments for the six imagers. See Section 6.6.2 regarding the filters for meteor studies.

3.6 The camera positioning system

As the imagers are using moderate fields-of-view (Figure 2.3), a Camera Positioning System (CPS) is required in order to be able to configure ALIS for various imaging situations. For example, when running in a tomographic mode, observation of a common volume centred on an auroral arc is desired, while maximum sky coverage, or tracking of the foot-point of a spacecraft might be the objective of other observational modes. When observing for example HF-pump enhanced airglow (Section 6.4), the cameras need to point towards the anticipated region of enhanced airglow above the EISCAT-Heating facility in Tromsø

Initially a traditional azimuth/elevation drive with rotation in azimuth and elevation was considered, but it was found that such a drive would be difficult and expensive to build given the size and weight of the imager and the available space at the station. There is also a cable wrap problem associated with the azimuth drive, where the drive would have to rotate back 360° in certain imaging situations. Because of this, a solution consisting of three frames mounted inside one another was selected.

The two innermost frames are mounted on perpendicular axes. The ALIS imager is attached to the innermost frame (Figure 3.10). Stepping motors are connected to one end of each axis via a worm-gear assembly, and an angular encoder is attached to the other end. The worm-gear assembly gives an automatic brake when the stepping motors are disengaged, but also introduces a small lag. The innermost axis is denoted α and the outer axis β. In this way it is possible to reach any region on the sky, keeping the image rotations small and without wrapping the cables. Also the cable lengths can be kept short (about 0.5 m) and the imager is accessible for maintenance and fairly easy to remove. A worst-case repositioning typically takes less than 10 s, and the accuracy is 0.01° as long as the stepping motors are engaged.

The CPS Control unit (CPC) is a similar electronics unit to the FWC (Figure 3.9) and contains the power supply and electronics for the CPS. Both the FWC and the CPC are in turn controlled by the NIPU (Section 2.2.2). Conversion of set azimuth, a_ϕ, and zenith-angle, z_θ, of the optical axis, into α and β values is automatically done by the NIPU software according to these equations:

$$\alpha = \arctan(\sin a_\phi \ \tan z_\theta) \tag{3.46}$$

$$\beta = -\arcsin(\cos a_\phi \ \sin z_\theta) \tag{3.47}$$

Azimuth is defined as zero towards North and 90° towards east. Zenith angle is zero in zenith and increases towards the horizon, (i.e. $z_\theta = 90° - h_\theta$, where h_θ is the elevation). It is worth remembering that the azimuth value is undefined for small zenith angles. The maximum zenith angle is typically about 54°.

To simplify the use of ALIS, a set of standard pre-programmed positions for various typical observing requirements are available (Table 3.6 and Figure 3.11).

The present CPS has been in use since 1993. Since being put into operation the CPS appears to be reliable and it has worked for years without any major problems. Worm-gear adjustment due to mechanical wear, as well as some angular encoder failures, probably due to an aging laser-diode in the angular encoder,

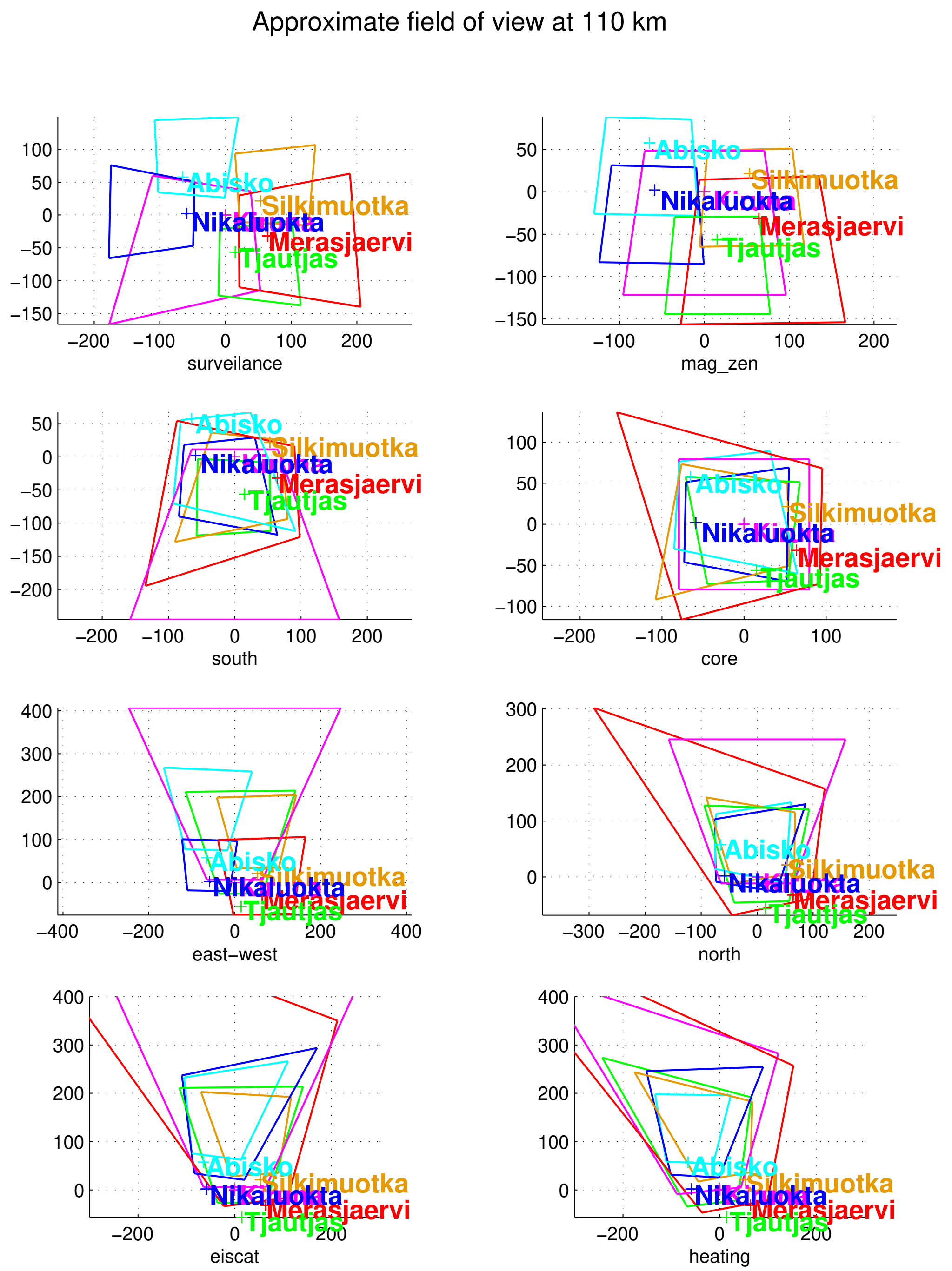

Figure 3.11: Projections to 110 km for the preset camera positions of Table 3.6. The axes are in km west-east (X) and north-south (Y) relative to Kiruna.

CPS Control Unit (CCU) : containing power-supply and electronics for the CPS (Figure 3.9).

Camera stand : consisting of four iron rods, directly attached to the corners of the iron frame supporting the house, thus the imager is not affected by vibrations in the house caused by for example strong winds (Section A.1).

A block diagram displaying the interrelationships of the various imager subsystems appears in Figure 3.12.

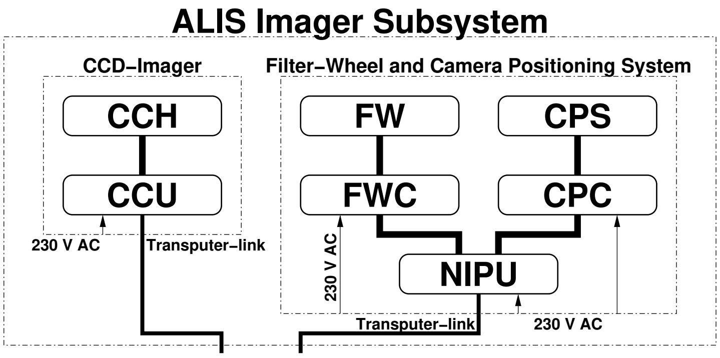

Figure 3.12: Block diagram of ALIS imager subsystems. Regarding the NIPU, see Section 2.2.2

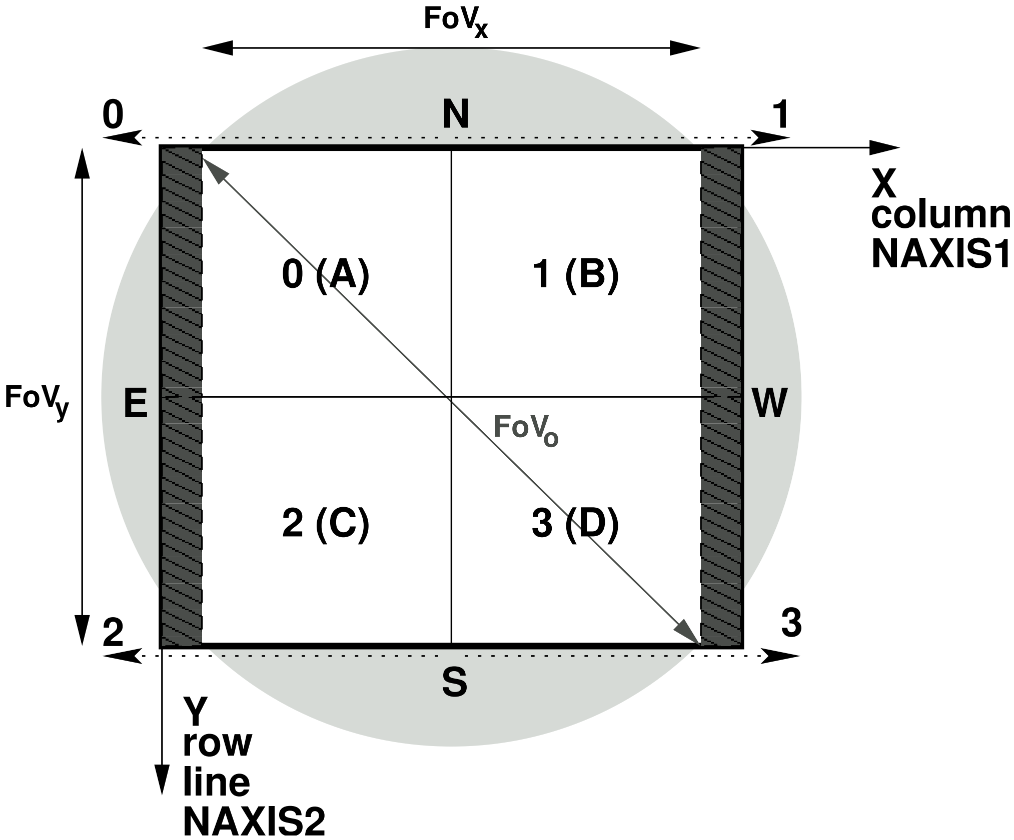

Figure 4.1: Coordinates and notation for the CCD in the ALIS images. The camera control unit reads out a line from each quadrant in parallel (along the dotted arrows 0–3). The pixels are then sent to the host computer, starting with quadrant 0. As this is finished, the next line is immediately read from the CCD. The host computer then sorts the pixels to form an image as indicated by the X and Y-axes in the figure. The approximate quarters (N, S, E, W) are only applicable to the fixed ALIS stations (i.e. not the bus). The quadrants are sometimes denoted 0–3 and sometimes A–D. The X-direction is also referred to as column or NAXIS1 and the Y-direction is sometimes referred to as row, line or NAXIS2. The shaded areas at the edges of the CCD indicate the bias-pixels, which are shaded from light. These are also called overscan-strip or reference-pixels. The optical field-of-view, FoV_o, is indicated with a grey circle and is measured diagonally across the CCD. The illuminated CCD (white) defines the field-of-view in x-direction, FoV_x, and the field-of-view in y-direction, FoV_y, (refer to Table 4.6).

As mentioned initially, to further enhance the bias removal, it is also possible to obtain k bias-frames (Typically at least 25 images), resulting in an averaged bias-correction image, $B_{\overline{Z}ij}$.

$$\forall(i,j):\ B_{\overline{Z}ij} = \frac{1}{k}\sum_{1}^{k}\left(DN_{Zij} - B_{Lj} - B_q - B_0\right)\ \text{[counts]} \tag{4.2}$$

This correction is normally only present when calibrating the imagers.

4.1.2 Dark-current

Correction for the dark-current is performed by taking several dark-exposures, i.e. long exposures ($t_{int} \geq 600$ s) with the shutter closed. The dark-current correction image, D_{ij}, is then produced by averaging these images together in much the same way as the averaged bias-correction image (Equation 4.2):

$$\forall(i,j):\ D_{ij} = \frac{1}{k}\sum_{1}^{k}\frac{1}{t_{int,k}}\left(DN_{Dij} - B_{\overline{Z}ij} - B_{Lj} - B_q - B_0\right)\ \text{[counts]} \tag{4.3}$$

Here $t_{int,k}$ is the integration time for image k.

However for the ALIS imagers, this correction has been found to be negligible for integration times less than 10–15 minutes. Therefore, no dark-current correction is made except for very special cases.

4.1.3 Flat-field correction

The purpose of the flat-field calibration is to remove multiplicative variations introduced by pixel-to-pixel sensitivity differences, vignetting in the optics, variation in transmittance on the filter surface, etc.. This is done by taking a large number of images of a uniform flat-field source:

$$\forall(i,j,\lambda):\ F_{ij\lambda} = \frac{1}{k}\sum_{1}^{k}\frac{1}{t_{int,k}}\left(DN_{Fij\lambda} - B_{\overline{Z}ij} - B_{Lj} - B_q - B_0 - D_{ij}\right) \tag{4.4}$$

In this equation $F_{ij\lambda}$ is the flat-field correction. The index, λ, indicates that the flat-field correction images should be obtained for each wavelength of interest. Normally this means one set of flat-field images per filter. However a calibration facility which can take measurements for several wavelengths within the filter passband would enable measurements of the combined effects of transmittances (Section 3.1.3) and quantum efficiency (Section 3.1.6) for the entire imaging system (and as a function of wavelength).

The moderate fields-of-view (50°–60°) for the ALIS imagers necessitate an integrating sphere of a sufficient diameter for flat-field calibration [i.e. about 1.5–2 m, see *Brändström*, 2000; Labsphere, 1997, and references therein.].

Numerous attempts were made to use simpler methods, such as cloudy skies, white screens, diffuse spherical lamp covers etc. to obtain reasonably good flat-field images. None of these attempts provided flat-field images of sufficient quality, as non-uniformities and gradients were hard to avoid with these simple approaches.

4.1.5 Summary

The corrections discussed above (apart from the bad-pixel interpolation) are summarised in the following equation:

$$\forall(i,j):\; DN'_{ij} = \frac{F_{ij\lambda}}{t_{int}}\left(DN_{ij} - B_{\overline{Z}ij} - B_{Lj} - B_q - B_0 - D_{ij}t_{int}\right) \qquad (4.5)$$

Here, DN'_{ij} is the corrected pixel value, which is normalised with respect to integration time t_{int}.

For most measurements, the following, simplified correction is applied

$$\forall(i,j):\; DN'_{ij} = \frac{F_{Mij\lambda}}{t_{int}}\left(DN_{ij} - B_{Lj} - B_q - B_0 - D_{ij}t_{int}\right) \qquad (4.6)$$

The symbol, $F_{Mij\lambda}$ is the modelled flat-field correction, as discussed in Section 4.1.3.

Apart from the steps described above, occasionally some additional steps are carried out in order to prepare the data for subsequent analysis. These include various types of filtering to remove cosmic-ray events, stars, etc.

4.2 Intercalibration

Intercalibration is carried out in order to be able to compare measurements from different instruments. To facilitate this, three radioactive ^{14}C light-standards and a calibration lamp are used (Figure 4.2). These light-standards are intercalibrated against other light standards during European calibration workshops held at regular intervals [for example *Lauche and Widell*, 2000a,b; *Widell and Henricson*, 2001]. As several of the light-standards used at these intercalibration sessions are traceable to National Bureau of Standards (NBS) sources, it is thus also possible to perform absolute calibration [*Torr and Espy*, 1981]. Results from some of the most recent calibration workshops are summarised in Table 4.3. For the ^{14}C-sources in use for calibrating ALIS (phosphors: 920B, L1614 and Y275) the column emission rate is plotted against wavelength in Figure 4.3. Table 4.4 presents the ratios of column emission rates from the latest calibration workshop (Oulu, 2001) to earlier calibration sessions. Despite the 5730 years half-life of ^{14}C, deviations of 10–20% are present, even within a couple of years as also noted by *Kaila and Holma* [2000]. This is probably related to either errors in the intercalibration procedure, or to the light-emitting phosphor of the sources.

The original use of these light-standards has been to calibrate photometers. This has been done by placing the light-standard on top of the front-lens of the photometer, covering the entire field-of-view. The same procedure was followed when calibrating the ALIS imagers. As the light-emitting surface of the calibrator does not cover the entire field-of-view of the imager, this method has been questioned [*Gustavsson*, 1997]. Therefore, during the latest calibration workshop, the light sources were placed at a larger distance (within focus) of the imager. However due to various technical problems, the results were inconclusive. Therefore this question remains open.

Sources		**Column emission rate [R/Å] at Filter [Å]**						
calibration	year	3914	4280	4866	5573	5882	6299	6562
Esrange, tungsten lamp								
Stockholm	2000	1.3	4.1	30	212	310	532	553
Oulu	2001	0.53	1.5	11.6	82	122	233	171
IRF, UJO 920B								
Lysebu	1985	5.1	126.0	61.5	18.6	10.5	6.7	8.1
Lindau	1999	4.4	102	60	22	12	7.6	2.4
Stockholm	2000	4.6	109	64	23	12.7	10	8.5
Oulu	2001	5.2	105	65	22	13	9.2	1.2
IRF, UJO L1614								
Lysebu	1985	0.07	0.73	32.5	27.7	8.7	2.5	4.3
Lindau	1999	0.6	1	37	33	9.3	1	2
Stockholm	2000	0.07	1.0	40	35	9.6	0.36	0.57
Oulu	2001	0.1	1.1	38	27	7	1.2	10.2
IRF, UJO Y275								
Lysebu	1985	0.03	0.3	3.8	251.0	378.0	217.0	113.0
Lindau	1999	0.01	0.2	3.8	263	383	282	165
Stockholm	2000	0.01	0.22	3.9	276	405	282	181
Oulu	2001	0.002	0.18	3.6	258	482	274	155
Mike Taylor, source								
Stockholm	2000	0.03	0.98	6.8	10	1.8	0.3	2.5
Sodankylä, blue lamp								
Lysebu	1985	2.0	6.0	10.1	9.9	15.3	4.0	0.66
Lindau	1999	2.3	7.2	12	9.3	10	7.5	7.2
Stockholm	2000	2.5	7.3	12.5	9.3	9.5	6.3	2.8
Oulu	2001	2.6	7.6	12	8.9	13	10	12
Sodankylä, tungsten lamp								
Lysebu	1985	0.12	0.71	5.4	31.8	62.8	125.8	137
Lindau	1999	0.1	0.75	5.6	33.5	65	137	192
Stockholm	2000	0.10	0.65	5.2	31	61	139	285
Oulu	2001	0.01	0.6	5	30	75	133	248
IRF, tungsten lamp								
Stockholm	2000	0.19	1.1	8.5	50	98	223	454
Oulu	2001	0.17	1.2	8	48	115	228	428
MPI-2 lamp								
Lysebu	1985	0.02	0.16	2.43	193.7	290.7	191.8	98.2
Lindau	1999	0.03	0.12	2.2	172	258	213	235
Stockholm	2000	0.01	0.13	2.3	175	266	153	105
Oulu	2001	0.01	0.01	2.3	169	251	193	105
S.Chernouss, Glow lamp								
Oulu	2001	13	143	66	84	374	392	59
S.Chernouss, Tungsten								
Oulu	2001	0.01	1.6	5.5	36	293	947	679

Table 4.3: Results from a selection of recent intercalibration workshops: The column emission rates are given in [R/Å] (Rayleighs/Ångström). (Some sources have been omitted in order to fit the table on one page.) [after *Lauche and Widell*, 2000a,b; *Widell and Henricson*, 2001, and earlier calibration workshop reports]

4.2.1 Absolute calibration

The digital-output, DN_{ij}, and number of generated photo-electrons per pixel $\overline{n}_{e^-_{\gamma ij}}$ is related by:

$$DN_{ij} = G_S \, \overline{n}_{e^-_{\gamma ij}} \text{ [counts]} \tag{4.7}$$

where G_S is the imager system gain, [*Preston*, 1993, 1995]:

$$G_S = \frac{G_{CCD} \, G_P \, t_{DCS}}{B_{ADC} \, \tau_{DCS}} \left[\frac{\text{counts}}{e^-_\gamma}\right] \tag{4.8}$$

Here, G_{CCD} is the CCD output sensitivity, G_P is the programmable gain setting (5 or 10), t_{DCS} is the DCS integration time, B_{ADC} is the ADC bit weight (90.6 μV/counts), and τ_{DCS} is the DCS integrator time constant. These parameters are configured during CCU start-up (Section 3.3.3).

Combining Equation 4.6 with Equations 3.20 and 3.22 yields for uniformly illuminated central pixels of the CCD, DN_{Cij} :

$$\frac{I_{cal}}{DN_{Cij}} = \frac{1}{t_{int}} \frac{16 f_{\#}^2}{10^{10} \, G_s \, Q_E \, T \, A_{pix}} \left[\frac{R}{\text{counts}}\right] \tag{4.9}$$

The "known" column emission rate, I_{cal}, which is obtained from a light-standard by integrating over the filter passband, $\lambda_1 \cdots \lambda_2$ is given by:

$$I_{cal} = \int_{\lambda_1}^{\lambda_2} I_{ls}(\lambda) \, d\lambda \approx I_{ls}(\lambda_2 - \lambda_1) = I_{ls} \, \Delta\lambda \, [R] \tag{4.10}$$

Here, the column emission rate of the light standard, $I_{ls}(\lambda)$, is a function of wavelength λ, that must be integrated over the filter passband, $\Delta\lambda$. However during the intercalibration workshops, $I_{ls}(\lambda)$ is measured only for one wavelength in the filter passband, hence the approximation in Equation 4.10 (see Table 4.3 and Figure 4.3).

Now, consider the right-hand part of Equation 4.9. The quantum-efficiency, transmittance and system gain is a function of wavelength and pixel-coordinates among other things, such as for example filter-temperature (i.e. $Q_E = Q_E(\lambda, i, j, \ldots)$, $T = T(\lambda, i, j, \ldots)$ and $G_S = G_S(i, j, \ldots)$). Due to the difficulties of determining these functions as well as the approximations and uncertainties related to the $f_{\#}$ Equation 4.9 is rewritten as follows:

$$\frac{I_{cal}}{DN_{Cij}} = \frac{1}{t_{int}} C_{abs\lambda c} \, F_{ij\lambda} \left[\frac{R}{\text{counts}}\right] \tag{4.11}$$

Here $F_{ij\lambda}$ (Equation 4.4) corrects for both the dependence on pixel-coordinates as well as on wavelength for a particular filter. (The index λc in the absolute calibration constant, $C_{abs\lambda c}$, indicates that the constant is unique for each filter of each imager c). Hence, *the importance of a proper flat-field calibration cannot be underestimated* (Section 4.1.3). Unfortunately, a proper flat-field calibration is not yet available for ALIS, and some approximations are required:

$$\frac{I_{cal}}{DN_{Cij}} \approx \frac{1}{t_{int}} C_{abs\lambda c} F_{Mij\lambda} \int_{\lambda 1}^{\lambda 2} T'(\lambda) d\lambda \approx C_{abs\lambda c} F_{Mij\lambda} \left[\frac{R}{\text{counts}}\right] \tag{4.12}$$

where $\overline{DN}'_C$ is obtained by averaging together a number of uniformly illuminated pixels in the central part of the image.

The present more approximative calibration is described by Equations 4.6 and 4.12:

$$C_{abs\lambda c} \approx \frac{1}{\overline{DN}'_C} \int_{\lambda_1}^{\lambda_2} I_{ls}(\lambda)\, d\lambda \int_{\lambda 1}^{\lambda 2} T'(\lambda) d\lambda \approx \frac{I_{ls}\Delta\lambda}{\overline{DN}'_C} \left[\frac{R}{\text{counts}}\right] \tag{4.14}$$

Hence, an absolute-calibration must be carried out for each filter of each imager.

The results from the two most recent absolute calibrations of the ALIS imagers are found in Table 4.5. As can be seen, the last absolute calibration of the ALIS

`ccd` `cam`	λ_{cw} [Å]	$\Delta\lambda$ [Å]	$\overline{DN}'_C$ [counts]	$\langle DN'_C \rangle$ [counts]	96-07-10 $C_{abs\lambda c}$ [R/counts]	97-05-21 $C_{abs\lambda c}$ [R/counts]	2001 adj. $C_{abs\lambda c}$ [R/counts]
1	5590	40	217.5	2.6	32.4	46.2	47.4
1	6310	40	173.4	2.6		50.1	63.2
1	6230	40	254.2	2.9		34.1	43.1
1	4285	50	116.8	3.4		53.9	44.9
2	5590	40	300.6	3.6	28.2	33.4	34.3
2	6310	40	339.3	3.5	25.6	25.6	32.3
3	5590	40	484.2	4.1	21.9	20.7	21.3
3	6310	40	427.3	2.8	22.2	20.3	25.6
4	5590	40	468.0	5.3	23.7	21.5	22.1
4	6310	40	402.2	4.1	23.7	21.6	27.3
5	5590	40	333.8	4.0		30.1	30.9
5	6310	40	390.5	4.2		22.2	28.1

Table 4.5: Calibration results from ALIS obtained in 1996 and 1997. The large difference for `ccdcam1` occurs because it was equipped with filter-wheel and new optics between these calibrations. Some filters (see Tables 3.4 and 3.5), as well as `ccdcam6` were not yet available during these calibrations. Both calibrations used the Lysebu, 1985 intercalibration. The last column gives values of the calibration of 21 May 1997, adjusted by the 2001 intercalibration result (Table 4.3). Finally it should be noted that no suitable light-standard for calibration of the 8455 Å filters is available.

imagers was carried out in 1997. At that time `ccdcam6` was not yet delivered; neither were all filters available. Also no suitable light-standard is available for the near-infrared 8446 Å emission line. An attempt was made to perform a recalibration of all imagers and filters in 2001. However this effort failed due to technical problems and limited time. Hence a new calibration must be performed as soon as possible.

A comparison of auroral measurements from `ccdcam6` and a Russian photometer (calibrated in Russia) both co-located in Kiruna indicates a disagreement in absolute intensities of $\approx 20\%$ between the two instruments [*Sergienko*, 2003]. This comparison as well as extrapolated values have been in use for the filter/imager combinations not appearing in Table 4.5 (i.e. `ccdcam6`. See also Tables 3.4 and 3.5).

There is furthermore an interesting possibility of performing absolute calibration by using known spectra of stars, which has been done for the 8446 Å

4.2.3 Related issues

On-chip binning

The absolute calibration has been found to scale accurately with the binning factors, thus:

$$C_{abs\lambda c,binxy} = \frac{C_{abs\lambda c}}{x_{bin} \times y_{bin}} \tag{4.16}$$

Where $C_{abs\lambda c,binxy}$ is the absolute calibration constant with binned pixels, x_{bin} is the binning-factor in the x-direction, y_{bin} is the binning factor in the y-direction.

Linearity

As no variable light-standard is available, the linearity has been checked by varying the integration time (t_{int}). As expected, the CCD detector appears to be completely linear until it reaches the saturation-equivalent exposure (Section 3.1.10).

Interference filters

Both the transmission characteristics and passband of a narrow-band interference filter are subject to aging effects. The filter-wheels of the ALIS imagers are also sometimes subject to high temperatures due to day-time sunlight. This is known to have a permanent degenerative effect on the filters. Questions have therefore been raised regarding the long-term stability of the filters. To clarify these issues, it would be desirable to re-measure filter characteristics for the filters. This was planned for the autumn of 2001, but had to be postponed for a number of reasons.

Another concern is to measure the transmittance of the filter, $T_f(i, j, \lambda)$, as a function of pixel indices, (i, j), (columns, lines). A monochromator system for filter transmission measurements was developed for ALIS [*Vaattovaara and Enback*, 1993]. Provided that an ALIS imager has a valid flat-field calibration, it should in principle be possible to check the transmittance of the optical system (including the filter) as a function of wavelength and pixel coordinates. Such a study would be beneficial for all optical instruments, using interference filters, and could provide answers to questions posed by *Kaila and Holma* [2000] regarding absolute calibration of wide field-of-view photometers and camera systems.

4.3 Geometrical calibration

The task of mapping the field-of-view of each pixel to the observed object is called geometrical calibration. As this topic is extensively covered in *Gustavsson* [2000, Chapter 4–5] it will only be briefly touched upon here. First a set of star-images are obtained for the viewing direction under consideration. Then the positions of the stars are calculated from a star-catalogue (Bright Star Catalogue (BSC))* and mapped down to the image coordinates. Then preferably more than 100 stars, evenly distributed across the image, are identified. Finally a transfer function is adjusted so that the calculated and actual positions of the stars overlap. This

*ftp://adc.gsfc.nasa.gov/pub/adc/archives/catalogs/5/5050

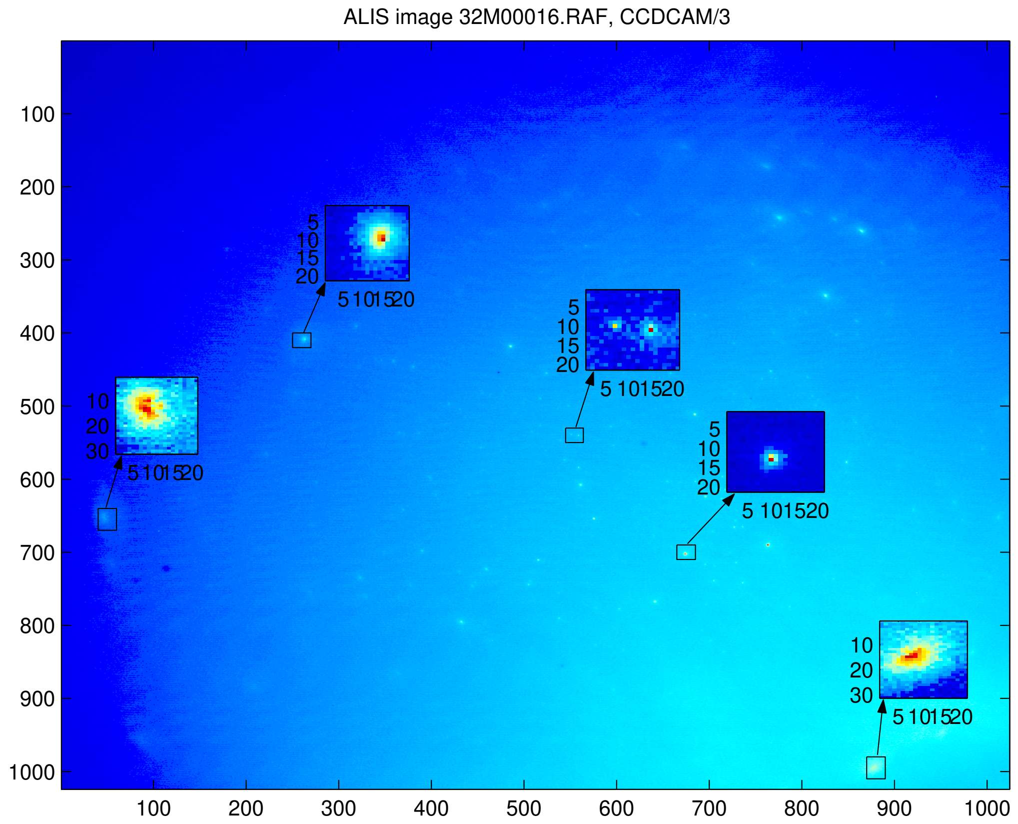

Figure 4.5: A typical ALIS background image with a selection of magnified stars displaying the variation of the point spread function (PSF) over the image. [after *Gustavsson*, 2000, Figure 5.6].

superfluos. If that had been known in advance, those resources could have been spent on other tasks.) The development of a control system for ALIS was therefore carried out by successive approximation and "survival of the fittest" ideas. The following sections will provide a brief overview of a vast subject that is best described by running ALIS and studying the source code.

5.1 Making an observation with ALIS

Experience has suggested the following steps for configuring ALIS for an observation:

1. **Defining a scientific rationale:** This is of course the first and most important task. Naturally it is almost impossible to predict the outcome of any observations. Nevertheless, well planned measurements with a clear view of what needs to be done tend to yield better results than "ad hoc" operations.

2. **Selecting stations:** Normally it is best to use as many stations as possible, but there might be observation schemes that require only a subset of the stations. It is also important to plan what changes to the rationale are necessary in case some stations cannot take part in the observation (for example due to clouds or technical problems).

3. **Selecting imager viewing directions:** This can be either the standard preset viewing-directions (Figure 3.11 and Table 3.6) or specially calculated viewing directions for a particular measurement. It is advisable to prepare a strategy for possible changes if the observed phenomena moves outside of the field-of-view. In most cases it is best to avoid changes of the viewing directions during a measurement. "Chasing the aurora" usually results in poor data. Another concern is to make sure that the selected positions are geometrically calibrated against the star background (Section 4.3).

4. **Selecting filters:** Filter selection usually follows directly from the scientific rationale. However all filters are not available at all stations (see Tables 3.4 and 3.5). Filter change time increases with the distance between the filters on the filter-wheel (nominally 1–2 s). It might also be necessary to obtain background intensities by exposing images with background filters.

5. **Selecting integration times:** The minimum integration time is defined by the shortest exposure resulting in an acceptable *SNR*. As the spectral sensitivity varies for the imager, there is normally a need for longer exposures for shorter wavelengths. Maximum exposure is defined by the longest exposure without saturating the CCD, or, more frequently, by requirements set by the desired temporal resolution. The risk of saturating the CCD must be considered at high binning factors as the sensitivity increases with the binning factors (Figure 3.4). Occasional saturated images pose no threat to the CCD, but yield unusable data. Finding an optimal integration time has proven to require large amounts of experience from earlier measurements. (see also Chapter 3)

on taking scientific decisions and possibly one who coordinates with other instruments. Taking good notes is essential, as analysis might not occur until months later.

14. Retrieve the raw-data from the stations: It is time-consuming to retrieve raw-data from the stations. All six stations can be visited in less than a week, but this requires a lot of driving. Usually the disks are brought back only during scheduled maintenance trips to the stations, or as the disks become full. If exceptionally interesting data have been recorded, it might still be desirable to retrieve it as quickly as possible.

15. Analysing and publishing the results: First one needs to select data, then this data-set must be preprocessed and calibrated before the actual analysis and publication phase starts. These final steps rely on good record-keeping in the previous steps.

5.1.1 Modes of operation

The modes for controlling ALIS are summarised below:

Manual control: By sending commands directly to ALIS, a user is able to control observations interactively. This mode of operation is most frequently used for checking observing conditions (cloudiness, etc.), for troubleshooting and for maintenance.

Semiautomatic operation: In this mode a user controls ALIS by running observation control programs (usually these are shell-scripts at the stations) that are uploaded, prepared and tested in advance. This is the normal operating mode.

Automatic operation: In this mode, an observation control program is loaded and run automatically at a predefined time. This mode can easily be switched to semi-automatic mode if the user wishes to change anything. Exceptions can be reported using a paging system if the control centre is unmanned. Due to the vast amounts of data produced, automatic measurements are uncommon.

5.1.2 Alarms and other exceptions

Many exceptions can be properly acted upon automatically, while others require manual interaction. These exceptions trigger alarms, which are displayed at ALIS-CC and at all user interfaces. If user interface is active, an automatic paging system will also alert the operator on duty. Typically, a pager call occurs for A-Alarms or fatal alarms, (see below) but the paging system can be configured to alert a user when an interesting measurement situation is emerging, etc. ALIS exceptions are classified in three alarm categories:

Fatal alarms: Fire, trespass or other severe conditions threatening the hardware.

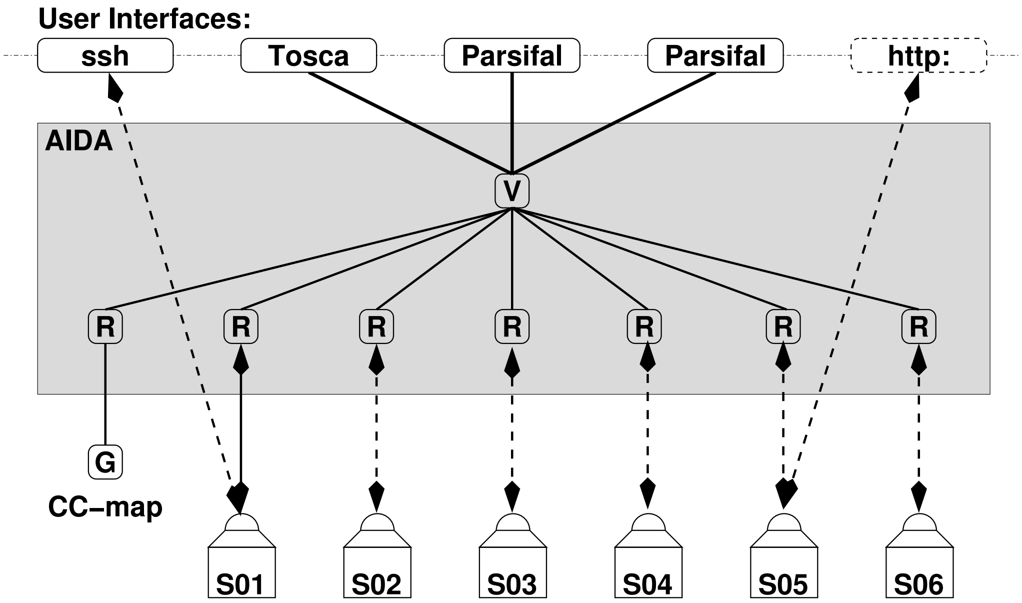

Figure 5.1: Block diagram of OPERA. Any number of user-interfaces (`parsifal`, `tosca`) can connect to AIDA in order to control ALIS. In AIDA a central supervising process V (`verdi`) routes all information between the different user-interfaces and the stations. The stations are connected to `verdi` via an interface process, R (`radames` controls a RS-232 serial line and a modem, or `rigoletto` that provides a TCP/IP connection to a station over an existing network connection). The control centre status display map (Figure 2.7) is connected in the same way as an ALIS station. The user-interfaces labeled `ssh` and `http` indicate the possibility to control the stations over a shell-login, or from a standard web-browser. This will eventually make the control centre software superfluous, as the functionality of AIDA will be available at each station.

and error-recovery functions. If the station computer is shut-down or malfunctioning, the housekeeping unit will take over the communication line and alert the control centre about the error condition at the station. It is then possible for the operator at the control centre to communicate directly with the housekeeping unit to diagnose the situation and often resume normal operation in less than ten minutes.

`ntpd` This freely-available daemon controls station timing (Section A.5).

NIPU software: Software for the Transputers in the NIPU are uploaded at NIPU start-up by the `nipu` program at the station computer. The NIPU software was written in Occam and Transputer-C.

Figure 5.2 presents the interrelationships of the various software at the stations superimposed onto a block-diagram of an ALIS station (Appendix A).

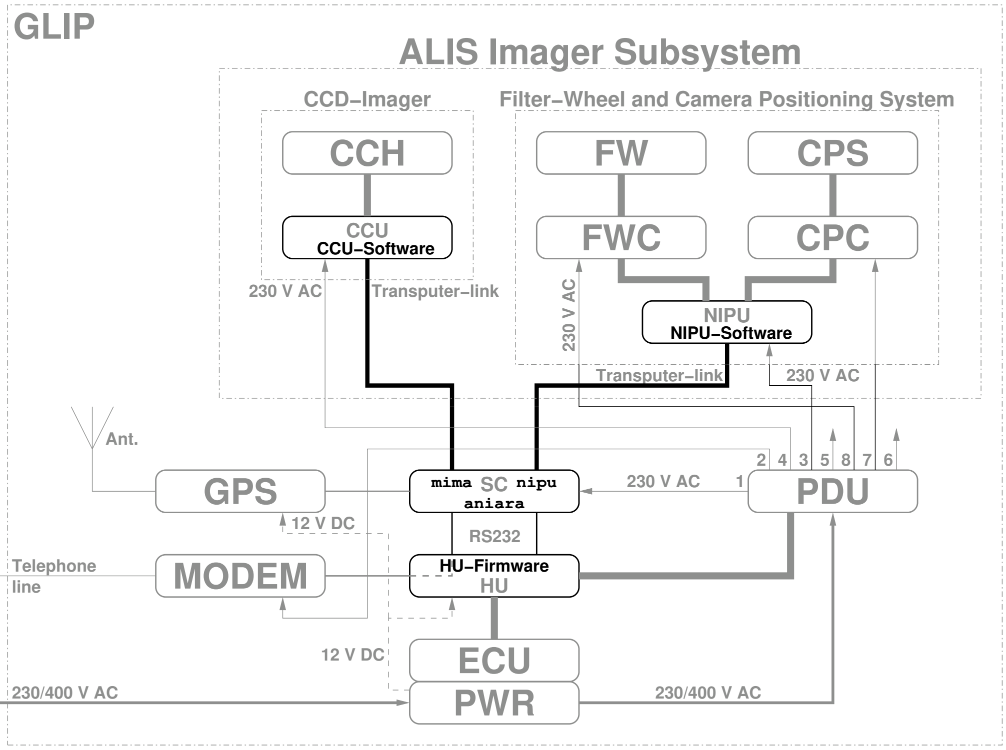

Figure 5.2: ALIS station software superimposed onto the block-diagram of an ALIS station (refer to Figure A.1 in Appendix A); `mima` uploads the vendor-provided CCU-software and controls the imager; `nipu` uploads the NIPU software and controls the CPS and FPS; `aniara` is the main station-control program. The housekeeping unit is controlled by firmware in an EPROM.

5.2.4 Experiences and future plans

ALIS software has now existed for over a decade. During the early years, technical obstacles, and in particular problems related to the many limitations of the

from ALIS. This division of responsibilities appeared naturally in a small group with a large and technically complex project.

6.1 Scientific objectives of ALIS

The list below tries to summarise the scientific objectives of ALIS, from the first proposal [*Steen*, 1989] until the present time.

Non-stable auroral forms: Auroral events such as: substorm onsets, Westward Travelling Surges (WTS), surges, folds, spirals (or auroral vortices), rays and omega bands, and the not well-understood pulsating and flickering aurora belong to this category. These phenomena require observations with high temporal and spatial resolution. So far, ALIS has been used infrequently to make this type of observations, due to a combination of technical limitations (Section 3.3.4), as well as difficulties related to the scientific understanding of these phenomena. However, a theoretical paper on auroral vortices was published (Section 6.5.3).

Stable auroral forms: The stable auroral arc has been the topic for many studies during the last five decades. Despite this, the ionospheric environment in and around it is not yet fully understood. Detailed field-aligned measurements of ionospheric parameters combined with tri-static plasma-drift measurements by EISCAT, produce profiles on electron density, electron and ion temperatures ranging from some 90 km to 1000 km, as well as, horizontal electric-field estimates in the ionospheric F-region. To relate such measurements to the optical data from ALIS, as well as to satellite and other ground-based instruments would increase the scientific yield of studies of stable auroral forms. Some results of such coordinated observations with ALIS, EISCAT and the FAST satellite are discussed in Section 6.5.2. Another stable auroral form is the *diffuse aurora*, (added to the scientific objectives in *Steen et al.* [1990]) where the equatorward edge of the diffuse aurora has been used to estimate the size of the auroral oval. The main ionospheric trough is often associated with the equatorward edge of the auroral oval. Examples of "accidental" measurements of the trough are discussed in Section 6.5.4. Other studies (however, not always of stable aurora) that could be included here are : enhanced aurora [*Hallinan et al.*, 1985], black aurora, statistical studies of arc-thickness etc.

Characteristic energy of particles: By the use of spectroscopic ratios, the characteristic energy of the precipitating particles can be obtained [*Hecht et al.*, 1989; *Meier et al.*, 1989; *Strickland et al.*, 1994; *Rees and Luckey*, 1974]. To do this properly would require simultaneous measurements at two wavelengths at each station, thus doubling the data-flow and requiring at least two imagers at each station. Results obtained so far involve a single camera at each station and rapid filter changes (Section 6.5.1).

A 3-D image: Since the fields-of-view of the ALIS stations overlap, it is possible to estimate the altitude distribution of auroral emissions by utilising triangulation and tomographic inversion techniques. *Steen* [1989] expected

Package name	*Description*
`Camera`	The cornerstone package, providing a set of functions for a black-box-model of the imaging process, mapping functions, as well as functions for manual and automatic stereoscopic triangulation.
`Starcal`	A tool to determine the characteristics of the camera-models and rotations by combining the information that can be obtained from images with the positions of the stars in the sky.
`Skymap`	A medium accuracy star-chart, used by `Starcal` to calculate the positions of the stars.
`EARTH`	A set of earth model functions based on WGS-84.
`Fits_tools`	A small toolbox for reading and pre-processing FITS image data.

Table 6.1: Summary of image processing tools provided by Björn Gustavsson at `http://www.irf.se/~bjorn/Starcal/`. They provide a small and self-contained set of functions for camera calibration as well as single and multi-viewpoint image data analysis. These tools are primarily intended for middle and upper atmospheric physics as well as for auroral research. (Quoted from: `http://www.irf.se/~bjorn/Starcal/Documentation/` see also *Gustavsson* [2000].)

6.2 ALIS data analysis

The primary raw-data output from ALIS is multi-station image data in FITS format (Section 2.2.5). Currently, the main part of the data-analysis software for ALIS includes programs for correcting the images, calibrations against the star background, auroral tomography and triangulation, spectroscopic and absolute measurements, etc. Most of the programs are written in Matlab and C, but some work was also carried out in IDL, NOAO/IRAF as well as other common image-processing environments. The main authors of the current data-analysis software for ALIS are Björn Gustavsson (see Table 6.1) and Peter Rydesäter (see Table 6.2). Carl-Fredrik Enell has developed additional tools for the analysis of PSC data [PSCWorks, see *Enell*, 2002, Appendix B]. A combination of the data-analysis tools mentioned was utilised to analyse nearly all of the observations summarised in this chapter.

6.2.1 Investigations of new data-analysis methods for ALIS

As ALIS produces large amounts of data, studies have been carried out to investigate various new and partly automated approaches to the problems of image processing, pattern recognition and image classification. Some references to published works on ALIS are presented below, however, this field is to a large extent highly experimental in nature and therefore these results are not included in the standard analysis of ALIS data.

To classify auroral images is not a straight-forward task. As noted by *Brändström et al.* [1998] it is sometimes difficult, even for an experienced observer, to discriminate between for example diffuse aurora and aurora behind thin clouds (Figure 6.1).

Figure 6.1: An example of the difficulties of auroral image classification. In this image, clouds, stars, diffuse and black aurora are seen. [After Figure 8 in *Brändström et al.*, 1998]

1997] which, to some extent, possesses similar image processing and classification problems as encountered in auroral imaging. A three-step procedure for automatically classifying auroral images is outlined: (1) use a PCNN for image segmentation, (2) post-process the resulting data, either by using Singular Value Decomposition (SVD) or by applying a second PCNN for feature extraction, (3) carry out the actual classification using a traditional neural network. This work was followed up by *Rydesäter et al.* [1998] who concentrated on the problem of how to find auroral arcs, and on their location within the images. For this purpose an arc detection algorithm was constructed and tested. Initial attempts were made to enhance the algorithm with a Radial Basis Neural Network (RBNN). It was concluded that the arc detection algorithm gave a robust detection of auroral arcs and their direction. Preliminary results from the application of a RBNN was promising.

Alpatov et al. [2000] applied self-organising neural networks to ALIS data, for the detection of polar stratospheric clouds.

A different approach to the problem of automatic recognition of auroral forms is studied by *Pudovkin et al.* [1998]. Here a more traditional method, based on the analysis of isolines of auroral luminosity shapes is utilised. Classical forms such as ellipses, spirals and folds appear to be confidently retrieved. However, *Pudovkin et al.* [1998] notes that the entire field of auroral classification seems to be at an early stage: "There are needs for extensive and purposeful studies of the forms peculiar to certain geophysical conditions, with the nature of the physical process within the auroral plasma and their characteristic time and space scales being taken into account."

Rydesäter [2001] presents a survey of possible methods of implementing a Selective Imaging Technique (SIT) functionality in ALIS, as proposed by *Steen et al.* [1997a]. (This would be an algorithm or a device that automatically controls ALIS, or advises the operator to acquire data of specific interest when favourable conditions occur.)

A study on the effects of lossy compression of auroral image data is presented in *Rydesäter et al.* [2001]. At least for the images studied, it appears to be possible to compress images to approximately 5–12% of their original size without increasing errors.

Another topic is the study of the fractal dimension of auroral features. An initial study was carried out by *Alpatov et al.* [1996a,b]. It was concluded that fractal analysis methods can be used to segment auroral images into aurora, stars, clouds and background. However it remains to be seen if segmentation of the auroral features themselves can be related to physical processes responsible for the aurora.

Despite the fact that these studies provided promising preliminary results, much work remain before these methods can be applied to auroral imaging on a regular basis.

Apart from the work related to ALIS, many other groups are working in this field. An example of this is the very promising work by *Syrjäsuo* [2001, and references therein] on auroral detection/classification by automated image analysis.

Research (NIPR), Tokyo. During a joint campaign (ALIS-Japan 1) held in March 1996, the first results of auroral tomography were obtained as reported in *Aso et al.* [1998a]. At this time ALIS had only three imagers, and two additional intensified CCD-cameras were provided by our Japanese colleagues [*Aso et al.*, 1993, 1994], resulting in a total of five imaging stations. A modified MART was used for tomographic analysis, presenting initial results of tomography for a folded arc, and a double-arc system [*Aso et al.*, 1998a]. An auroral model with a folded arc is also discussed in this paper.

In *Aso et al.* [1998b] initial results and model comparisons using a modified version of a Simultaneous Iterative Reconstruction Technique (SIRT) [*Gilbert*, 1972] were applied to data from the March 1995 ALIS-Japan 1 campaign. The method was also verified by numerical simulations. An auroral fold occurring at 23:40:30 UTC on 26 March 1995 was selected for testing the tomographic analysis with the modified SIRT method assuming magnetic field-aligned auroral structures. Projecting back the reconstructed volume onto the original images reveals a disparity of about 10% or less. The modified SIRT method was found to be a promising CT application in the field of auroral studies. In total, four joint ALIS-Japan campaigns have been undertaken so far, and some of these data are still in the analysis phase.

Aso et al. [2000] reports on tomographic analysis of auroral images by the modified SIRT method. Auroral images were obtained on 9 February 1997 at 19:46:00 UTC in the $O(^1S)$ 5577 Å emission line as well as at 18:31:30 UTC in the N_2^+ 1Neg. 4278 Å emission line. The latter case showed a bright folded arc south of Kiruna and a faint thin arc north of Kiruna. The peak height of the intense aurora appears lower than the faint arc. Given favourable conditions for auroral tomography, it is possible to study the basic auroral formation process. To demonstrate this *Aso et al.* [2000] also performed a numerical simulation for the reconstruction of a slightly folded auroral structure using data from seven stations. Furthermore, the authors report on initial triangulation results applied to the studies of nacreous clouds. Some more reports of ALIS observations of nacreous clouds are summarised in Section 6.6.1.

Triangulation and tomography-like methods were applied to the studies of HF pump-enhanced airglow (Section 6.4). A solution to the inverse problem for a particularly ill-posed problem, with data from only three stations south of the emission region, is discussed in *Gustavsson et al.* [2001a].

In *Gustavsson et al.* [2001b] a constrained tomographic inversion was used to estimate the N_2^+ 1Neg. 4278 Å altitude distribution, which allowed an estimate of the energy distribution of the electron flux (Section 6.5.1).

This section has provided a rather brief summary of a very large subject. For further, more detailed studies, the reader is encouraged to read the cited papers, and, in particular, the main reference for three-dimensional imaging with ALIS by *Gustavsson* [2000].

Future developments to be expected in this field include the investigation of smooth basis functions and approximated projection algorithms for faster tomography [*Rydesäter and Gustavsson*, 2001].

6.4.1 The EISCAT Heating facility

The EISCAT Heating facility is located at Ramfjordmoen near Tromsø, Norway (69.6°N, 19.2°E, 86.3 m above sea level, L=6.2, magnetic dip angle I=78°) [*Rietveld et al.*, 1993]. The facility is located about 200 km north of Kiruna (See Figure 6.2). Up to 1.2 MW of CW power in the frequency range from 3.85 to 8 MHz can be generated by twelve transmitters of 100 kW each. There are three antenna arrays, covering the frequency ranges of 5.4-8 MHz, 3.85–5.65 MHz and 5.4–8 MHz. Array 1 has a beam width of 7° with a gain of 30 dB corresponding to 1200 MW Effective Radiated Power (ERP). Arrays 2–3 have beam widths of 14.5°, a gain of 24 dB and a maximum ERP of 300 MW. The main HF wave parameters such as frequency, polarisation, beam direction, and maximum power are chosen and set up at the time of tuning-up the transmitters. It is furthermore possible to modulate, power-step, change polarisation modes and to change the direction of the beam during an experiment [*Rietveld et al.*, 1993].

The EISCAT Heating facility enables strong excitation of plasma turbulence in a wide range of angles to the geomagnetic field. This is due to the fact that the pump electric field is directed parallel to the geomagnetic field at the reflection height, and essentially perpendicular to the magnetic field at only a few kilometres lower altitude [*Leyser*, 1991].

6.4.2 ALIS observations of enhanced airglow

Starting in 1995, a series of experiments were carried out, attempting to produce enhanced airglow with the EISCAT Heating facility, and to detect it with ALIS. *Stubbe et al.* [1982] noted that such experiments require: a sufficiently high ionospheric critical frequency, dark and clear skies, no auroral activity and a low or at least stable natural airglow background. As seen from Table 6.4 many events are yet to be analysed. In the following text emphasis will be on the 16 February 1999 event.

6.4.3 Observations on 16 February 1999

The first unambiguous observation of HF pump-enhanced airglow at auroral latitudes was made on 16 February 1999 [*Brändström et al.*, 1999]. This evening the skies were clear at most ALIS stations and there was no auroral activity ($K_p \approx 0$). ALIS operated between 16:15 and 18:30 UTC taking a new image every 10 s with 5 s integration time for the $O(^1D)$ 6300 Å emission line. The sensitivity of the CCD-cameras was enhanced 64 times by on-chip binning 8×8 pixels, thus reducing the spatial resolution from 1024×1024 pixels to 128×128 pixels. All ALIS-cameras were pointing towards the anticipated region of enhanced airglow. This is the so called "heating-position" (see Table 3.6 and Figure 3.11), centred at an altitude of approximately 250 km above the EISCAT Heating facility (Figure 6.2). Ten transmitters were operating with an output power of 85 kW each. Thus a total transmitted power of 850 kW, yielded an ERP of around 125 MW. The transmitted frequency was 4.04 MHz, reflecting in the ionospheric F-region, and the ordinary mode (O-mode) beam was tilted 6° south from the vertical (which is about half the angle between the vertical and the geomagnetic field

Dates	**HEA**	**Remarks**
1995 11-25	no	
1995 11-28	no	10 min on 5 min off
1995 11-30	no	
1998 11-18	no	
1999 02-16	yes	*Brändström et al.* [1999]; *Gustavsson et al.* [2001a]; *Leyser et al.* [2000]; *Sergienko et al.* [2000]
1999 02-18	?	
1999 02-19	?	
1999 02-21	yes	5577 Å, 6300 Å *Gustavsson et al.* [2003]
1999 02-22	no	
1999 03-15	yes	
1999 03-16	yes	
1999 03-17	yes	
2000 11-19	?	
2001 02-24	yes	
2001 03-19	no	
2001 03-21		Cloudy over ALIS but HEA reported by *Kosch et al.* [2002b]
2002 03-07	yes	Freq. stepping. 4278 Å, 5577 Å, 6300 Å
2002 03-10	yes	4 min on 2 min off 4278 Å, 5577 Å, 6300 Å, 8446 Å
2002 11-02–11-07	no	
2002 11-08	yes	Freq. stepping
2003 02-24–03-07	no	Too much auroral activity

Table 6.4: An overview of most HF pump-enhanced airglow experiments carried out with ALIS. The column HEA indicates if HF pump-enhanced airglow was observed. Question marks indicate uncertainty at the time of observation. As seen, the events which have proved most interesting so far are 16 February 1999 and 21 February 1999. Analysis and new measurements are still in progress as this is written.

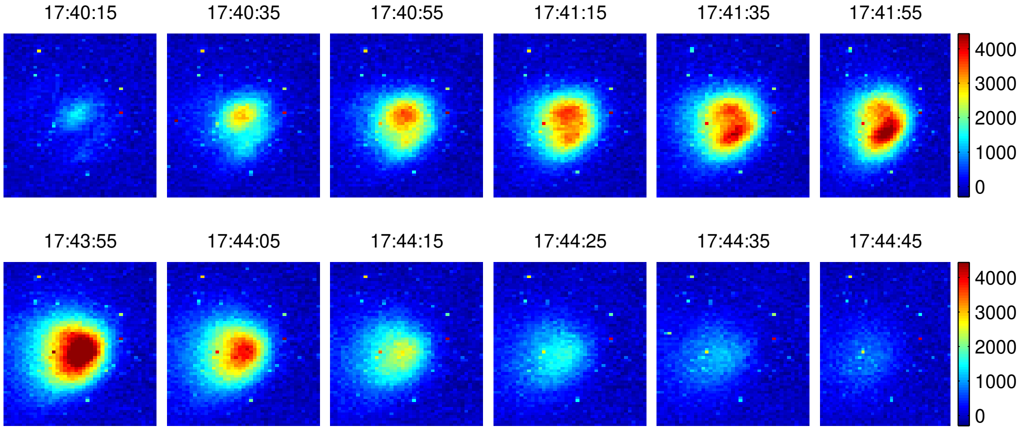

Figure 6.4: Sequence of airglow images from the Silkkimuotka ALIS station for 20 s intervals following transmitter-on at 17:40:00 UTC (top), and at 10 s intervals following transmitter-off at 17:44:00 UTC (bottom). The intensity scale is in raw counts. Two peaks of airglow intensification are clearly visible in the transmitter-on sequence. [After Figure 3 in *Brändström et al.*, 1999]

background ionosphere, which drift through the transmitted beam.

A series of images of the airglow intensity is shown in Figure 6.4. Transmitter-on occurs at 17:40 UTC, beyond which the airglow region and intensity is seen to slowly grow, forming two peaks. The upper one appears to saturate, after which the lower peak underneath intensifies, and eventually merges with the first peak. Transmitter-off occurs at 17:44 UTC, beyond which the airglow slowly decays. The peak intensity was estimated to be approximately 300 ± 100 R. (See Section 4.2.1, regarding the estimated error of the absolute calibration).

Figure 6.5 shows data from the Silkkimuotka station obtained near transmitter-on at 17:48:00 UTC and -off at 17:52:00 UTC. Both the intensity and size of the patch are seen to slowly increase after transmitter-on, and to decay slowly after transmitter-off.

From Figure 6.3 it is seen that simultaneous data from up to three stations exist for some time periods. This enables triangulation of the height of the airglow region. As shown in the top panel in Figure 6.6, the typical height of the maximum emission was found to be 230–240 km from 17:32 UTC to 18:08 UTC. For the transmitter-on at 18:12 UTC, the enhanced airglow altitude is 250-260 km. In the bottom panel it is shown that the airglow region was positioned approximately 160–170 km to the north of Kiruna and 50 km to the west.

In Figure 6.7, it is seen that the initial location of the two interaction regions are approximately 20–30 km apart. The initially more intensive northernmost region of excitation is fairly immobile, while the southernmost moves 30 km northward in 4 minutes corresponding to a velocity of 100 ± 20 m/s [*Gustavsson et al.*, 2001a].

Also, the ionospheric F-region neutral wind was measured by Fabry-Perot interferometers (FPI) [*Aruliah et al.*, 1996; *Gustavsson et al.*, 2001a]. Figure 6.8

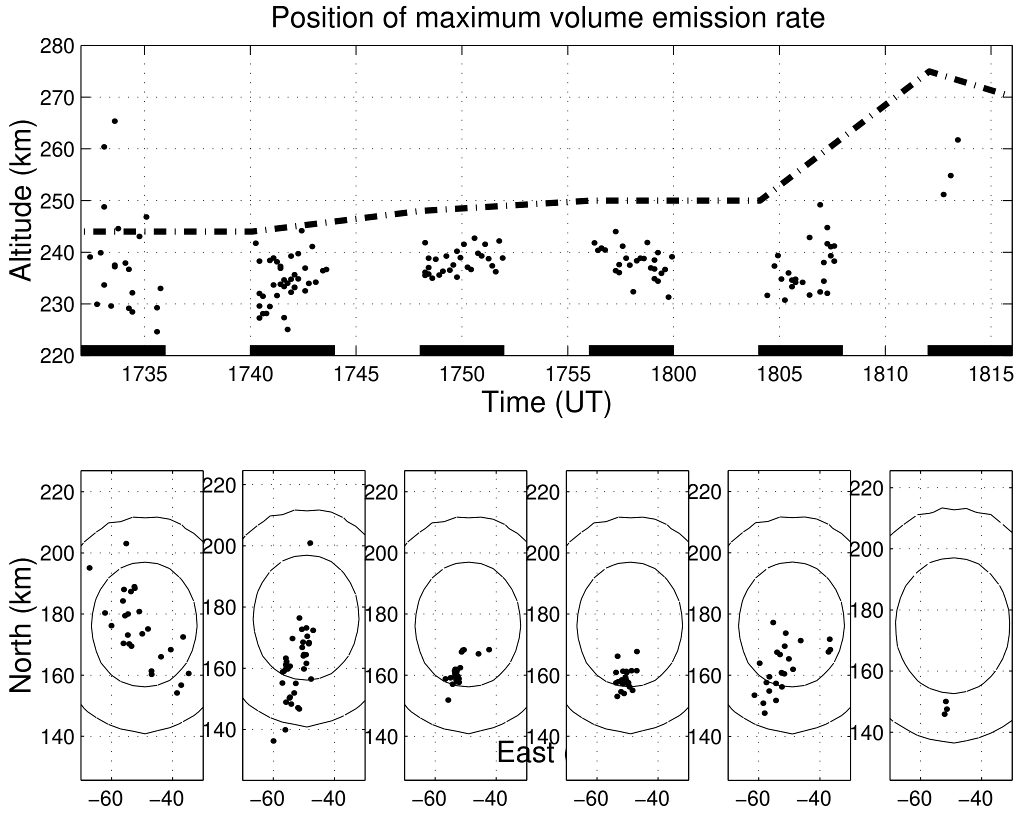

Figure 6.6: The upper panel shows the triangulated altitude of maximum enhanced airglow. The thick dashed line represents the altitude of the enhanced ion line as observed by EISCAT. The lower panels shows the horizontal location relative to Kiruna of the enhanced airglow region for the corresponding pulse. The dashed contours are the projections of the -1 and -3 dB free space antenna pattern projected to the reflection height. [After Figure 6 in *Gustavsson et al.*, 2001a]

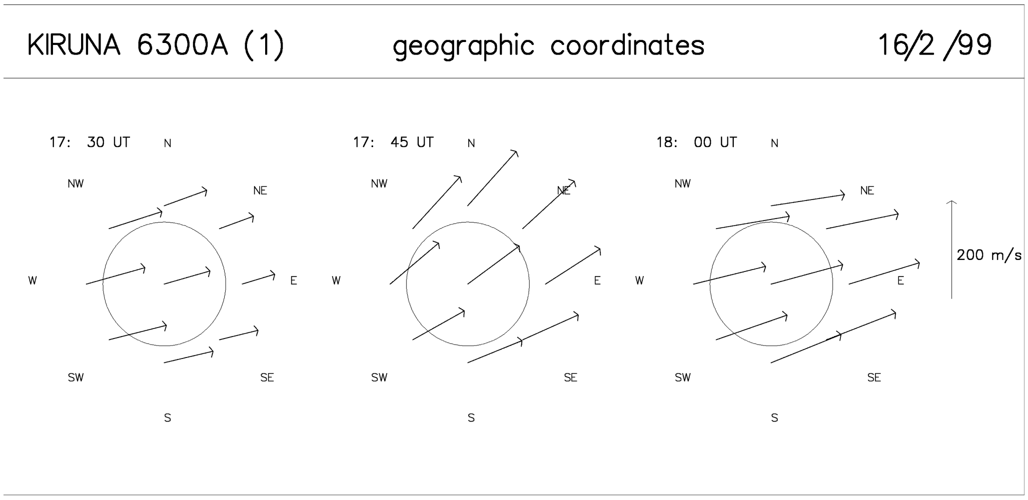

Figure 6.8: Fabry-Perot interferometer measurements of the neutral wind at 240 km altitude. The circle represents the field of view of the FPI looking at 45° elevation. This represents a circle above Kiruna with a radius of approximately 240 km. [After Figure 3 in *Gustavsson et al.*, 2001a]

displays winds varying between eastward and north-eastward, with velocities of 130-180 m/s. At 17:45 UTC the wind direction was $42° \pm 5°$ (north-eastward) with a velocity of 150 ± 5 m/s. Fabry-Perot neutral wind measurements (Figure 6.8) agree well with the north-eastward drift of the "centre of emission".

The EISCAT-UHF radar, operated at about 930 MHz, measured background plasma parameter values. The radar was operating in the common-program-1 mode with a GEN-type long pulse and alternating code [*Wannberg*, 1993], and was directed parallel to the geomagnetic field [see *Leyser et al.*, 2000, for additional information about the radar measurements].

Figure 6.9 displays these measurements of electron density, electron temperature and ion temperature versus time and altitude, with a range resolution of 22.5 km. Enhanced electron temperature is clearly seen for the transmitter cycle period of eight minutes (17:24–18:32 UTC). The electron temperature rises from an unperturbed background temperature of approximately 1000 K to about 3500 K, which corresponds to an increase of 250%. The exceptionally high temperature measurement at 18:20–18:24 UTC might be contaminated by pump-enhanced ion lines. The temperature enhancement extends several tens of km below the pump reflection height and several hundred kilometres above the reflection height [*Leyser et al.*, 2000]. A decay of the ionospheric electron density is seen in the top panel of Figure 6.9, as expected after sunset.

6.4.4 Discussion

The first report of HF pump-enhanced airglow at high latitudes was made by *Stubbe et al.* [1982] at the EISCAT Heating facility, Ramfjordmoen, Norway on October 5, 1981 at 17:40-18:20 UTC. In this experiment, photometers recorded a 50% increase (about 20 R) of the red-line (6300 Å) and a 15% decrease of the green line (5577 Å) during transmitter-on periods. The frequency was 5.423 MHz, and an O-mode beam with an ERP of 260 MW was switched 5 min on/5 min off. However, simultaneous observations made by *Henriksen et al.* [1984] did not find any evidence of pump enhanced airglow, which casted some doubts on the results by *Stubbe et al.* [1982]. In both of these observations, the optical instrumentation was scanning photometers with field-of-view of about 5°. This could have introduced aiming problems, causing the photometers to measure in the wrong region of the sky. On the other hand, it must be noted that Radio Frequency Interference (RFI) is more likely to produce false positive results from a photometer, as compared with an imager as a shift of bias of a single readout channel is more likely to be affected than all pixels in an image. These remarks illustrate why multi-station imaging measurements are superior to photometers given enough sensitivity. Such cameras were not available at the time of the experiments cited above.

The first clearly unambiguous observations of high-latitude HF pump-enhanced airglow were made on 16 February 1999, as described in the previous section. The positive result of this and subsequent observations might be attributed to some of the following reasons: improved optical instrumentation, more favourable ionospheric conditions, the approaching solar maximum. While the previous positive observation by *Stubbe et al.* [1982], relied on photometer measurements made from the same site as the EISCAT Heating facility, the results from 16 February 1999 were obtained by several stations located about 150–200 km away from the heating facility. Therefore, direct RFI from the transmitters can be clearly ruled out for these observations. The observations have also been confirmed by simultaneous measurements from an independent imager [*Kosch et al.*, 2000b,a, 2002b] on several occasions. It could therefore be stated that the validity of these observations are beyond all reasonable doubt. In addition, HF pump-enhanced airglow was observed at auroral latitudes at the High Frequency Active Auroral Research Program facility (HAARP) facility in Alaska [*Pedersen and Carlson*, 2001].

In *Brändström et al.* [1999] the observations of 16 February 1999 are found to be similar to the observations by *Bernhardt et al.* [1991] where an 165 MW, 5.828 MHz O-mode beam produced $\geq$ 200 R of airglow near zenith above the SURA-facility (latitude 56°N) in Russia.

The two intensity peaks in Figure 6.4, resemble seed irregularities as discussed by *Bernhardt et al.* [1991]. The drift-pattern of the two intensity peaks (Figure 6.7) is probably associated with electric fields and neutral-wind convection. During the next transmitter-on period 17:48–17:52 UTC, (Figure 6.5) a single patch of enhanced airglow appeared. *Leyser et al.* [2000] attributes this variability to possible large-scale plasma density irregularities in the pump-plasma interaction region.

The altitude of maximum volume emission is slightly lower than the pump reflection height of approximately 250 km as measured with the Dynasonde and EISCAT-UHF radar. These measurements are consistent with model calculations of the airglow emission altitude for different source altitudes of monoenergetic electrons [*Bernhardt et al.*, 1989].

The observed decay time of the airglow of approximately 30–35 s is signi-

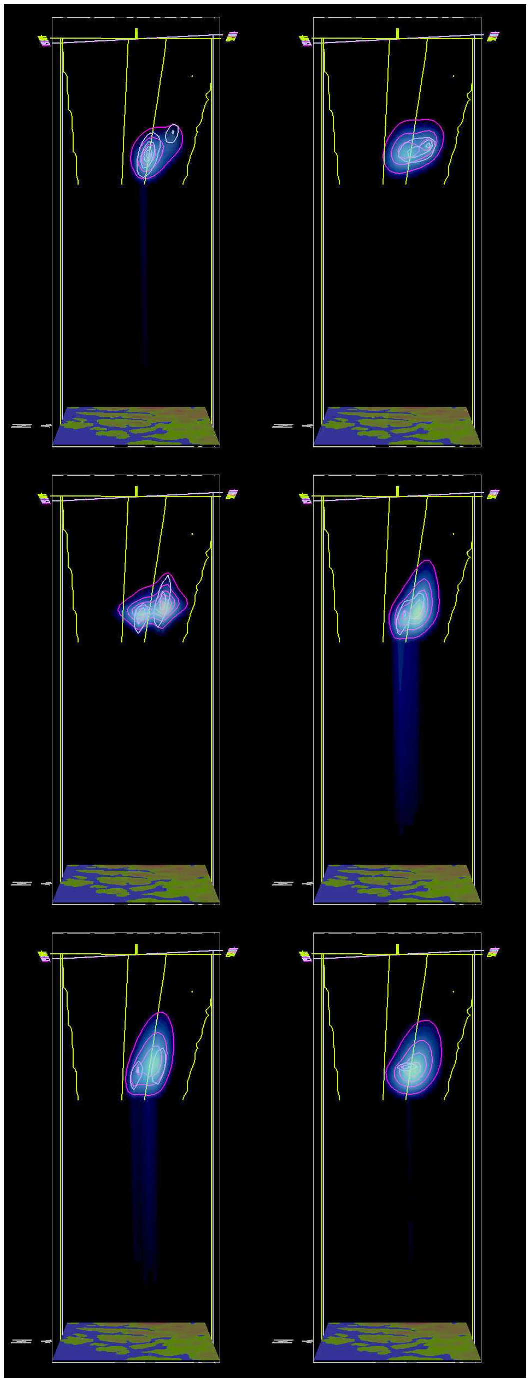

Figure 6.10: Volume rendering of the artificially enhanced airglow region above Tromsø, as seen from the west. The bottom plane shows the map of the Tromsø/Kiruna region. The yellow lines are the HF-pump 70% and 10% beam widths in the meriodonal plane, the purple and orange contours are the 6300 Å emission and the $O(^1D)$ excitation. UTC is (left→right top→ bottom) 17:32:50, 17:33:20, 17:33:50, 17:34:30, 17:34:50, 17:35:20. [After Plate 5 in *Gustavsson et al.*, 2001a]

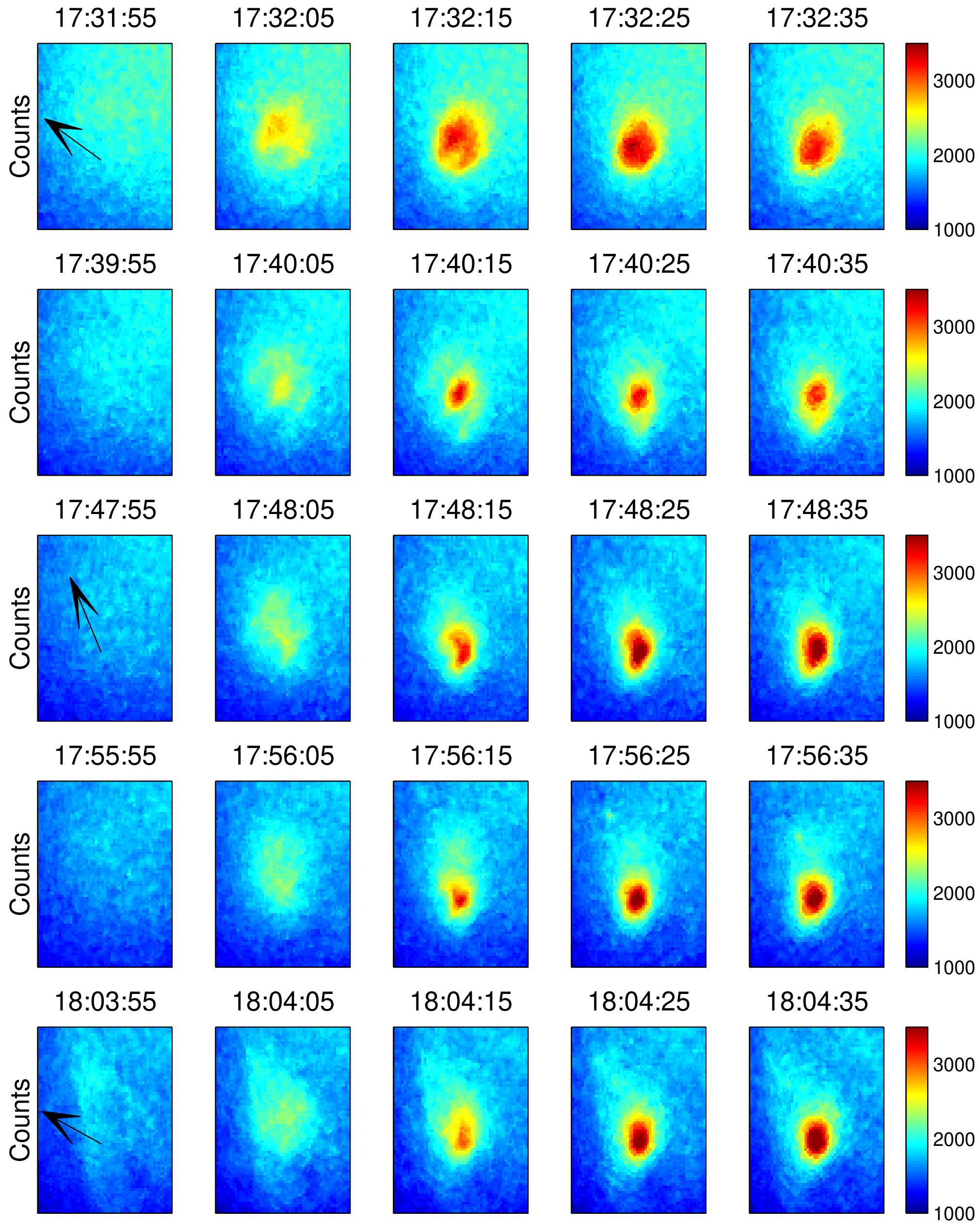

Figure 6.11: Estimates of the $O(^1D)$ excitation rates for the period just before transmitter-on and the four 10 s periods just after transmitter-on for five pulses. The arrows are the neutral wind direction projected to the images. All images are from the ALIS station in Silkkimuotka. [After Plate 7 in *Gustavsson et al.*, 2001a]

event cannot be made to occur at the desired time or place to fit a particular measurement. However, well-planned observations will increase the probability of making useful observations. In this section some of the results related to auroral studies are summarised.

6.5.1 An estimate of the auroral electron spectra

One of the traditional emission lines of choice for monochromatic auroral imaging is the $O(^1D)$ 6300 Å emission line [*Solomon et al.*, 1988; *Meier et al.*, 1989]. However, the excitation mechanism of that line is still under some debate [*Meier et al.*, 1989]. As the excited $O(^1D)$ state is quenched at lower altitudes, the ratios of the column emission rates for the $O(^1D)$ 6300 Å and N_2^+ 1Neg. 4278 Å emission-lines have been taken as an indicator of the characteristic energies of the precipitating electrons. The long radiative lifetime of the $O(^1D)$ 6300 Å emission line makes comparisons with the rapid N_2^+ 1Neg. 4278 Å and $O(^1S)$ 5577 Å emission-lines difficult, particularly for active auroral events.

In 1996 the first ALIS station was equipped with filters for the $O(3p^3P)$ 8446 Å emission line. Initial observations confirmed a sufficient signal strength for the ALIS-Imagers, and subsequently all stations were equipped with filters for this emission-line.

A preliminary study [*Steen et al.*, 1999a] presents data from 25 March 1998. Two ALIS stations (Kiruna and Merasjärvi) provided data from an auroral event occurring at the end of a geomagnetically disturbed period. An eastward travelling fold similar to that described by *Steen et al.* [1988] first appeared in the west and traversed the Kiruna zenith at about 1000 m/s as estimated from all-sky images. After that, the arc broke up and was replaced by a diffuse auroral band. The fold was observed in $O(^1D)$ 6300 Å, $O(^1S)$ 5577 Å, N_2^+ 1Neg. 4278 Å, and $O(3p^3P)$ 8446 Å. The observed fold appeared almost identical in all emission-lines, except, as expected in the slow $O(^1D)$ emission. This initial study concluded that the $O(3p^3P)$ 8446 Å auroral morphology appears similar to that of N_2^+ 1Neg. 4278 Å.

In a more extensive study [*Gustavsson et al.*, 2001b], two methods for estimating characteristics of primary electron spectra are compared and used to describe the auroral event of 25 March 1998. One method uses the spectral information in the images (Figure 6.12), while the other method is based on an inversion of the N_2^+ 1Neg. 4278 Å altitude distribution. Using the second method, ALIS can currently give estimates of the primary electron distribution with a time resolution of about 10 s (Figure 6.13). The paper concludes that only two dimensional measurements are able to follow the dynamics of this type of event, as single-point measurements cannot distinguish between temporal and spatial variations. Estimating the characteristic energy of precipitating electrons by combining measurements in 4278 Å, 6300 Å and 8446 Å provides useful results for temporal variations slower than 100 s. The primary electron spectra retrieved from the altitude distribution of the N_2^+ 1Neg. 4278 Å emission can give estimates of the electron characteristics with 10 s time resolution, but only for discrete auroral structures. To fully exploit the information obtainable from these kind of observations requires a combination of spectral and spatial analysis and to compare the results with two-dimensional electron transport and ionospheric models.

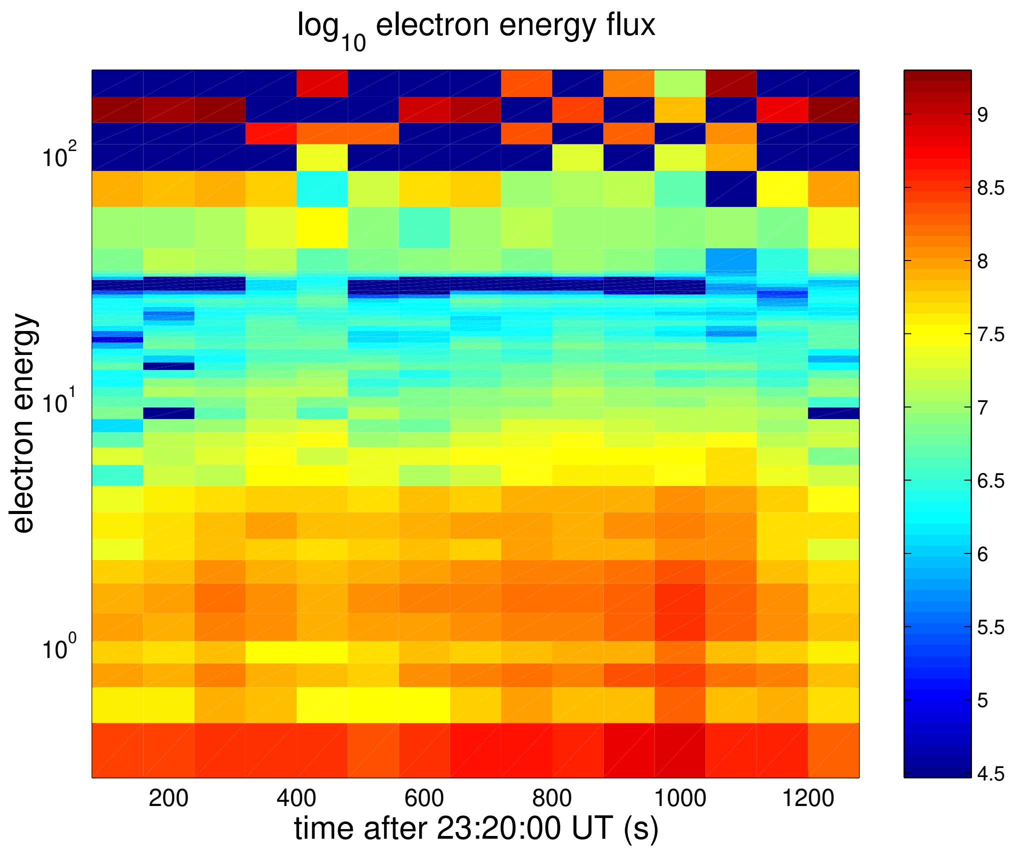

Figure 6.13: An estimation of the energy flux by inversion of N_2^+ 1Neg. 4278 Å altitude distribution. About 400 s after 23:20:00 UTC there appears to be a slight increase in both total flux and typical energy. [After Figure 6 in *Gustavsson et al.*, 2001b]

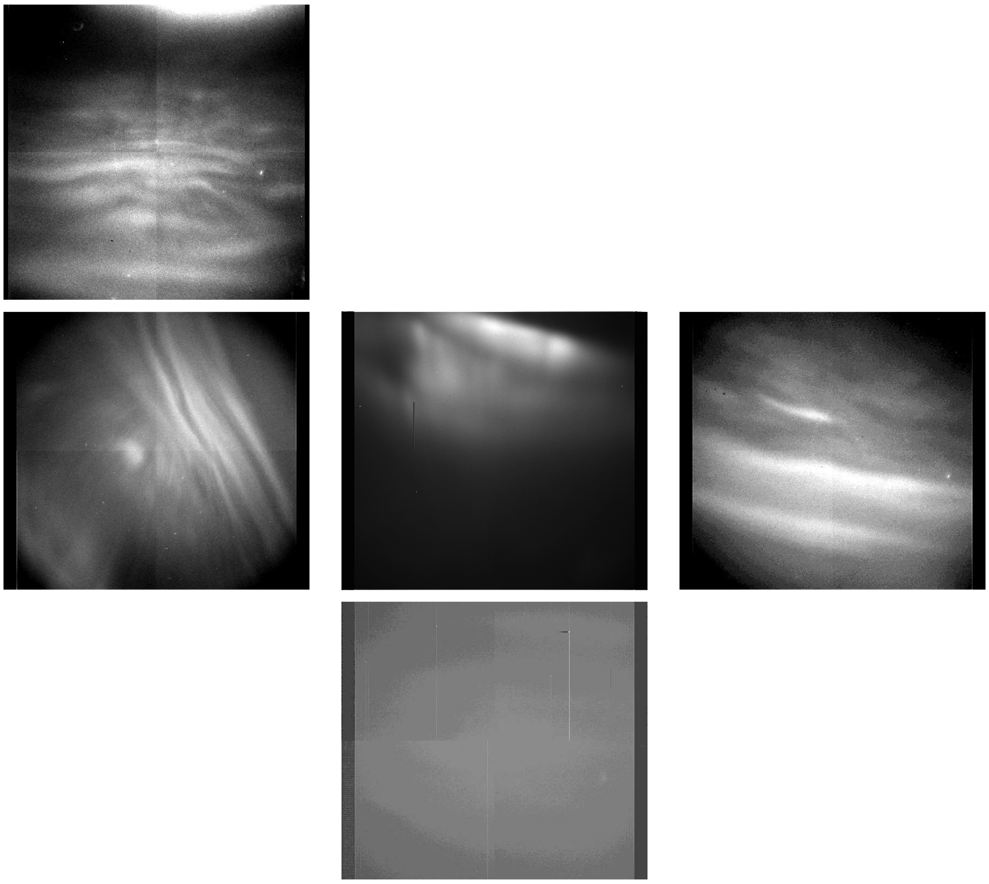

Figure 6.14: Example auroral images from 16 February 1997 during the FAST pass at 20:10:00 UTC; Abisko (top left), Nikkaluokta (middle-left), Kiruna (middle), Silkkimuotka (middle-right and Tjautjas (bottom). All images are in 5577 Å and with $t_{int} = 2$ s. The orientation of the Kiruna imager is $a_\phi = 0°$ and $z_\theta = 40°$. Nikkaluokta had no CPS at this time (hence the rotation) and was imaging zenith. The remaining stations are in the magnetic zenith position ($a_\phi = 180°$ $z_\theta = 12°$).

Normally measurements with ALIS stop for the season around 15 April, and operations resume in late August or early September. This is because the bright summer nights at arctic latitudes prevent ALIS from performing low-light measurements. However, some experiments have been made to try to image the aurora from ground even during this off-season. In this case the normal ALIS imagers (Chapter 3) are not usable, instead the camera head was dismantled and used together with a prototype imaging spectrometer for daylight auroral imaging. The main part of this new imaging instrument was an imaging optical spectrometer based on two 50 mm diameter capacitance-stabilised Fabry-Perot etalons [*Rees et al.*, 1981; *McWhirter*, 1993; *Rees et al.*, 1996, 1999] placed directly in series with each other and with a narrow-band (2 Å) interference filter. In front of this a wide-angle (35 mm) lens with telecentric optics was mounted. The output image consisting of interference fringes was imaged by a 300 mm lens onto a CCD camera-head from an ALIS-Imager (Chapter 3) operated with 2×2 on-chip binning. The spectrometer had a wavelength bandwidth of 3.7 pm [*Rees et al.*, 2000]. Since two capacitance-stabilised etalons were used, it was possible to tune the spectrometer by varying the optical path-differences of both etalons, placing the narrow annulus corresponding to 6300 Å emission line at any radius within the image. By scanning the position of the 6300 Å annulus and taking ten successive images at each scan position, it was possible to construct a two-dimensional sky-image at 6300 Å (Figure 6.15). This image was the main accomplishment over earlier studies. In this initial work a suitably-normalised previously published [*Delbouille et al.*, 1973] solar spectrum was subtracted since no suitable arrangement for measuring the solar spectrum across the entire image was present for the prototype instrument. Due to this, the intensities of the 6300 Å emission line were only roughly estimated, so neither useful Doppler-shifts (corresponding to wind) nor line-widths (corresponding to temperature) could be extracted.

With modest modifications, this instrument could be used to make optical auroral observations under all day-time solar illumination conditions, albeit with low temporal resolution.

6.5.6 The relation between the thermospheric neutral wind and auroral events

The thermosphere and ionosphere are coupled to the magnetosphere via electric fields and field-aligned currents [*Aruliah et al.*, 1996]. Intensification of the aurora is found to be related to rapid variations in the thermospheric neutral wind on a time scale that excludes contribution from the ion-drag force [*Steen and Collis*, 1988]. Instead the neutral wind variations must be understood in the context of large-scale coupling between the ionosphere and magnetosphere. ALIS can provide high resolution auroral images, that combined with neutral wind vector fields obtained by Fabry-Perot interferometer measurements can yield a better understanding of the relation between the thermospheric neutral-wind and the aurora.

Measurements of the F-region neutral wind using Fabry-Perot interferometers have been carried out in Kiruna since the early 1980's in collaboration with groups in the U.K. [*Aruliah et al.*, 1996]. In 1997, two scanning mirror Fabry-Perot interferometers were operated in collaboration with the Atmospheric Physics Laboratory at University College London [*McWhirter*, 1993; *Aruliah et al.*, 1996], as well as one Doppler Imaging System (DIS) [*Rees et al.*, 1997] in collaboration with Utah State University and Hovemere Ltd. In a preliminary study [*Brändström et al.*, 1997b] data from the latter instrument was compared to auroral images obtained from ALIS. The Doppler Imaging System (DIS) used in Kiruna consists of an all-sky lens, an interference filter for the 6300Å airglow/auroral emission and a Fabry-Perot etalon. The resulting interference fringes are imaged by an intensified Peltier-cooled CCD camera. In the subsequent analysis, each of the six interference fringes are divided into 24 sectors for which the Doppler shift of the input signal is calculated. Each sector thus corresponds to the Doppler-shift in a certain region of the sky, making it possible to 'image' the neutral wind velocity.

During the winter of 1996/1997 events with conjugate all-sky, ALIS and DIS observations were collected. Events when there was clear sky, auroral activity and preferably discrete auroral forms with a strong signal in the $O(^1D)$ 6300 Å emission line were selected. A collection of data from 10 January 1997 was described by *Brändström et al.* [1997b]. (Other promising events also exist for example 7–9 February 1997). When a stable arc was seen, the neutral wind was mainly northward. Preliminary analysis of the dataset suggests that the wind is directed perpendicular to the arc, with very low wind speeds parallel to the arc. This observation is supported by observations from 10 January. Another interesting feature in the data is the apparent westward drift of diffuse auroral structures at the same time as the wind turns eastward around 19:30 UTC. However these results are to be considered only as a demonstration of measurement possibilities. These studies have not been followed up so far.

6.6 Other studies

6.6.1 Polar stratospheric clouds

ALIS was optimised for studies of auroral phenomena at altitudes ranging from 90–300 km (Chapter 2). Despite this, it was realised early [*Steen*, 1989; *Steen et al.*, 1990] that ALIS might also be useful for the study of PSCs. Such clouds occur when regions of liquid or solid aerosols form in the altitude range of 15–30 km due to the low stratospheric temperatures that can be reached during the polar night in Arctic and Antarctic polar vortex combined with the additional rapid cooling caused by lee-waves [for example *Hesstvedt*, 1960; *Toon et al.*, 1986; *Crutzen and Arnold*, 1986; *Tolbert*, 1996, and references therein]. PSCs have been observed for more than a hundred years and *Mohn* [1893] attempted to make an altitude estimation by visual observations but arrived at uncertain results (23–100 km). One of the first accurate measurements of PSC altitude was performed by *Størmer* [1930], using photographic triangulation techniques. The presence of stratospheric clouds causes increased stratospheric ozone depletion [*Solomon et al.*, 1986] and because of this, the interest in PSC studies increased at the end of the last century.

ALIS is used to detect the appearance of PSCs and also to obtain temporal variation in the 3D distribution of the cloud surfaces. In 1997 ALIS made PSC observations, presenting a temporal development of the two-dimensional altitude

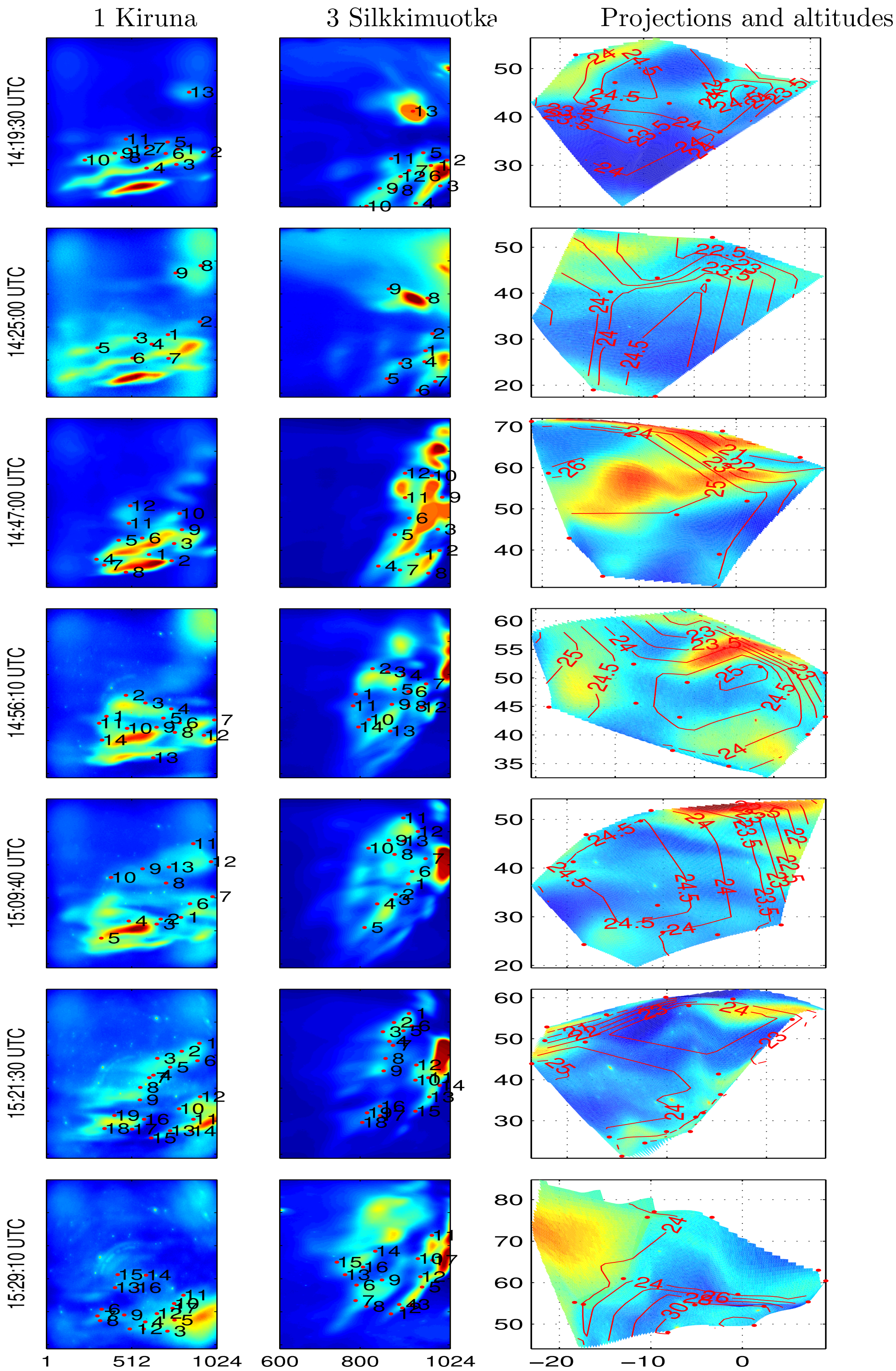

Figure 6.16: Columns 1 and 2: Time series of images (from Kiruna and Silkkimuotka, respectively) with identified PSC points (the colour-scales show the pixel values in 10^4 A/D counts after background subtraction). Rows 1-1024 and columns according to the abscissae are shown. Column 3: Contour surfaces of altitudes [km] spanned by these points, superimposed on projections of the images from station 1. The axes show W-E and N-S distances in kilometres from Kiruna. [After *Enell et al.*, 2003])

tions of this type. A meteor is most often seen during a short interval of just one second or less, and this must occur while the shutter is open. To maximise the possibility of acquiring an image of a meteor-trail, the stations should be operated with overlapping exposures, so that there are always at least two imagers with open shutters. In this way simultaneous imaging from up to six stations might occur, so that the altitude distribution of the meteor trails could be triangulated, while some stations simultaneously image the trails in the rather strong sodium (5893 Å) and calcium (4227 Å) emission lines [*Ceplecha and Rajchl*, 1963].

In a simulated study [*Brändström et al.*, 2001a] it was suggested that ALIS would operate with all six stations. The imagers would be oriented to observe a common volume, in order to enable triangulation of altitudes. The CCD-detectors are operated in maximum resolution mode (1024 × 1024 pixels) and with the longest possible integration times without saturating the CCD (on the order of several minutes). The dynamics is recorded by quickly opening and closing the shutter, with a period of 50 ms. (In principle this should be possible, but there are still some technical problems to be solved. Another option is to install a separate "meteor-shutter".) Performing the observations in this way increases the probability of observing a meteor and gives the possibility to study the velocities of a particular meteor at different altitudes.

In order to attempt experiments involving meteor observations, two filters with suitable passbands were procured (Table 6.5).

λ_{cw} [Å]	$\Delta\lambda$ [Å]	corr. passband [Å]	usage
4227	280	4087–4356	Covering Ca I and Fe I emission-lines [*Ceplecha and Rajchl*, 1963] as well as a water band around 4230 Å [*Dressler et al.*, 1992]
5893	200	5793–5978	Covering Na emission-lines at 5893 Å [*Ceplecha and Rajchl*, 1963]

Table 6.5: Filters for meteor studies. The table gives centre wavelengths, filter bandwidth, corrected passband and emission lines of interest.

Some preliminary studies were carried out during the Leonid showers of 1996 (without the meteor filters), 1999, 2000 and 2001. These observations yielded no usable results mainly due to bad weather conditions, although, important knowledge about how to perform an observation of this type was gained. The main objective with these experimental observations was to try to observe a predicted differential ablation process.

Successful observations of a meteor trail using two adjacent ALIS stations (Kiruna, and the mobile station) were obtained on 19 November 2002, at 03:48 UTC. The observed Leonid probably originated from the population ejected from the comet 55P/Tempel-Tuttle in 1767 according to the dust-trail simulations and observations by *McNaught and Asher* [1999]. Consequently this meteoroid was on its 7th period around the sun and still quite young in the sense that it had not lost much of its volatile constituents. Four images of this meteor trail appear

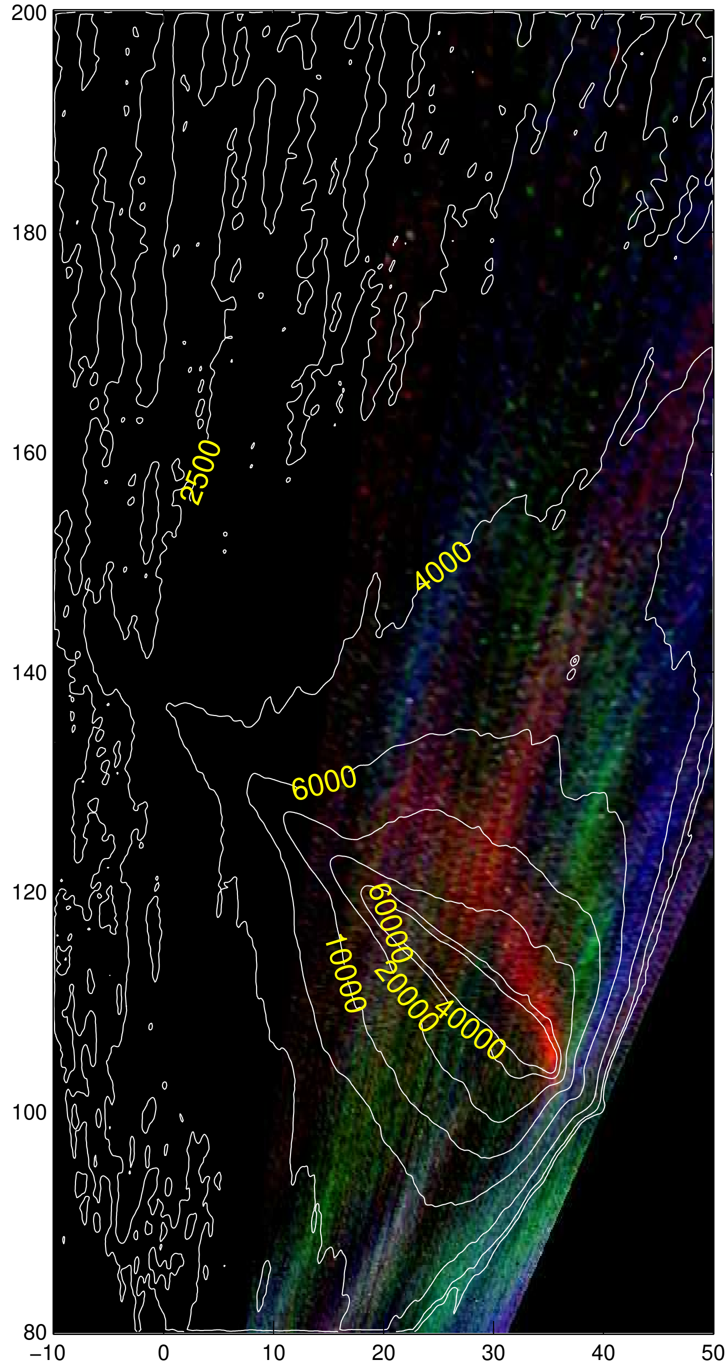

Figure 6.18: Projected altitude-profile of the raw-data in Figure 6.17. The iso-intensity lines corresponds to the 4227 Å image. The red, green and blue colours correspond to the three images in 5893 Å. It is possible to see how the Na emission in the meteor trail drifts with time from 03:48:00 UTC until 03:49:00 UTC.

A reader interested in further information related to three-dimensional imaging of the aurora and airglow, geometrical calibration, etc., is recommended to study *Gustavsson* [2000], as these topics were only briefly touched upon in the present work. Further reading related to the processing of multi-station auroral image data is found in the work by *Rydesäter* [2001].

Simultaneous auroral imaging from space-borne optical instruments would be an effective complement to the ground-based images. Ideally a sounding rocket launched through an auroral structure, resulting in simultaneous measurements from both ground and space, would certainly provide new insights into the auroral altitude distribution and the possibility to further validate and enhance the 3D-reconstruction techniques.

Observations of the rich and interesting night-sky phenomena related to auroral and ionospheric space plasma physics as well as the environmentally important atmospheric physics is a long-term commitment involving many disciplines as well as ground-based and space-borne instruments of various types. The diversity of the scientific results summarised in this chapter provides an example of what can be achieved on a moderate budget.

In this field of science, long-term stability, not only in terms of continuous observations, but also in terms of budget and staffing, combined with long-term plans for technical maintenance and development is important.

The GLIP was designed in such a way that it should be able to operate in the harsh climate of the Kiruna region without any manual attendance for a period of up to 8 months. It was a requirement to be able to monitor and control all necessary functions of the GLIP remotely, even if the normal means for controlling the station should fail. In the case of a total communication- and control failure, critical subsystems, such as heaters and sensitive detectors, should enter a safe survival mode. The station should furthermore be able to continue operation even if the control centre failed. Finally, the GLIP would be designed in a modular fashion, so that the various subsystems and instruments should be easy to replace for maintenance, etc. The major subsystems of the GLIP are described in the following sections; refer to the block diagram in Figure A.1.

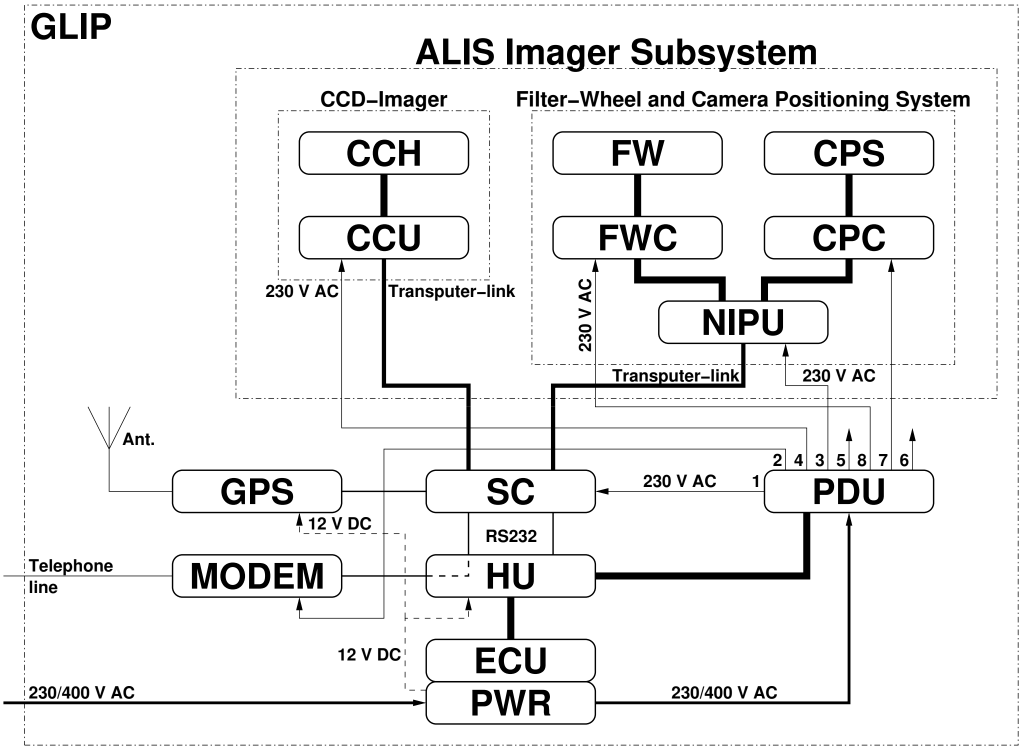

Figure A.1: Block diagram of the Ground-based Low-light Imaging Platform. The acronyms are explained in Table A.1

A.1 Station housing

The largest part of the GLIP consists of the station housing with the observing dome and instrument mount points. A Housing for ALIS (HALIS) must provide protection against the harsh climate: temperatures ranging from $-45°C$ to $+30°C$ (worst case), strong winds and intense solar radiation. The housing should also be easy to transport and assemble at distant locations. A special problem for an imaging station is the roof, where a large opening is required. On the prototype structure the roof was built in a traditional way, but the demand for

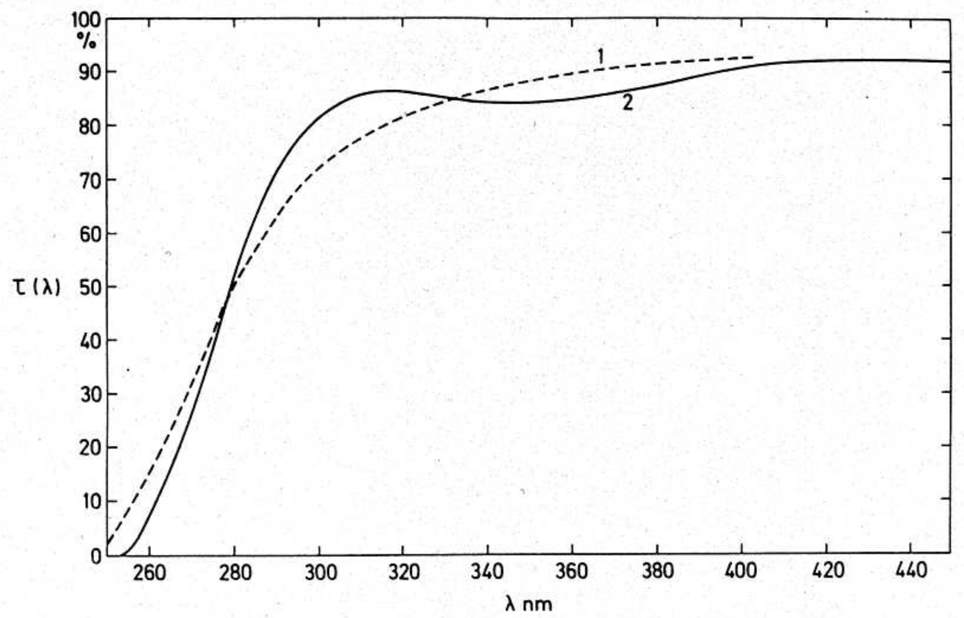

Figure A.2: Transmittance curves $T_{dome}(\lambda)$ for Plexi-glass Röhm GS2458 where λ is the wavelength in nm. Curve 1 corresponds to the transmission of a 3 mm thick Plexiglas sample obtained by Röhm, Darmstadt. Curve 2 has been measured by J. Stegman, MISU, Stockholm for a sample of 4 mm thickness. [After *Steen*, 1987]

insulation. The roof makes a smooth and water-proof transition from the square 2 m $\times$ 2 m cross-section of the structure to the circular 1 m diameter observing hole where the dome is mounted.

The semi-half-spherical observing dome is designed with a sleeve in such a way that the interface to the roof is water-tight (Figure A.4).

The HALIS can be transported and mounted at a distant location in less than one working day by 2–4 persons, using a simple trailer for road transportation, and assistance from a tractor or helicopter for the final move. The removable roof simplifies transportation and enables easy installation of large equipment modules into the station.

In total ten* HALIS of the design described above have been built for ALIS; eight are deployed on site and two of the structures are temporarily loaned out to ESRANGE. Some of the GLIPs have been on site for about ten years, without any major problems. A repainting of the plywood surfaces each decade seems appropriate to prolong the lifetime of the station.

Another experience gained from the early campaigns, (when two manned intensified CCD-cameras were operated at the Abisko and Nikkaluokta stations on a temporary basis), is that the GLIPs are not well-suited for manned operation. This is mainly due to condensation on the inner side of the dome, resulting from the humans in the station, and from frequent use of the door. After leaving the station, defrosting the dome might take up to 15 min depending on weather con-

*Two additional structures have been built for other users

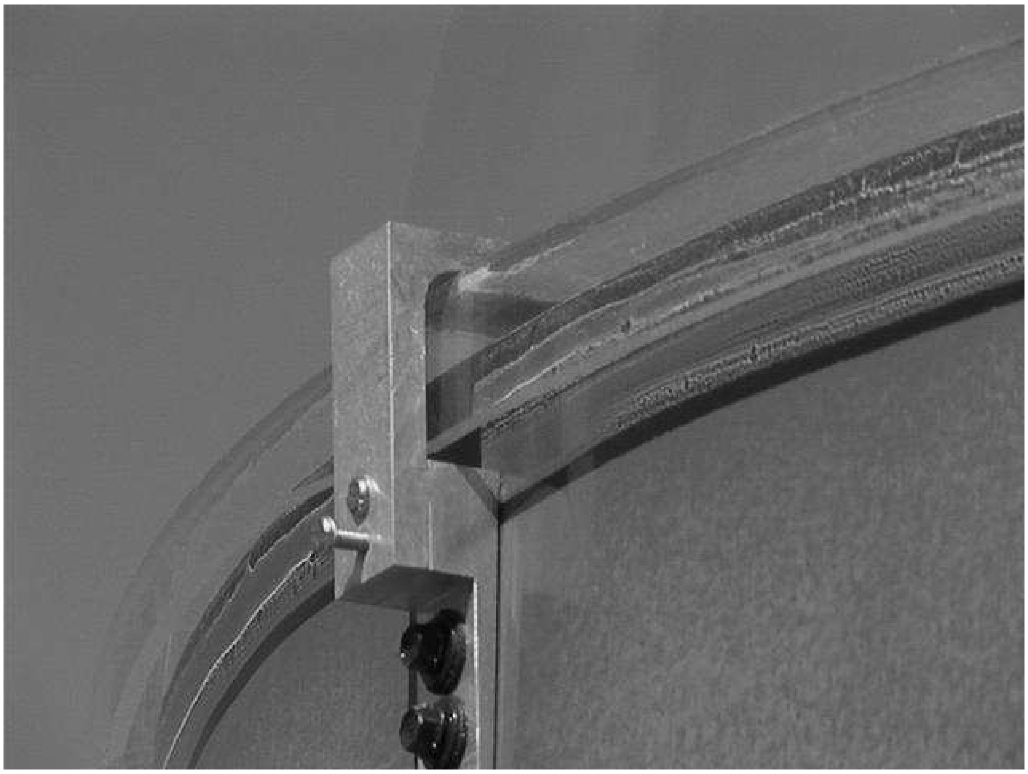

Figure A.4: Detail of the GLIP dome, showing the water-tight interface between the dome and the roof.

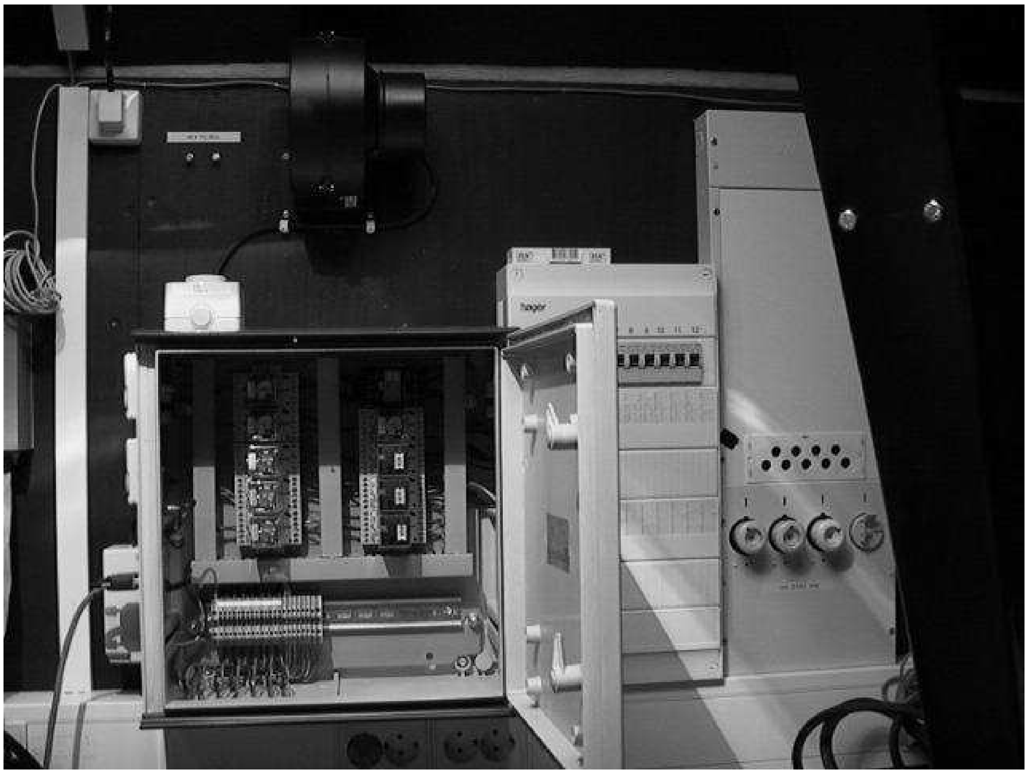

Figure A.5: The electrical installation of a GLIP. The cooling fan is seen in the upper-middle part of the image, below it is the environmental control unit (ECU) with thermostats and relays. To the right is the main fuse box and far right the main fuses and mains switch.

(230 V/10 A) with a power sensor and additional surge protection on each outlet as well as on the three incoming lines, thus enabling the housekeeping unit to monitor power failures on any of the incoming three phases as well as power distribution problems related to the PDU itself.

There is also a 12 V 75 Ah lead-acid battery with an automatic charger powering the housekeeping unit and other devices requiring an uninterrupted 12 V DC supply, such as the GPS receiver, etc.

A GLIP consumes up to 10000 kWh annually. Most of this energy is used by the heating and defrosting equipment. Some sites have had a rather large number of power failures, and it has been suggested that an Uninterrupted Power Supply (UPS) should be installed at each station to prevent the loss of measurements due to transients and short-term power outages.

If GLIPs are to be mounted in remote areas with no commercial power, they might have to generate their electrical power on site and therefore might require other solutions for heating and defrosting the dome.

A.4 Housekeeping Unit

The present Housekeeping Unit (HU) (Figure A.7) was designed in 1990, and is based on a similar, older system that proved reliable for many years. It is based on the 6502 microprocessor and the firmware is written in assembler and stored in EPROM. It also has non-volatile RAM with a real-time clock, a serial interface, A/D converter, a number of digital-I/O interfaces, various sensors and controls. The housekeeping unit is powered by uninterrupted 12 V DC (max 1 A) from the lead-acid battery.

Figure A.7: The ALIS Housekeeping Unit.

The housekeeping unit monitors battery and mains voltages, outdoor- dome- filter- and ambient temperatures, illumination level, fire- and trespass alarm sensors, precipitation (snow/rain) and the proper functioning of the station computer. It controls the power distribution unit, the environment control unit (Section A.2) and the access to the dial-up communication line.

If the station computer ceases to function properly, the housekeeping unit will take actions to bring the station into a safe state and alert the control centre of the situation. By sending commands directly to the housekeeping unit it is then possible to diagnose the situation and restart the station. Due to this solution, almost no trips to the stations have been required for system malfunctions.

The present housekeeping unit has been in use since 1991 and proven very reliable but must unfortunately soon be replaced as many of its components are obsolete. The next generation of housekeeping units will be based on a number

Figure A.9: Left: Exterior view of the mobile imaging platform. Right: Interior view of the mobile GLIP. The Imager assembly is mounted under the dome, on top of the rack. Below, a computer monitor, the FWC, keyboard, NIPU, computer and external disks can be seen.

A.6 Communication

Any communication equipment capable of connecting the station to a remote control centre or network can be used at the GLIP. Except for the Kiruna station, which has a Ethernet connection, all GLIPs have been using 28 kbits/s dial-up modem lines (Section 2.2.3). At the station a Local Area Network (LAN) interconnects all networked devices.

A.7 Station computer

The main computer controlling most of the GLIP is called the Station Computer (SC). The SC is typically a PC (i486 or newer) with the Debian GNU/Linux operating system (Section 2.2.1). In case of station computer malfunction, the housekeeping unit (Section A.4) will take over control, bring down all equipment in the GLIP to a safe state, and alert the control centre about the situation.

A.8 The mobile imaging platform

In order to improve the coverage close to the Tromsø magnetic field line, a van was equipped with a small dome as seen in Figure A.9.

The ALIS imager, camera-controller, filter-wheel controller, NIPU and station computer were installed inside the van (Figure A.9). In this case the imager was fixed in zenith so no camera positioning system was required. Since the van was

Parameter	Symbol	`ccdcam3`	Unit	Notes
Read noise	$\langle n_{e_r^-} \rangle$	7.62	e^-_{RMS}	a) b) $9@7\mu s/pixel$
Dark current	$\overline{n}_{e_d^-}$	17.75	$e^-_{RMS}\ s^{-1}$	at $-15°C$ b)5–6@ $-29°C$
Full well	$n_{e^-_{max}}$	313	ke^-	c)
Quantum efficiency	Q_E	83.0	%	4000 Å
Quantum efficiency	Q_E	99.3	%	5500 Å, at $-15°C$ d)
Quantum efficiency	Q_E	88.0	%	7000 Å
Quantum efficiency	Q_E	52.0	%	9000 Å

Table B.3: Some parameters for the CCD in ALIS-imager `ccdcam3` (Tk1024A, serial No. 1668BR08-02) as measured by the CCD-manufacturer. All values at $-45°C$ unless otherwise noted. Notes: a) quadrant with highest value. b) same parameter, as measured by camera manufacturer. c) quadrant A 3% linearity. d) questionable assuming a lower value (Figure 3.1) [author's note]

Parameter	Symbol	`ccdcam4`	Unit	Notes
Read noise	$\langle n_{e_r^-} \rangle$	7.24	e^-_{RMS}	a) b) $9@12.5\mu s/pixel$
Dark current	$\overline{n}_{e_d^-}$	8.43	$e^-_{RMS}\ s^{-1}$	at $-15°C$
Full well	$n_{e^-_{max}}$	269	ke^-	c) b) 240
Quantum efficiency	Q_E	69.5	%	4000 Å
Quantum efficiency	Q_E	83.4	%	5500 Å, at $-15°C$
Quantum efficiency	Q_E	88.1	%	7000 Å
Quantum efficiency	Q_E	53.1	%	9000 Å

Table B.4: Some parameters for the CCD in ALIS-imager `ccdcam4` (Tk1024AB, serial No. 4362BBR02-04) as measured by the CCD-manufacturer. All values at $-45°C$ unless otherwise noted. Notes: a) quadrant with highest value. b) same parameter, as measured by camera manufacturer. c) quadrant A 3% linearity.

Parameter	Symbol	`ccdcam5`	Unit	Notes
Read noise	$\langle n_{e_r^-} \rangle$	8.3	e^-_{RMS}	a) b)$7.5@10.5\mu s/pixel$
Dark current	$\overline{n}_{e_d^-}$	12.4	$e^-_{RMS}\ s^{-1}$	at $-15°C$.
Full well	$n_{e^-_{max}}$	316	ke^-	c)
Quantum efficiency	Q_E	89.8	%	4000 Å
Quantum efficiency	Q_E	98.9	%	5500 Å, at $-15°C$, d).
Quantum efficiency	Q_E	99.4	%	7000 Å, d).
Quantum efficiency	Q_E	55.3	%	9000 Å

Table B.5: Some parameters for the CCD in ALIS-imager `ccdcam5` (SI-003AB serial No. 6144GBR10-B2) as measured by the CCD-manufacturer. All values at $-45°C$ unless otherwise noted. Notes: a) quadrant with highest value. b) same parameter, as measured by camera manufacturer. c) quadrant A 3% linearity. d) questionable assuming a lower value (Figure 3.1) [author's note].

approach is investigated based on a commercial digital colour camera with replaceable standard optics. Such a camera can produce digital data of better, or at least similar quality, to the 16 mm colour films produced by the old camera. After testing a number of cameras, most were found to have too poor sensitivity or other problems. Eventually one camera with acceptable signal-levels for auroral imaging was found.

This camera (Fuji FinePix S1Pro, cost $\approx$ 30000 SEK) was equipped with a Nikon Nikkor 8 mm 1:2.8 objective-lens giving almost all-sky field-of-view (about $180^\circ \times 112^\circ$). Figure C.1 (Left) shows the prototype camera mounted in a dome of the optics lab in Kiruna. The final version will be mounted in an insulated

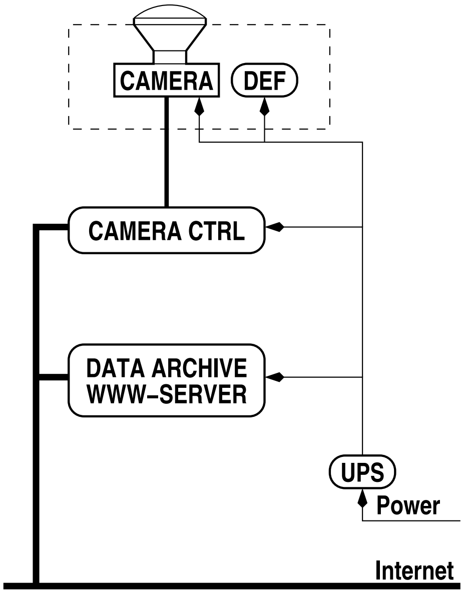

Figure C.1: Left: The prototype new digital all-sky camera (Fuji FinePix S1Pro) mounted on a tripod. The lens is a Nikon Nikkor 8 mm 1:2.8 giving almost all-sky field-of-view. Right: Block diagram of the new all-sky camera. The camera is controlled from a PC (CAMERA CTRL). The images (quick-looks and full-resolution images) are then downloaded to a data archive with a web-server. An UPS provides backup power. The camera is mounted in a heated insulated box with a defrosting device for the front-lens. Using two computers increases reliability and accessibility of the data-archive.

box together with all necessary equipment such as heaters, defrosters, etc.

The camera is controlled by a camera control computer (Figure C.1), and the image data is transferred to an archiving computer, where it is made available to the world-wide web. Monitoring and control of the camera can be done remotely using an ordinary web browser. A data storage medium suitable for long-term storage will be selected later, for example writable CDs or DVDs, etc. A sample images appears on the in Figure C.2. The large auroral image on the cover is also from this camera. This prototype camera eventually developed severe reliability problems related to its internal firmware, the USB interface (used for communication with the PC) and possibly also the shutter. Therefore the manufacturer and black aurora with an acceptable signal-to-noise ratio. These cameras could therefore be a good tool for studies of auroral morphology and dynamics, as well as for providing supporting images for other instruments (ALIS, EISCAT, etc.). Another interesting future possibility is to use this type of camera together with methods for automated image analysis as described by [for example *Rydesäter*, 2001; *Syrjäsuo*, 2001] for automated control over spectroscopic imaging systems like ALIS. The following table summarises some of the features of the camcorder tested:

- 3 CCD $\approx$ 450 kpixels.
- Optics: $f = 6 - 72$ mm 1:1.6-2.4
- 12$\times$ optical zoom, 48$\times$ digital zoom.
- miniDV tapes (memorystick for still-images)
- IEEE-1394 "Firewire" capture directly to a computer.
- Colour auroral imaging possible from about 3 images per second up to video rate, depending on auroral intensity. Good sensitivity for Red and Green auroras, acceptable for blue.

A sample frame of an auroral scene with a meteor trail is displayed in Figure C.3. Video footage can be made available by the author on request.

2001a,b]. Based on this information, an estimate of the efforts required to restart ALIS will be presented. It is important to note that in order to make a final plan, a thorough technical examination of vital systems is required. Such an investigation is estimated to take about two man-months (preferably two people for one month). However despite this, it should be possible to start immediate measurements with two imagers in parallel as the rest of ALIS is evaluated, the only constraint being staff availability.

The following list summarises anticipated status of the main technical systems (see also Figure A.1 in Appendix A).

The ALIS stations: In order to save money all stations have been left with electrical power switched off. To avoid equipment damage, heating should be turned on at least two weeks before attempting to turn on any equipment. The GLIPs (Appendix A) are expected to be found in good condition. However the domes will require cleaning, and some stations might require repainting.

Computers: With few exceptions, all computers should be usable. However, all computers are old, and failures cannot be excluded. As each station computer needs at least two ISA-slots for interface boards (NIPU, CCU), it is important to keep the old computers usable as long as possible as new computers with ISA slots are becoming rare. Although the NIPU must be replaced soon, it is not feasible to replace the CCU within a couple of years at the present funding level. Computer replacements must likely be scheduled within 1–2 years.

The NIPU: All NIPUs (Section 2.2.2) were working in 2001, and are expected to be used at least initially. It must be stressed, however, that the NIPUs are totally obsolete, they cannot be repaired, nor can any changes to the CPS and FPS be accommodated (for example replacements of angular encoders). As the NIPUs are essential for filter changes, it is important to replace these units as soon as possible. They can be replaced by micro-controllers at a reasonable cost.

Communication systems: All dial-up telephone lines must be checked. Some modems might require replacement. It should furthermore be investigated if station 5 in Abisko can be connected to Internet via the LAN at the Abisko Research Station. Continued efforts should be made to find cheaper and faster communication to the stations. (see also Section 2.2.3)

Station data storage: Most external disks used for local data storage (Section 2.2.4) at the stations are well past their safe technical lifetime, due to many hours of operation. They are also small by present standards. As disk-crashes at the stations may lead to large data losses, all disks should be replaced. The cost for procuring 10–12 external disks is relatively low.

Data archiving: Documentation and backup copying at alternate sites of the ALIS data-base is underway as this is written. It is recommended that the archive media be transferred from CD-R (Recordable CD-ROMs) to

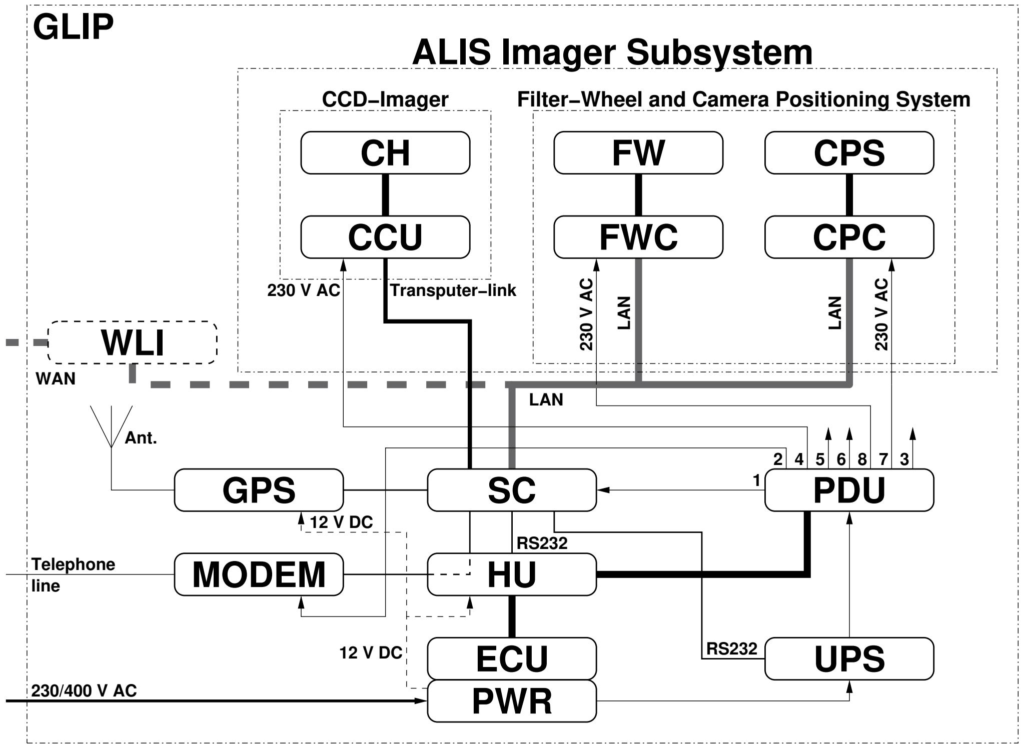

Figure D.1: In the first stage of the upgrade, the NIPU would be replaced by micro-controllers in the FWC and CPC. Also an UPS and possibly a faster network connection would be added at the stations. The acronyms are explained in Table A.1 and D.1

Acronym	Explanation
ICC	Imager Control Computer
LAN	Local Area Network
UPS	Uninterruptable Power Supply
WAN	Wide Area Network (connected to the Internet)
WLI	WAN/LAN Interface consisting of the WAN-Interface, a router, a switch and possibly also a firewall

Table D.1: Explanation of acronyms in Figures D.1–D.2 (See also Figure A.1 and Tables A.1 in Appendix A) as well as for performing the necessary upgrades and maintenance, it might be an option to increase the student involvement in the observations, as well as in some software development and data-analysis.

The fate (i.e. funding) of ALIS in a longer perspective is directly dependent on what actions are taken in the upcoming 1–3 years. A stable core-group with thorough scientific and technical experience from ALIS operations is without doubt the most critical component.

D.2.1 A longer perspective

Given a sustained and increased funding in the future, upgrading (or replacing) the imagers is required in a longer perspective. Also all obsolete systems at the stations need to be replaced. The next step would probably be to expand ALIS towards Tromsø with station (9) Frihetsli (Figure 2.4 and Table 2.3) and possibly near the EISCAT site at Ramfjordmoen, as well as equipping the existing stations (7) Kilvo and (8) Nytorp with instruments. For such new stations a tentative block-diagram appears in Figure D.2. It must also not be forgotten

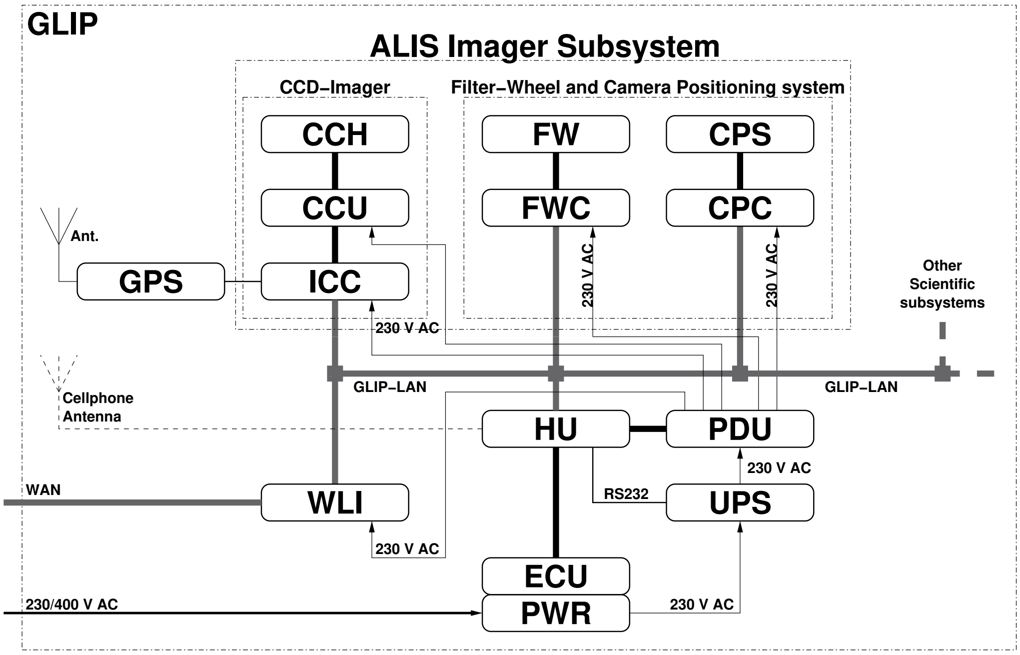

Figure D.2: For future new stations, the SC is replaced by an new HU, which might have a cell-phone interface for emergency operation. The imager is controlled by a dedicated computer, and the dial-up line is replaced by a high-speed Internet connection.

that the GLIPs are capable of housing several other instruments of various types (Section 2.1). Such instruments could include imaging spectrometers, dedicated cloud cameras, colour imagers for auroral imaging (Appendix C), magnetometers, riometers, ionosondes, etc.

Another issue is that as the stations become networked over permanent Internet connections, there will be no need for a dedicated control centre as illustrated in Figure D.3. Given an internationally-standardised set of interfaces, any collec-

Aso, T., M. Ejiri, H. Miyaoka, T. Ono, T. Hashimoto, T. Yabu, and M. Abe, Aurora stereo observations in Iceland, in *Proc. NIPR Symposium on Upper Atmos. Phys.*, vol. 6, pp. 1–14, National Institute of Polar Research, 1993.

Aso, T., M. Ejiri, H. Miyaoka, T. Ono, Y. Tetsuro, K. Muguruma, T. Hashimoto, and M. Abe, Aurora stereo observation in Iceland and its tomography analysis, *Trans. Inst. Electronics Communication Engineers*, *J77-DII*, 69–78, 1994, (in Japanese).

Aso, T., M. Ejiri, A. Urashima, H. Miayoka, Å. Steen, U. Brändström, and B. Gustavsson, First results from auroral tomography from ALIS-Japan multi-station observations in March 1995, *Earth Planets Space*, *50*, 81–86, 1998a.

Aso, T., M. Ejiri, A. Urashima, H. Miyaoka, Å. Steen, U. Brändström, and B. Gustavsson, Auroral tomography analysis of a folded arc observed at the ALIS-JAPAN multi-station campaign on March 26, 1995, in *Proceedings of the NIPR Symposium on upper atmosphere Physics*, vol. 11, pp. 1–10, National Institute of Polar Research, Tokyo, 1998b.

Aso, T., Å. Steen, U. Brändström, B. Gustavsson, A. Urashima, and M. Ejiri, ALIS — a state of the art optical observation network for the exploration of polar atmospheric processes, *Adv. Space Res.*, *26*, 917–924, 2000.

AstroCam Ltd., *4400 Programmer's reference manual*, AstroCam Ltd., 1995.

AstroMed Ltd., *4400 Programmer's reference manual*, AstroMed Ltd., 1993.

Backlund, V., Über die Technik der simultanen Telefilmsplanigraphie, *Acta Radiol. Suppl.*, *137*, 1956, (PhD Thesis).

Baker, D. J., and G. J. Romick, The Rayleigh interpretation of the unit in terms of column emission rate or apparent radiance expressed in SI units, *Applied Optics*, *15*, 1966–1968, 1976.

Barmore, F. E., High resolution observations of the 6300 Å oxygen line in the day airglow, *Planet Space Sci.*, *25*, 185–191, 1977.

Baschin, O., Die ersten Nordlichtphotographien etc., *Met. Z.*, *17*, 1900.

Bens, A. R., L. L. Cogger, and G. G. Shepherd, Upper atmospheric temperatures from Doppler line-widths — Observation of the OI dayglow emission at 6300 Å, *Planet Space Sci.*, *13*, 551–563, 1965.

Bernhardt, P. A., C. A. Tepley, and L. M. Duncan, Airglow enhancements associated with plasma cavities formed during ionospheric heating experiments, *J. Geophys. Res.*, *94*, 9071–9092, 1989.

Bernhardt, P. A., W. A. Scales, S. M. Grach, A. N. Keroshtin, D. S. Kotik, and S. V. Polyakov, Excitation of artificial airglow by high power radio waves from the SURA ionospheric heating facility, *Geophys. Res. Lett.*, *18*, 1477–1480, 1991.

M. L. P. Thomas Lindbladh and J. Kinser, vol. 3728, pp. 108–114, Royal Institute of Technology, Stockholm, Sweden, The International Society for Optical Engineering, 1998, ISBN 0-8194-3202-4.

Brändström, U., B. Gustavsson, Å. Steen, and A. Pellinen-Wannberg, ALIS (Auroral Large Imaging System) used for optical observations of the meteor impact process, in *Proceedings of the Meteoroids 2001 Conference*, edited by B. Warmbein, vol. SP-495, pp. 331–336, European Space Agency, 2001a, ISBN 92-9092-805-0.

Brändström, U., T. Lövgren, A. Moström, C.-F. Enell, B. Gustavsson, T. Aso, M. Ejiri, Å. Steen, and P. Rydesäter, Brief report on ALIS (Auroral Large Imaging System), a new all-sky camera in Kiruna and auroral imaging using a mini-DV camcorder, in *Proc. of 28th Annual European Meeting on Atmospheric Studies by Optical Methods*, Sodankylä Geophysical Observatory, 2001b, (in press).

Carlson, C. W., The Fast Auroral SnapshoT explorer, *EOS, Transactions, American Geophysical Union*, *73*, 1992.

Carlsson, H. C., V. B. Wickwar, and G. P. Mantas, Observations of suprathermal electrons accelerated by HF-excited instabilities, *J. Atmos. Terr. Phys.*, *44*, 1089–1100, 1982.

Celsius, A., *Observationes de lumine boreali*, Norimbergae, 1733.

Ceplecha, Z., and J. Rajchl, The meteor spectrum with dispersion from 11 to 38 Å/mm, *Publishing House of the Czechoslovak Academy of Sciences*, *14*, 29–47, 1963, (Available from the NASA Astrophysics Data System).

Chamberlain, J. W., *Physics of the aurora and airglow*, Classics in geophysics, AGU (American Geophysical Union), 1995, (A reprint of the original work from 1961).

Cocks, T. D., D. F. Creighton, and F. Jacka, Application of a dual Fabry-Perot spectrometer for daytime airglow studies, *J. Atmos. Terr. Phys.*, *42*, 499–511, 1980.

Conde, M., and F. Jacka, Analysis of day-time observations of the 630 nm thermospheric emission over Mawson, Antarctica, *ANARE Res. notes*, *69*, 125–138, 1989.

Conde, M. P., P. Greet, and F. Jacka, The Ring effect in the sodium D2 Fraunhofer line of day skylight over Mawson, Antarctica, *J. Geophys. Res.*, *97*, 11,561–11,565, 1992.

Cormac, A. M., Representation of a function by its line integrals, with some radiological applications, I, *J. Appl. Phys.*, *34*, 2722–2727, 1963a.

Cormac, A. M., Representation of a function by its line integrals, with some radiological applications, II, *J. Appl. Phys.*, *35*, 2908–2913, 1963b.

Enell, C.-F., Optical studies of polar stratospheric clouds and related phenomena, Ph.D. thesis, Swedish Institute of Space Physics, Kiruna, Sweden, 2002, (IRF Scientific Report 278), ISBN: 91-7305-307-4.

Enell, C.-F., B. Gustavsson, Å. Steen, U. Brändström, P. Rydesäter, P. Johansson, T. Wagner, U. Friess, K. Pfeilsticker, and U. Platt, Optical studies of polar stratospheric clouds, in *Proceedings of SPIE, Satellite remote sensing of clouds and the atmosphere IV*, edited by J. E. Russell, vol. 3867, pp. 290–297, The International Society for Optical Engineering, 1999a.

Enell, C.-F., Å. Steen, B. Gustavsson, U. Brändström, P. Johansson, T. Wagner, U. Frieß, K. Pfeilsticker, and U. Platt, Studies of polar stratospheric clouds occurence at Kiruna, in *XXV annual European Meeting on Atmospheric Studies by Optical Methods*, pp. 122–126, Instituto de Astrofísica de Andalucia, Granada, Spain, 1999b.

Enell, C.-F., Å. Steen, B. Gustavsson, U. Brändström, P. Johansson, T. Wagner, U. Frieß, K. Pfeilsticker, U. Platt, and K.-H. Fricke, Detection of polar stratospheric clouds at Kiruna, in *Air pollution report 69, Mesoscale processes in the stratosphere*, edited by K. S. Carslaw and G. T. Amanatidis, vol. 18912, pp. 65–68, Office for Official Publications of the European Communities, European Commission, Luxembourg, 1999c, ISBN 92-828-4629-6.

Enell, C.-F., B. Gustavsson, Å. Steen, U. Brändström, and P. Rydesäter, Multistatic imaging and optical modelling of nacreous clouds, *Phys. Chem. Earth*, *25*, 451–457, 2000.

Enell, C.-F., U. Brändström, B. Gustavsson, S. Kirkwood, K. Stebel, and Å. Steen, Case studies of the development of polar stratospheric clouds using bistatic imaging, *Ann. Geophys.*, 2003, (in press).

Frey, S., H. U. Frey, D. J. Carr, O. H. Bauer, and G. Haerendel, Auroral emission profiles extracted from three-dimensionally reconstructed arcs., *J. Geophys. Res.*, *101*, 21,731–21,741, 1996.

Galand, M., Special section: Proton precipitation into the atmosphere, *J. Geophys. Res.*, *106*, 1–178, 2001.

Galperin, Y. I., Multiple scales in auroral plasmas, *J. Atmos. Solar and Terr. Phys.*, *64*, 211–229, 2001.

Gardner, J. A., A. L. Broadfoot, W. J. McNeil, S. T. Lai, and E. Murad, Analysis of the GLO-1 observations of meteoric metals in the thermosphere, *J. Atmos. Terr. Phys.*, *61*, 545–562, 1999.

Gartlein, C. W., Unlocking secrets of the northern lights, *Nat. Geograph. Mag.*, p. 673, 1947.

Gassendi, P., *De vita Pereskii, Anno 1621*, Edit. Hag. Com., 1651.

Gilbert, P., Iterative methods for the three-dimensional reconstruction of an object from projections, *J. Theor. Boil.*, *36*, 105–117, 1972.

Hedin, M., I. Häggström, A. Pellinen-Wannberg, I. Häggström, L. Andersson, U. Brändström, B. Gustavsson, Å. Steen, A. Westman, G. Wannberg, T. van Eyken, T. Aso, C. Cattell, C. W. Carlson, and D. Klumpar, Trough observations with the EISCAT radars, ALIS auroral imaging system and FAST satellite, in *Proceedings of RadioVetenskap och Kommunikation 99*, edited by J.-O. Gustavsson, vol. 1, pp. 113–117, Högskolan i Karlskrona/Ronneby, Karlskrona, Sweden, 1999, ISBN 91-630-8156-3.

Hedin, M., I. Häggström, A. Pellinen-Wannberg, I. Häggström, L. Andersson, U. Brändström, B. Gustavsson, Å. Steen, A. Westman, G. Wannberg, T. van Eyken, T. Aso, C. Cattell, C. W. Carlson, and D. Klumpar, 3-D extent of the main ionospheric trough —a case study, *Adv. Polar Upper Atmos. Res.*, *14*, 157–162, 2000.

Henriksen, K., W. Stoffregen, B. Lybekk, and Å. Steen, Photometer and spectrometer search of the oxygen green and red lines during artificial ionospheric heating in the auroral zones, *Ann. Geophys.*, *2*, 73–76, 1984.

Hernandez, G., *Fabry-Perot Interferometers*, Cambridge University Press, 1986, ISBN: 0-521-32238-3.

Hertel, R. J., Signal and noise properties of proximity focused image tubes, in *Ultrahigh Speed and High Speed Photography, Photonics and Videography*, edited by G. L. Stradling, vol. 1155, pp. 332–343, The International Society for Optical Engineering, 1989.

Hesstvedt, E., On the physics of mother of pearl clouds, *Geofysiske Publikasjoner*, *XXI*, 1–32, 1960.

Holst, G. C., *CCD arrays, cameras and displays*, 2nd ed., The International Society for Optical Engineering, 1998, ISBN: 0-8194-2853-1.

Høymork, S. H., ed., *Sensors and Instruments for Space Exploration*, chap. 6. Measurements by optical methods, pp. 71–119, 2nd ed., Swedish Institute of Space Physics, Kiruna, 2000.

Hunten, D. M., F. E. Roach, and J. W. Chamberlain, A photometric unit for the aurora and airglow, *J. Atmos. Terr. Phys.*, *8*, 345–346, 1956.

Hyppönen, M., R. Pellinen, C. Sucksdorff, and R. Torniainen, Digital all-sky camera, *Tech. Rep. 9*, Finnish Meteorological Institute, Helsinki, 1974.

Höffner, J., and U. von Zahn, The 1996 Leonid shower as studied with a potassium lidar: Observations and inferred meteoroid sizes, *J. Geophys. Res.*, *104*, 2633–2643, 1999.

Ivanov, V. E., and T. I. Sergienko, Interaction of the auroral electrons with the atmospheric gases. (the Monte-Carlo modelling), 1992, Nakua, St. Petersburg, 1992.

Janesick, J. R., T. Elliott, S. Collins, M. M. Blouke, and J. Freeman, Scientific charge-coupled devices, *Optical Engineering*, *26*, 692–714, 1987.

Labsphere, *A guide to integrating sphere theory and applications*, Labsphere, 1997.

Lance, C., and R. H. Eather, High frequency active auroral research program (HAARP) imager, *Tech. rep.*, Air Force Geophysics laboratory, USAF, Hanscom AFB, Massachusetts USA, 1993, PL-TR-93-2219.

Lauche, H., and O. Widell, Intercalibration of low light level sources, letter from Hans Lauche, 2000a.

Lauche, H., and O. Widell, Intercalibration of low light level sources, in *Proc. of 27th Annual European Meeting on Atmospheric Studies by Optical Methods, Stockholm, Sweden*, Meteorological institution, Stockholm university, Sweden, 2000b.

Leyser, T. B., Parametric interactions between upper hybrid and lower hybrid waves in heating experiments, *Geophys. Res. Lett.*, *18*, 408–411, 1991.

Leyser, T. B., and B. Gustavsson, Private communication, 2003.

Leyser, T. B., B. Gustavsson, B. U. E. Brändström, F. H. Å. Steen, T. A. M. T. Rietveld, and M. Ejiri, Simultaneous measurements of high-frequency pump-enhanced airglow and ionospheric temperatures at auroral latitudes, *Adv. Polar Upper Atmos. Res.*, *14*, 1–11, 2000.

Leyser, T. B., B. U. E. Brändström, B. Gustavsson, T. Sergienko, and M. T. Rietveld, Enhanced airglow by high frequency electromagnetic pumping with the EISCAT heating facility and observed by the multi-station auroral large imaging system ALIS, in *URSI*, URSI, 2002, paper 815, 2002.

Lodin, H., The value of tomography in examination of the intrapulmonary bronchi, *Acta Radiol. Suppl.*, *101*, 1935.

Love, S. G., and D. E. Brownlee, A direct measurement of the terrestial mass accretion rate of cosmic dust, *Science*, *262*, 550–553, 1993.

Macleod, H. A., *Thin-film optical filters*, Macmillan, New York, 1986, ISBN: 0-02-948110-4.

Mantas, G. P., Large 6300 Å airglow intensity enhancements observed in ionosphere heating experiments are excited by thermal electrons, *J. Geophys. Res.*, *99*, 8993, 1994.

Mantas, G. P., and H. C. Carlson, Reinterpretation of the 6300 Å airglow enhancements observed in the ionosphere heating experiments based on analysis of Platteville Colorado, *J. Geophys. Res.*, *101*, 195–209, 1996.

Massey, P., *A User's guide to CCD Reductions with IRAF*, National Optical Astronomy Observatory, 1992, `http://iraf.noao.edu/docs`.

McDade, I. C., and E. J. Llewellyn, Satellite airglow limb tomography: Methods for recovering structured emission rates in the mesospheric airglow layer, *Canad. J. Phys.*, *71*, 552–563, 1994.

Pedersen, and Carlson, First observations of HF heater-produced airglow at the High Frequency Active Auroral Research Program facility: Thermal excitation and spatial structuring, *Radio Sci.*, *36*, 1013–1026, 2001.

Pellinen, R., and K. Kaila, Optical groundbased network, in *Proc. of the Cluster workshop, Svalbard, Norway 16–19 Sept.*, pp. 147–158, European Space Agency Publications Division, 1991, (ESA SP-330).

Pellinen-Wannberg, A., E. Murad, B. Gustavsson, U. Brändström, C.-F. Enell, C. Roth, I. P. Williams, and Å. Steen, Water in Leonid meteor trails, *(in preparation)*, 2003.

Perkins, F. W., and P. K. Kaw, On the role of plasma instabilities in ionospheric heating by radio waves, *J. Geophys. Res.*, *76*, 282–284, 1971.

Pliny, *Historiae Naturalis*, vol. II, chap. 27,33, (ancient text), ca. 77.

Pountain, D., The transputer strikes back, *Byte*, pp. 265–275, 1991.

Preston, T. J., *4400 Quad CCD Camera controller user guide. System description and operations manual*, AstroMed Ltd., Cambridge, 1993.

Preston, T. J., *4400 Quad CCD Camera controller user guide for motherboard issue B. System description and operations manual*, AstroCam Ltd., Cambridge, 1995.

Puccio, W., Private communication, 2002.

Pudovkin, M. I., Å. Steen, and U. Brändström, Vorticity in the magnetospheric plasma and its signature in the aurora dynamics., *Space Science Rev.*, *80*, 411–444, 1997.

Pudovkin, M. I., Å. Steen, N. V. Nikolaev, O. I. Kornilov, U. Brändström, B. Gustavsson, and P. Rydesäter, Automatic recognition of auroral forms, in *Ninth workshop on Virtual Intelligence / Dynamic neural networks*, edited by M. L. P. Thomas Lindbladh and J. Kinser, vol. 3728, pp. 121–127, Royal Institute of Technology, Stockholm, Sweden, The International Society for Optical Engineering, 1998, ISBN 0-8194-3202-4.

Raspopov, O. M., V. A. Dergachev, and E. G. Goos'kova, Ezekiel's vision: visual evidence of Sterno-Etrussia geomagnetic excursion?, *EOS, Transactions, American Geophysical Union*, *84*, 77, 2003.

Rayleigh, L., Absolute intensity of the aurora line in the night sky, and the number of atomic transitions required to maintain it, *Proc. Roy. Soc. London*, *A129*, 458, 1930.

Rees, D., I. McWhirter, P. B. Hays, and T. Dines, A stable rugged, capacitance-stabilised piezoelectric scanned Fabry-perot etalon, *J. Phys. E: Sci. Instrum.*, *14*, 1320–1325, 1981.

Sergienko, T., Private communication, 2003.

Sergienko, T., B. Gustavsson, Å. Steen, U. Brändström, M. Rietveld, T. Leyser, and F. Honary, Analysis of excitation of the 630.0 nm airglow during heating experiment in Tromsø on February 16, 1999, *Phys. Chem. Earth*, *25*, 531–535, 2000.

Simpson, W., The point-to-point protocol (ppp), *Request For Comments: 1661*, 1994, ftp://ftp.rfc-editor.org/in-notes/rfc1661.txt.

Sipler, D. P., and M. A. Biondi, Measurements of $O(^1D)$ quenching rates in the F region, *J. Geophys. Res.*, *77*, 6202–6212, 1972.

Siscoe, G. L., A historical footnote on the origin of aurora borealis, *EOS, Transactions, American Geophysical Union*, *59*, 994, 1978.

Siscoe, G. L., S. M. Silverman, and K. D. Siebert, Ezekiel and the Northern lights: Biblical aurora seems plausible, *EOS, Transactions, American Geophysical Union*, *83*, 173, 2002.

Solomon, S., R. R. Garcia, F. S. Rowland, and D. J. Wuebbles, On the depletion of Antarctic ozone, *Nature*, *321*, 755–758, 1986.

Solomon, S. C., P. B. Hays, and V. J. Abreu, Tomographic inversion of satellite photometry, *Applied Optics*, *23*, 3409–3414, 1984.

Solomon, S. C., P. B. Hays, and V. J. Abreu, The auroral 6300 Å emisson: Observation and modelling, *J. Geophys. Res.*, *93*, 9867–9882, 1988.

Spurny, P., H. Betlem, K. Jobse, P. Koten, and J. van't Leven, New type of bright Leonid meteors above 130 km, *Meteorit. Planet. Sci.*, *35*, 1109–1115, 2000.

Steen, Å., The optical laboratory in Kiruna: A new research facility in the auroral zone, *KGI Tech. Report 033*, Kiruna Geophysical Institute, Kiruna, Sweden, Kiruna, Sweden, 1987, ISSN 0349-2672.

Steen, Å., Investigations of auroral dynamics, techniques and results, Ph.D. thesis, Swedish Institute of Space Physics, Kiruna, Sweden, 1988a, (KGI Scientific Report 1994), ISSN 0984-1703.

Steen, Å., An auroral height measuring system designed for real time operation, *Rev. Sci. Instrum.*, 1988b.

Steen, Å., An Auroral Large Imaging System in Northern Scandinavia, in *Proc. 9th Symposium on European rocket and ballon programmes and related research, Lahnstein, FRG*, pp. 299–303, European Space Agency, 1989, ESA SP-291.

Steen, Å., ed., *Auroral Tomography workshop proceedings*, IRF Scientific Report 213, Swedish Institute of Space Physics, 1993, ISSN 0284-1703.

Steen, Å., Application for equipment to an optical calibration facility in kiruna, Funding application to Forskningsrådsnämnden (FRN), 1998, (partly in Swedish, IRF Dnr 238-150/98).

Strickland, D. J., R. R. Meier, J. H. Hecht, and A. B. Christensen, Deducing composition and incident electron spectra from ground-based auroral optical measurements: theory and results, *J. Geophys. Res.*, *94*, 13,527–13,539, 1994.

Stubbe, P., H. Kopka, H. Lauche, M. T. Rietveld, A. Brekke, O. Holt, T. B. Jones, T. Robinson, A. Hedberg, B. Thidé, B. Crochet, and H. J. Lotz, Ionospheric modification experiments in northern Scandinavia, *J. Atmos. Terr. Phys.*, *44*, 1025–1041, 1982.

Syrjäsuo, M., New Finnish all-sky cameras, in *Proceedings of the 24th annual European meeting on atmospheric studies by optical methods*, pp. 247–251, Sentraltrykkeriet A/S Bodø, 1997, ISBN: 82-994583-0-7.

Syrjäsuo, M. T., All-sky camera, (master's-thesis), Helsinki Univ. of Technology, 1996.

Syrjäsuo, M. T., Auroral monitoring network: From all-sky camera system to automated image analysis, (D.Sc.(Tech.)-thesis), Finnish Meteorological Institute, Helsinki, Finland, 2001, Contribution series 32, ISBN: 951-697-551-8.

Theuwissen, A. J. P., *Solid-state imaging with charge-coupled devices*, vol. 1 of *Solid-state scenece and technology library*, Kluwer, 1995.

Tolbert, M. A., Polar clouds and sulfate aerosols, *Science*, *272*, 1597, 1996.

Toon, O. B., P. Hamill, R. P. Turco, and J. Pinto, Condensation of HNO_3 and HCl in the winter polar stratospheres, *Geophys. Res. Lett.*, *13*, 1284–1287, 1986.

Tornéus, A., GOSSIP a general information panel for ALIS, *IRF Tech. Rep. 040*, Swedish Institute of Space Physics, Kiruna, Sweden, 1992, ISSN 0284-1738.

Torr, M. R., and P. Espy, Intercalibration of instrumentation used in the observation of atmospheric emissions: Second progress report, *Tech. Rep. 101*, Utah State University, Center for atmospheric and space sciences, Logan Utah, 1981.

Trondsen, T. S., High spatial and temporal resolution auroral imaging, Ph.D. thesis, University of Tromsø, 1998.

Urashima, A., T. Aso, M. Ejiri, Å. Steen, U. Brändström, and B. Gustavsson, Camera calibration by integrating sphere for the auroral tomography observation, *Adv. Polar Upper Atmos. Res.*, *13*, 79–88, 1999.

Vaattovaara, M., and J. Enback, Development of a calibration system using a monochromator and an APD, *Internal Note 023*, Swedish Institute of Space Physics, 1993.

Vegard, L., Photographische Aufnahmen des Nordlichtspektrums mit einem Spectrographen von grosser Dispersion, *Phys. Zhur.*, *14*, 677–681, 1913.

Vegard, L., and O. Krogness, The position in space of the aurora polaris, in *Geofysiske Publikasjoner*, vol. 1 of *Geofysiske Publikasjoner*, pp. 1–170, A. W. Brøggers bogtryckeri, Christiania (Oslo), Norway, 1920.